Carbon Nanotube

Based Nanofluidic Devices

by

Pei Pang

A Dissertation Presented in Partial Fulfillment
of the Requirements for the Degree
Doctor of Philosophy

Approved November 2011 by the
Graduate Supervisory Committee:

Stuart Lindsay, Chair
Robert Ros
John Shumway
Nongjian Tao
José Menéndez

ARIZONA STATE UNIVERSITY

December 2011

ABSTRACT

Nanofluidic devices in which one single-walled carbon nanotube (SWCNT) spans a barrier between two fluid reservoirs were constructed, enabling direct electrical measurement of the transport of ions and molecules. Ion current through these devices is about 2 orders of magnitude larger than that predicted from the bulk resistivity of the electrolyte. Electroosmosis drives excess current, carried by cations, and is found to be the origin of giant ionic current through SWCNT as shown by building an ionic field-effect transistor with a gate electrode embedded in the fluid barrier. Wetting of inside of the semi-conducting SWCNT by water showed the change of its electronic property, turning the electronic SWCNT field–effect transistor to “on” state. These findings provide a new method to investigate and control the ion and molecule behavior at nanoscale.

DEDICATION

For my beloved parents:

Yong Pang and Manling Yang

ACKNOWLEDGMENTS

It is such a pleasure to take this moment to sincerely thank my advisor, Professor Stuart Lindsay, for his support and guidance. What he brought to me is how to perform work better, greatly benefiting my career path in the future. I owe my deepest gratitude to Dr. Jin He. His valuable advice and constant patience for my research lets me get through all the way.

I would like to thank theorist Professor Predrag S. Krstić and his group members in Oak Ridge National Laboratory for their theoretical analysis and simulation work. I would like to thank Dr. Brett Gyarfas for the help in programming and learning of TEM. I would also like to thank my committee members, Professor Robert Ros, John Shumway, Nongjian Tao and José Menéndez for their help.

I have to thank my CNT colleagues in our group. Di Cao and Tao Luo helped me in fabrication work in lab and cleanroom. Hao Liu taught me the chemical and biological knowledge and brightened me up when I was down. Weisi Song, a pretty good partner on optical instruments, struggled with me in experiement and bore my complaint in hard time. Padmini Krishnakumar shared her thoughts and comments on my work.

My gratitude is also to the other past and current members in our group. I learned AFM from Dr. Qiang Fu and STM from Dr. Lisha Lin. The discussion with Dr. Shuo Huang and Shuai Chang always benefits me. I also got much insight in chemistry from Dr. Peiming Zhang, Dr. Feng Liang, Shuhui Wan and Sen Peng. Yanan Zhao shared his knowledge in programming with me.

I am grateful to Maggie Black, Michael Dodson and Steve Woodward for their technical assistance in lab. I want to thank all my friends who have given me so much help during these years.

I would also like to thank the staffs of CSSER (center for solid state electronics research) in ASU for their cleanroom training and technical problem solving.

Finally, I was financially supported by the National Human Genome Research Institute.

TABLE OF CONTENTS

Page

CHAPTER Page

CHAPTER Page

LIST OF TABLES

LIST OF FIGURES

Figure Page

Figure Page

Parts of this dissertation include collaborative published work, in which I am as the first, the second listed co-author or later.

Chapter 4 is adapted with permission from Haitao Liu, Jin He, Jinyao Tang, Hao Liu, Pei Pang, Di Cao, Predrag Krstić, Sony Joseph, Stuart Lindsay and Colin Nuckolls. The reported experiments were performed by Haitao Liu, Jin He, Jinyao Tang, Hao Liu, Pei Pang and Di Cao under the guidance of Stuart Lindsay and Colin Nuckolls. Haitao Liu and Jin He performed the measurement and data collection. Hao Liu ran the quantitative polymerase chain reaction (QPCR). Both Pei Pang and Di Cao did device fabrication work and parts of the measurement. Predrag Krstić and Sony Joseph performed theoretical simulations. Stuart Lindsay and Colin Nuckolls wrote the manuscript. The results were separately published in two journals: *Science* (DNA translocation) and *Journal of Physics: Condensed Matter* (nucleotide translocation as a review report).

Chapter 5 is adapted with permission from Pei Pang, Jin He, Jae Hyun Park, Predrag Krstić and Stuart Lindsay. The reported experiments were performed by Pei Pang under the guidance of Stuart Lindsay and Jin He. Pei Pang did device fabrication work and performed the measurement,

data collection and part of data analysis. Jin He did the major data analysis. Predrag Krstić and Jae Hyun Park performed theoretical simulations. Stuart Lindsay and Jin He wrote the manuscript. The results from this work were published in *ACS Nano*.

Chapter 6 is adapted with permission from Di Cao, Pei Pang, Jin He, Tao Luo, Jae Hyun Park, Predrag Krstić, Colin Nuckolls, Jinyao Tang and Stuart Lindsay. The reported experiments were performed by Di Cao and Pei Pang under the guidance of Stuart Lindsay and Jin He. Both Di Cao and Pei Pang did device fabrication work and performed the measurement and data collection. Tao Luo grew carbon nanotubes. Jin He did the data analysis. Predrag Krstić and Jae Hyun Park performed theoretical simulations. Colin Nuckolls and Jinyao Tang carried out primary measurement work and shared helpful discussion. Stuart Lindsay and Jin He wrote the manuscript. The results from this work were published in *ACS Nano*.

1. INTRODUCTION: PROPERTIES OF CARBON NANOTUBES

1.1 Physical Structure of Carbon Nanotubes

Carbon nanotubes (CNTs), like hollow straws, are of various lengths but just nanometers in diameter. They have been of great interest from fundamental point of view to devices development, since their discovery in 1991 by Iijima.[1] Based on the number of graphene layers, CNTs are categorized as single-walled carbon nanotubes (SWCNTs) and multi-walled carbon nanotubes (MWCNTs). An ideal CNT can be considered as a hexagonal network of carbon atoms, or graphene sheet, which is rolled up to form a seamless hollow cylinder. SWCNT, having a cylindrical shell with only one atom in thickness (~1.4 Å), is considered as the fundamental structural unit. The diameter and helicity of any SWCNT can be characterized by the chiral vector $\vec{C}_h = n\vec{a}_1 + m\vec{a}_2$ which connects two crystallographically equivalent sites on a 2D graphene sheet (see **Figure 1.1**). The integers *n* and *m* denote the number of unit vectors ($\vec{a}_1$ and $\vec{a}_2$, respectively) along two directions in the honeycomb crystal lattice of graphene. The SWCNT is “armchair" nanotube when n=m；if m=0，it is called "zigzag". Otherwise, the others are called "chiral". Meanwhile, the absolute value of chiral vector $|\vec{C}_h|$ is the circumference of SWCNT and so the diameter d_t of the nanotube can be given by the geometric calculation as below:

$$d_t = \left|\vec{C}_h\right| / \pi = \frac{\sqrt{3}a_{c-c}}{\pi}\sqrt{n^2 + m^2 + nm}, \tag{1.1}$$

where a_{c-c} is the C-C bond length (~1.42 Å).

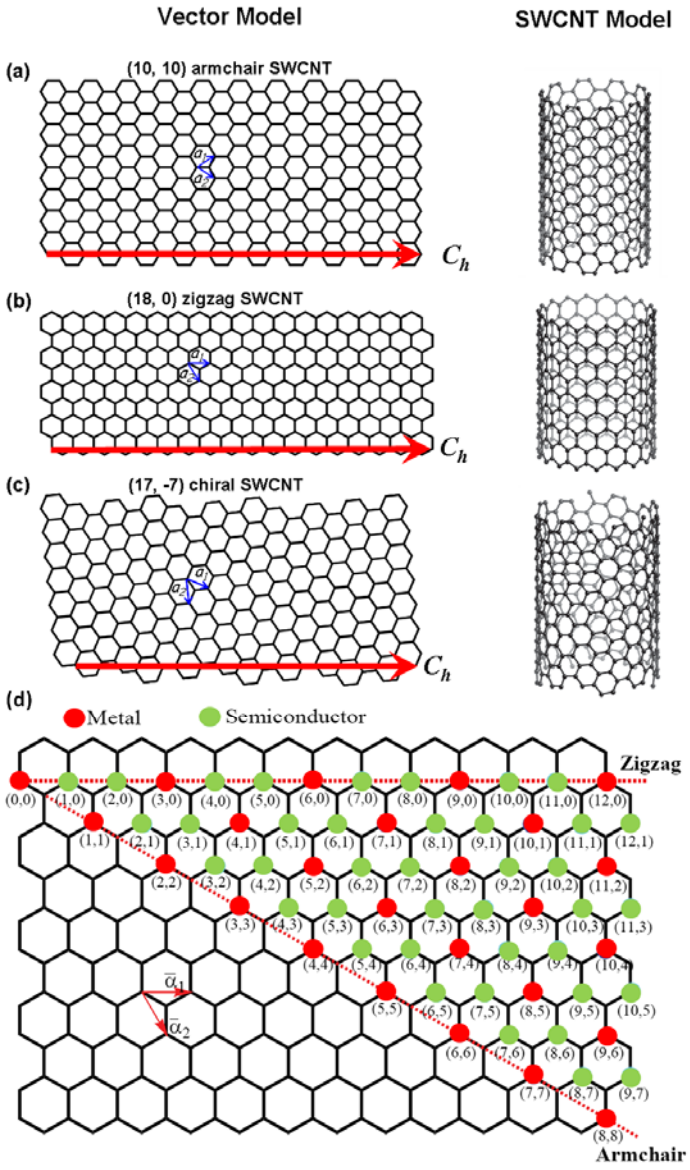

Figure 1.1 (a)–(c) Schematic illustration of the SWCNT chirality: armchair (10,10), zigzag (18,0) and chiral (17,-7). The left column shows the rolling of graphene sheets to a carbon nanotube, illustrating the chiral vector $\vec{C}_h$ with respect to the unit vectors $\vec{a}_1$ and $\vec{a}_2$ in the honeycomb crystal lattice of the graphene. The right column displays the corresponding SWCNT models. (d) Chiral structures for possible SWCNT structures.[2]

1.2 Electronic Structure of Carbon Nanotubes

The electronic properties of SWCNT are highly sensitive to their structural parameters: if n − m is a multiple of 3, then the nanotube is metallic; otherwise the nanotube is a semiconductor. Actually, such properties can be explained by a sketch of the band structure of rolled-up graphene modified by the reduced dimensionality.

1.2.1 Electronic band structure of graphene

The early studies of graphene utilized the tight binding method to obtain its energy dispersion relations.[3] First of all, **Figure 1.2** shows the unit cell indicated by the dash line part. $\vec{a}_1$ and $\vec{a}_2$ are unit vectors in real space, as discussed in Section 1.1. In order to find out the electronic band structure, we need to find out the information about the momentum state, $\vec{k}$, in the reciprocal lattice of graphene. The first Brillouin zone, as the unit cell of the reciprocal lattice, is shaded in **Figure 1.2b**. The reciprocal lattice vectors are given by:

$$\vec{b}_1 = \frac{2\pi}{\sqrt{3}a}\hat{k}_x + \frac{2\pi}{a}\hat{k}_y, \tag{1.2}$$

$$\vec{b}_2 = \frac{2\pi}{\sqrt{3}a}\hat{k}_x - \frac{2\pi}{a}\hat{k}_y, \tag{1.3}$$

corresponding to a reciprocal lattice constant of $\frac{4\pi}{\sqrt{3}a}$ where $a = |\vec{a}_1| = |\vec{a}_2| = \sqrt{3}a_{c-c}$. Here Γ, K and M as three high symmetry points (the

center, the corner, and the center of the edge, respectively) are defined and labeled as well.

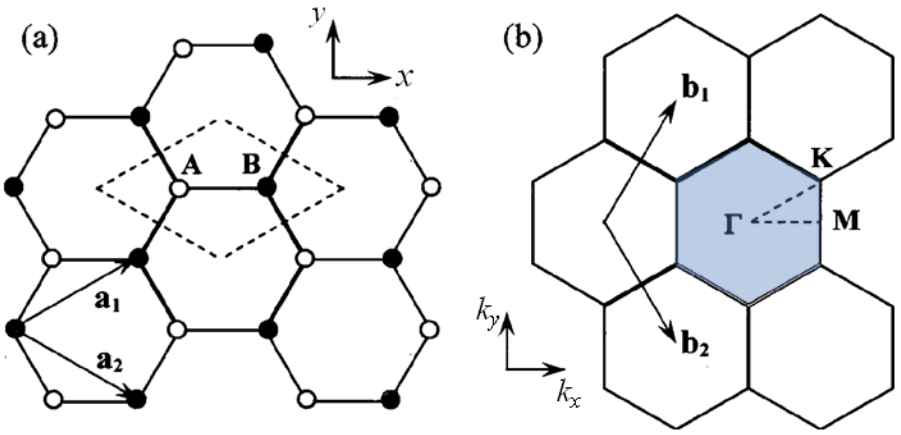

Figure 1.2 (a) The unit cell indicated by the dash rhombus, in which A and B are inequivalent lattice points. $\vec{a}_1$ and $\vec{a}_2$ are the unit vectors. (b) The corresponding reciprocal lattice of (a). The first Brillouin zone is shaded in light blue. Here high symmetry points, Γ, K and M have been labeled. $\vec{b}_1$ and $\vec{b}_2$ are the reciprocal lattice vectors.[3]

Due to the high symmetry of graphene with sp^2 hybridization, it is suitable to carry out tight binding calculation for this system. Saito *et al*.[3] have described the detailed method to get this. Here the dispersion relation is directly shown as below:

$$E_{g2D}(k_x,k_y)=\pm t\sqrt{1+4\cos(\frac{\sqrt{3}k_x a}{2})\cos(\frac{k_y a}{2})+4\cos^2(\frac{k_y a}{2})}, \qquad (1.4)$$

where the parameter t = -2.7eV and the lattice constanct $a = |\vec{a}_1| = |\vec{a}_2|$ =2.46Å.[4]

The energy dispersion of graphene throughout the Brillouin zone is shown in **Figure 1.3**. The upper and lower surfaces are the allowed energy value for different electron momentum states and are called conduction and valence band, respectively. Meanwhile, at K points, plugging the coordinates of them into Equation 1.4 will result in $E_{g2D}(k_x, k_y)$=0, which means that the two bands touch each other just at the vertices or K points of the Brillouin zone, called Dirac points.

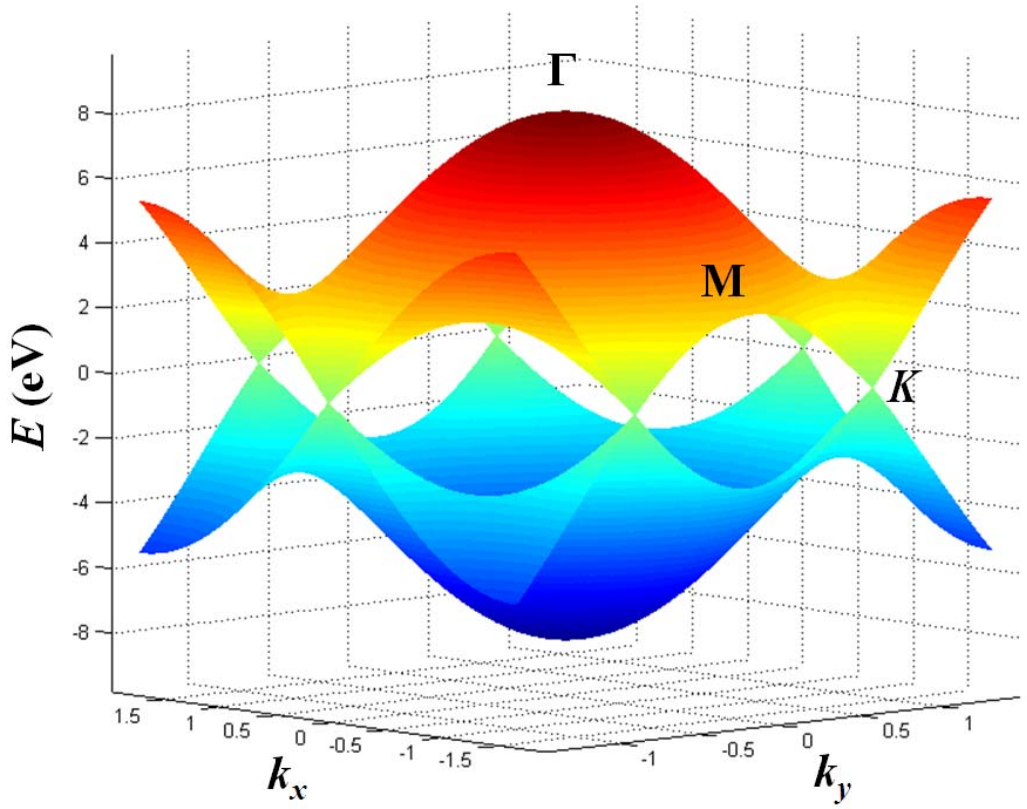

Figure 1.3 Band structure of graphene throughout the region of the first Brillouin zone. The red upper surface is the conduction band and the blue one is the valence band. The two bands touch at the Dirac points. Here high symmetry points, Γ, K and M have been labeled in the graph.

For sp^2 hybridization, there are two π electrons per unit cell and these two π electrons fully occupy the valence band of graphene, which makes graphene be a zero band-gap semiconductor.[3] However, of particular interest here is the rolling of a graphene layer to a cylinder, or a single-walled carbon nanotube (SWCNT).

1.2.2 Electronic band structure of SWCNT

When graphene is rolled over to the tubular structure of SWCNT, there is the periodic boundary condition characterized by the chiral vector, $\vec{C}_h \cdot \vec{k} = 2\pi n$ (n is an integer), which causes a quantization of the wave vector along the circumferential direction. Here two reciprocal lattice vectors can be defined first: $\vec{K}_{\parallel}$ along the CNT axis and $\vec{K}_{\perp}$ in the circumferential direction.[3] Based on this definition, the allowed wave vector $\vec{k}$ can be expressed by $\vec{k} = A\vec{K}_{\perp} + B\vec{K}_{\parallel}$, in which A is an integer due to $\vec{K}_{\perp} \cdot \vec{C}_h = 2\pi$. For $\vec{K}_{\parallel}$ direction the wave vector $\vec{k}$ remains continuous. From reference,[3] we can directly express the two reciprocal lattice vectors as below:

$$\vec{K}_{\perp} = \frac{1}{2}\left(\frac{\sqrt{3}a_{c-c}}{\left|\vec{C}_h\right|}\right)^2((2n+m)\vec{b}_1 + (2m+n)\vec{b}_2), \tag{1.5}$$

$$\vec{K}_{\parallel} = \frac{1}{N}(m\vec{b}_1 - n\vec{b}_2), \tag{1.6}$$

where N is the number of hexagons per unit cell of a SWCNT. [3]

Actually, whether SWCNT is a semiconductor or metallic tube depends on if the allowed wave vector $\vec{k}$ intersects through the Dirac points or K points. If it misses the points, then this creates a semiconducting nanotube with a range of energy gap where no electron states can exist. If the allowed wave vector $\vec{k}$ contains the Dirac point, where the conduction band and the valence band cross each other without gap, this will result in a metallic nanotube.

In this case, it is necessary to analyze the allowed $\vec{k}$ in the region of the Brillouin zone around K points. In **Figure 1.4**, the energy dispersion relations of graphene are shown in 2D Brillouin zone. Here we use (5,2) (**Figure 1.4a**) and (4,0) (**Figure 1.4b**) CNTs as examples to show how the quantized allowed $\vec{k}$ to determine the CNT electronic properties. When the chiral vector $\vec{C}_h = n\,\vec{a}_1 + m\,\vec{a}_2$ is defined, this means the direction of reciprocal lattice vectors $\vec{K}_{\parallel}$ and $\vec{K}_{\perp}$ is also fixed, especially that $\vec{K}_{\perp}$ is parallel to $\vec{C}_h$. Thus, in 2D Brillouin zone along the $\vec{K}_{\perp}$ direction we can find out two K points that are the farthest from Γ point. Through a K point an imaginary dashed line H along $\vec{K}_{\perp}$ direction intersects with a continuous wave vector line (red lines in **Figure 1.4**) along $\vec{K}_{\parallel}$ direction. $\vec{K}_{\parallel}$ and $\vec{K}_{\perp}$

are perpendicular to each other, so we can obtain the relationship as below:

$$\mathrm{H}=\overrightarrow{\Gamma K}\cdot\frac{\vec{K}_{\perp}}{\left|\vec{K}_{\perp}\right|} \tag{1.7}$$

Each K point has a corresponding K' point with the opposite coordinates, so H= H'. In section 1.2.1 reciprocal lattice vectors $\vec{b}_1$ and $\vec{b}_2$ have been given and so the coordinate of K point can easily got. Using Equation 1.5 we can obtain:

$$\mathrm{H}=\frac{2n+m}{3}\left|\vec{K}_{\perp}\right| \tag{1.8}$$

If 2*n*+*m* is divided by three, then 2*n*+*m*-3*m*= 2(*n*-*m*) can be also divided by three and so *n*-*m* should be a multiple of three. Thus, H is an integer multiple of $\left|\vec{K}_{\perp}\right|$, which means the allowed wave vector $\vec{k}$ intersects the K (or K') point, and so in this case the CNT is metallic tube without bandgap, shown in **Figure 1.4a** as an example. Reversely, if *n*-*m* is not a multiple of three, $\vec{k}$ will miss the K (or K') point and a bandgap (~1eV) will be created between conduction band and valence band. The tube is semiconducting, like the (4,0) CNT in **Figure 1.4b**.

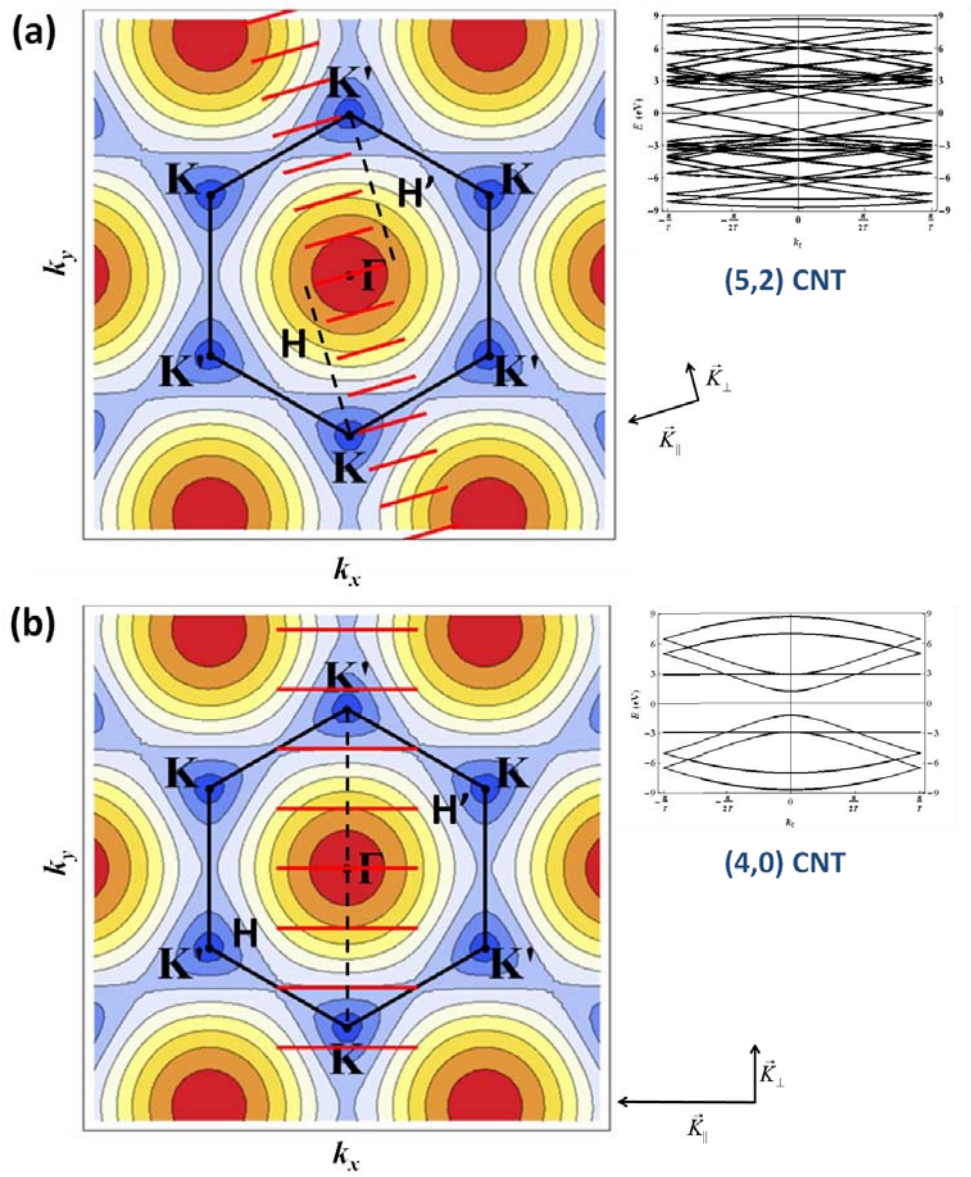

Figure 1.4 The one-dimensional wave vectors $\vec{k}$ (red lines) are shown in the 2D Brillouin zone of graphene for (a) (5,2) metallic CNT and (b) (4,0) semiconducting CNT. H (H') is an imaginary line passing K (K') point and parallel to the chiral vector $\vec{C}_h$ direction. The inset graphs in both (a) and (b) are the corresponding energy dispersion in 1D Brillouin zone.[5]

2. NANOTUBE SYNTHESIS AND DEVICE FABRICATION

2.1 Ultralong Single-walled Carbon Nanotubes Growth by Chemical Vapor Deposition (CVD) Method

2.1.1 Method

We have used two kinds of catalysts for CNT growth by chemical vapor deposition (CVD): block copolymer-templated cobalt nanoparticles[6] and ferritin-based iron nanoparticles[7]. Here the block copolymer method, as a typical CVD method, will be described in detail. The growth result of the both two methods will be shown at the end of this section.

In the CVD method, the cobalt (Co) nanoparticles are used as catalysts and ethanol provides the carbon source, and this method shows great performance in SWCNT growth with control over orientation, length, and diameter.[8] The growth mechanism of SWCNTs by CVD method involves the dissociation of ethanol molecules catalyzed by a transition metal, and followed by the dissolution and saturation of carbon atoms in the metal nanoparticles. The precipitation of carbon from the saturated metal particle leads to the formation of tubular carbon solids in sp^2 structure. Tubule formation is favored over other forms of carbon such as graphitic sheets with open edges. This is because a tube contains no dangling bonds and therefore is in a low energy form.[2] At high temperature, carbon has finite solubility in this metal, which leads to the formation of metal-carbon

solution and therefore forms the SWCNTs. The SWCNTs grown in this way can be 1 ~ 2nm in diameter. The longest SWCNT we have grown can reach 1.05 cm.

2.1.2 Experiment setup

Figure 2.1 shows the experiment set up. Hydrogen (H_2) is used as reducing gas and argon (Ar) as protective gas in the CVD method. The two gases will first pass through drying units (DRIERITE) and filters (Swagelok), removing the water vapor and other impurities. The flow rate of the two gases is meansured and controlded by mass-flow controller (MKS type 1179) in this growth system. After passing the mass-flow controller, there are two channels for gas flow as shown in the top view of **Figure 2.1a**. The lower one is just used to send gas, for warming up the tube furnaces and removing the polymer on silicon substrate; the upper one is used to deliver the ethanol, kept in an ice/water bath (0 ˚C), into the tube furnace (Lindberg/Blue, mini-mite 1100˚C Tube furnace, single zone), where the SWCNT growth takes place. The tube furnace and the placement of the silicon wafer chip are schematically shown in **Figure 2.1b.**

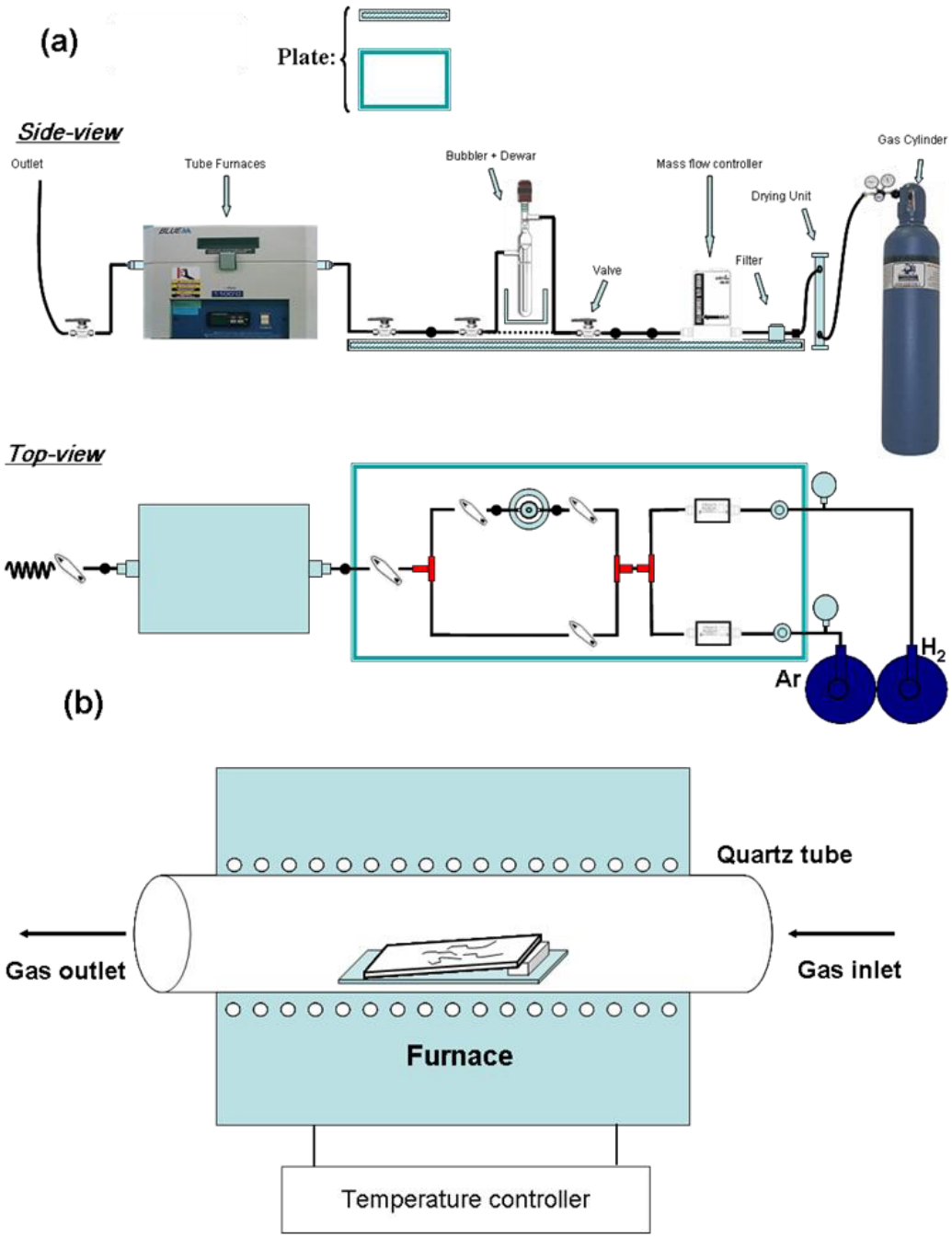

Figure 2.1 (a) Experiment setup: side-view and top-view; (b) schematic diagram of the ethanol chemical vapor deposition (CVD) in the tube furnace (one inch diameter quartz tube, 15 inch heating zone), where the CVD growth of SWCNTs is performed over cobalt nanoparticles.

2.1.3 CNT growth procedure

2.1.3.1 Catalyst preparation. We used the block copolymer method[6] to synthesize transition metal cobalt nanoparticles with uniform size and distance between each other, which can offer promise for the diameter- and position-controlled growth of carbon nanotubes.[8] The polymer is Poly(styrene-b-4-vinyl pyridine) (PS-P4VP) (Mn-PS-b-4VP: 10400-b-19200; PDI: 1.27), from Polymer Source, Inc. The raw transition metal cobalt is from cobalt (II) acetate $(CH_3CO_2)_2Co$ (Sigma-Aldrich Inc.). 0.05 g of PS-P4VP di-block copolymer was added into 12.5 ml toluene and stirred at 70°C for 4–5 hours. Subsequently, 1.1 mg of $(CH_3CO_2)_2Co$ powder was added to the block copolymer solution and stirred for 24 hours at 30°C. With this process, the cobalt nanoparticles will be homodispersed in the polymer. The size of metal cobalt particles, of the order of nanometers, will have control over the diameter of grown SWCNTs. In order to synthesize SWCNTs of comparable diameters, a uniform nano-structure of the cobalt catalyst has to be prepared very carefully. PS-P4VP block copolymer forms micelles in toluene which are capable of self-organizing into ordered structures on substrates. Interactions between the transition metal Co ions and the pyridine group were utilized to sequester metal ions in the spherical domains (nanoreactors) to form monodisperse metal nanoclusters. Coordinated covalent bonds are formed as a result of the interaction between the lone

pair of electrons associated with the nitrogen atom in the pyridine group and cobalt with partially filled 3d orbital.

2.1.3.2 Catalyst Oxidation. A silicon substrate (15mm × 30mm) with 1.0 μm thick SiO_2 was cleaned by piranha solution (concentrated sulfuric acid to 30% hydrogen peroxide solution at 3:1 ratio) and then rinsed by de-ionized water. After the transfer of the cobalt catalyst solution onto the edge of silicon substrate by PDMS stamps, the substrate was put on a quartz sample boat (15mm × 50mm) with the catalyst side facing the gas flow entrance and sent into the center of the 1 inch diameter quartz tube, shown in **Figure 2.1b**. The substrate with metal salt polymer was heated in the air at 750°C for about 15 min in order to oxidize the metal and to remove the polymer from the micelles.

2.1.3.3 Catalyst reduction. The CNT growth can be improved better if the substrate is tilted by slightly raising the catalyst side of the substrate. As shown in **Figure 2.1b**, the substrate is tilted about ~5 degree by inserting a small piece of quartz block under the substrate at the catalyst side. With argon flow rate at 300 standard cubic centimeters per minute (sccm) and hydrogen at 110 sccm, the temperature of the furnace will ramp up to pre-set 900°C with ramp rate of 18°C /min. The reduction time is about 20 minutes.

2.1.3.4 CNT growth. The furnace is set at 900°C and the hydrogen gas flow rate is reduced to lower value (hydrogen at ~32 sccm and argon at ~320 sccm). The nanotube growth begins at the time when the valves are switched to allow ethanol vapor to go into the furnace (**Figure 2.1a** top view). The growth is normally carried out for one hour.

2.1.3.5 Finish. After growth, the hydrogen is stopped. The quartz tube is allowed to cool down to lower than 100°C with argon flow at ~320 sccm. The substrate is then cleaned with acetone, isopropanol and deionized water and kept in water to avoid contamination while waiting for the investigation by scanning electron microscope (SEM).

2.1.4 Results

Oriented single-walled carbon nanotubes are grown out from the cobalt catalyst area and their growth direction are almost parallel to each other, as shown in the SEM image in **Figure 2.2a**. The well-oriented and isolated single-walled carbon nanotube can even reach longer than 1 cm routinely along the gas flow direction. With the observation via SEM a detailed image of one carbon nanotube shows it is very straight on the surface of the substrate as shown in **Figure 2.2b**. A typical atomic force microscopy (AFM) tapping mode image of an as-grown CNT by cobalt catalyst and the CNTs diameter distribution are shown in **Figure 2.2c** and **Figure 2.2d**.

Besides, the other kind of catalyst, ferritin, was also tried to use for the growth of CNT with bigger diameter. Iron loaded ferritin catalysts were produced following the procedure by Li et al.[7] with a theoretical loading of ~1200 Fe(III)/ferritin. By using the ferritin catalyst, we can also grow CNTs on SiO_2 or Si_3N_4 substrates. Actually, a large fraction of CNTs grown by this way showed high electrical conductivity, which is attributed to large diameter SWCNTs or few-layer MWCNTs.[9] The diameter distribution measured by AFM is shown in **Figure 2.2e**.

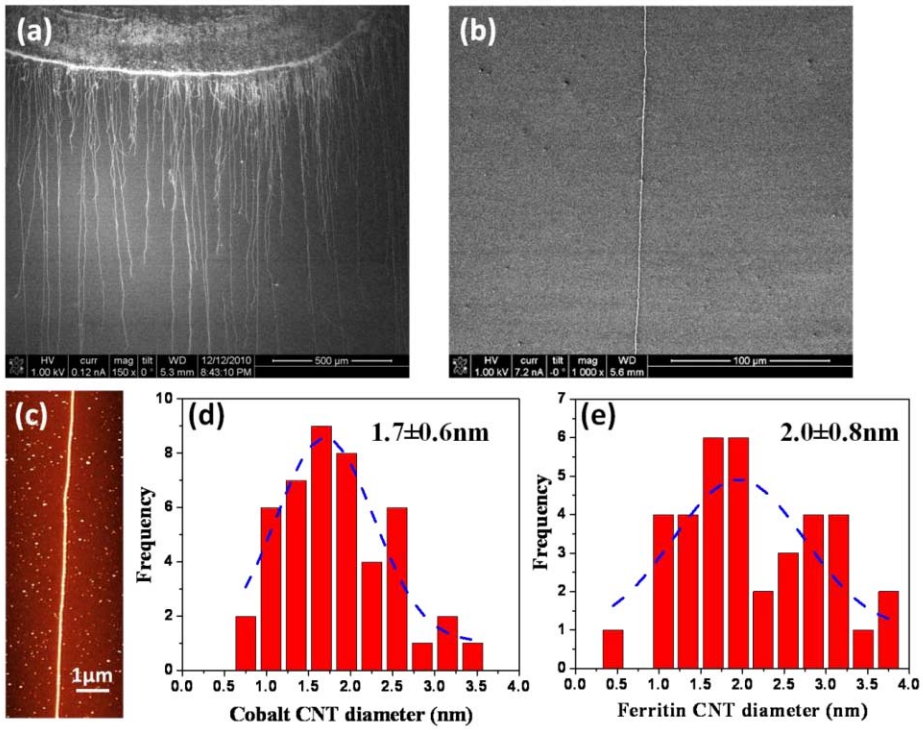

Figure 2.2 (a) Overall view of SWCNTs grown out of the catalyst area by SEM. (b) A SEM image of one straight as-grown SWCNT. (c) AFM image of a CNT (cobalt as catalyst) on SiO_2/Si substrate after growth. The height of the CNT measured by AFM was used to determine the diameter of the CNT. (d) A typical diameter distribution of CNT by cobalt method. A Gaussian fit gives the mean diameter 1.7±0.6 nm. (e) A typical diameter distribution of CNT by ferritin method. A Gaussian fit gives a mean diameter of 2.0±0.8 nm.

2.2 The Deposition of Markers and Contact Electrodes

Among various techniques for the manufacture of the practical electronic devices is the lithography which is used to put the designed patterns onto the surface of the substrate. Photolithography (or "optical lithography"), an extensive and sophisticated lithography technique, uses light directly through a photo mask to transfer a well-designed geometric pattern to a polymer resist layer, or called as photoresist, on the substrate.

Photoresists are classified into two groups: positive resists and negative resists. A positive resist is a type of photoresist in which the portion of the photoresist that is exposed to light becomes soluble to the photoresist developer. The portion of the photoresist that is unexposed remains insoluble to the photoresist developer. A negative resist will be reverse correspoinding to the positive one.

Here in our study, the image reversal technique by using AZ 5214 photoresist will be introduced due to its benefit for the lift-off process. AZ 5214 is a positive photoresist and the parameters exposure dose, reversal bake time and temperature, and development time have great impact on the profile of the final patterns. Image reversal process actually reverses the action of positive photoresist so negative images can be formed with the same resolution. **Figure 2.3** are schematic illustrations showing the

image reversal process by using AZ 5214 photoresist, which is spin-coated (4000 rpm for 30 seconds) onto the silicon wafer chips and the thickness is around 1.3 μm. An EVG® 620 Automated Mask Alignment System is the photolithographic instrument we use. The designed mask patterns are transferred onto a transparent glass with chromium material. When the UV light exposes (dose: 35mJ/cm^2) through the mask patterns, the exposed photoresist area becomes soluble in developer. Here the dose parameter is optimized, so the slope of the photoresist profiles or sidewall is not normal to the substrate, which means the exposed area is just like a trapezoid from the view of the cross-section, shown in **Figure 2.3b**. Then the chips are transferred to reversal bake at 115 $^{\circ}$C for 2 min, which leads to the crosslinking of photoresist in the exposed area while the unexposed area remains photo-active (**Figure 2.3c**). Then flood exposure (dose: 110 mJ/cm^2) without a mask then makes the photoresist, which is not exposed in the first expose step, soluble in developer, shown the **Figure 2.3d** to **Figure 2.3f**. By using thermal evaporation of Cr/Au with 5nm/40nm onto the developed chips, followed by the lift-off step in dichloromethane and acetone, the designed patterns can be transferred onto the silicon wafer chips (**Figure 2.3g** and **h**). **Figure 2.3i**, as an example, shows the index markers on the chips, by which we can find the coordinates of SWCNTs on the chips by scanning electron microscope

(SEM) and carry out the alignment step in the subsequent fabrication of contact electrodes by electron beam lithography (EBL).

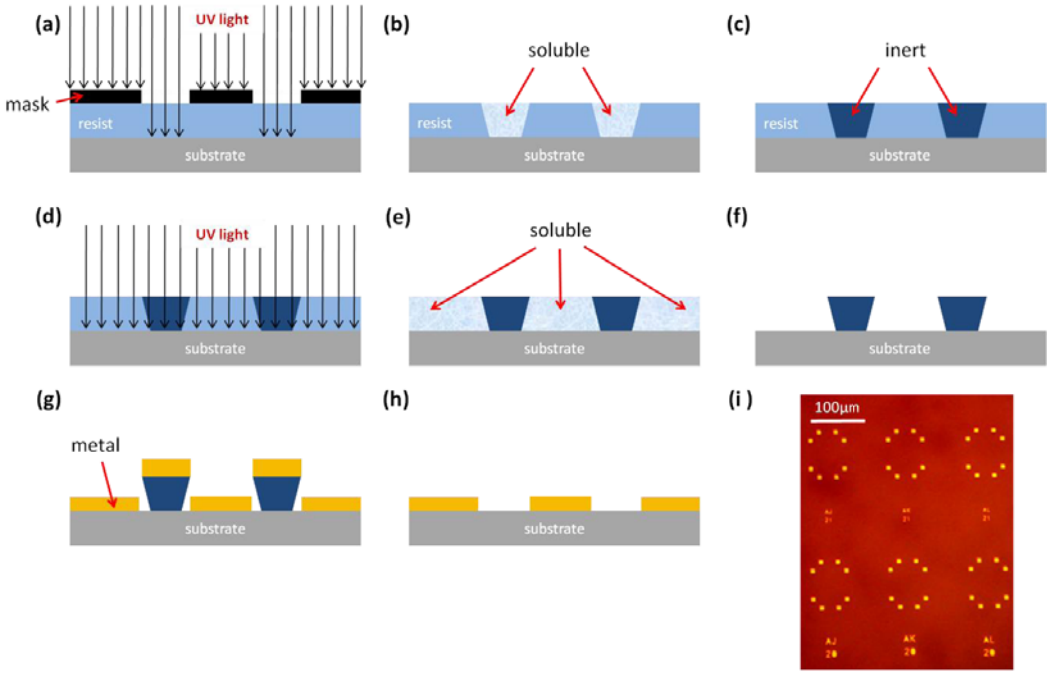

Figure 2.3 Schematic illustration of image reversal process. (a) Exposure by UV light through mask. (b) The exposed positive photoresist becomes soluble. (c) The reversal bake crosslinks the exposed area, while the unexposed area remains photoactive. (d) Without mask the flood exposure is carried out. (e) Exposed photoresist becomes soluble. (f) After development, the areas exposed in the first exposure step (b) now remain. (g) Thermal evaporation of metal film (Cr/Au) onto the chips. (h) The metal film is removed by lift-off. The metal film at mask area with the designed dark patterns is left. (i) A typical optical image of gold alignment markers on the surface of a silicon wafer fabricated by image reversal technique.

In our study, both of the SWCNT based nanofluidic devices and CNT field effect transistors (CNT-FETs) are made in order to obtain the ionic current through individual SWCNT and the SWCNT electric properties,

respectively. However, there is a fabrication limit for photolithography: the mask is just for general use (like the fabrication of alignment markers) but not amenable to customization. The SWCNTs grown by CVD method are randomly distributed on the silicon wafer chip and we cannot make a mask for all of specific device (reservoir or contact electrode) fabrications. In this case, electron beam lithography (EBL) is an ideal instrument which can directly pattern the device structures specifically and meanwhile the feature size can be even down to even tens of nanometers due to the high resolution e-beam exposure. Poly(methyl methacrylate) (PMMA) is the e-beam resist, which can be removed by the development after the e-beam exposure. Here for our device fabrication, EBL is used to make the electrical contact electrodes (**Figure 2.4a**) for measuring CNT electric properties (CNT-FET device with back gate electrode). Besides, the top gate electrode and the fluid reservoirs are also fabricated by EBL to create the CNT based ionic field effect transistors (ionic FETs), as shown in **Figure 2.4b**. These devices will be discussed in detail in the following chapters.

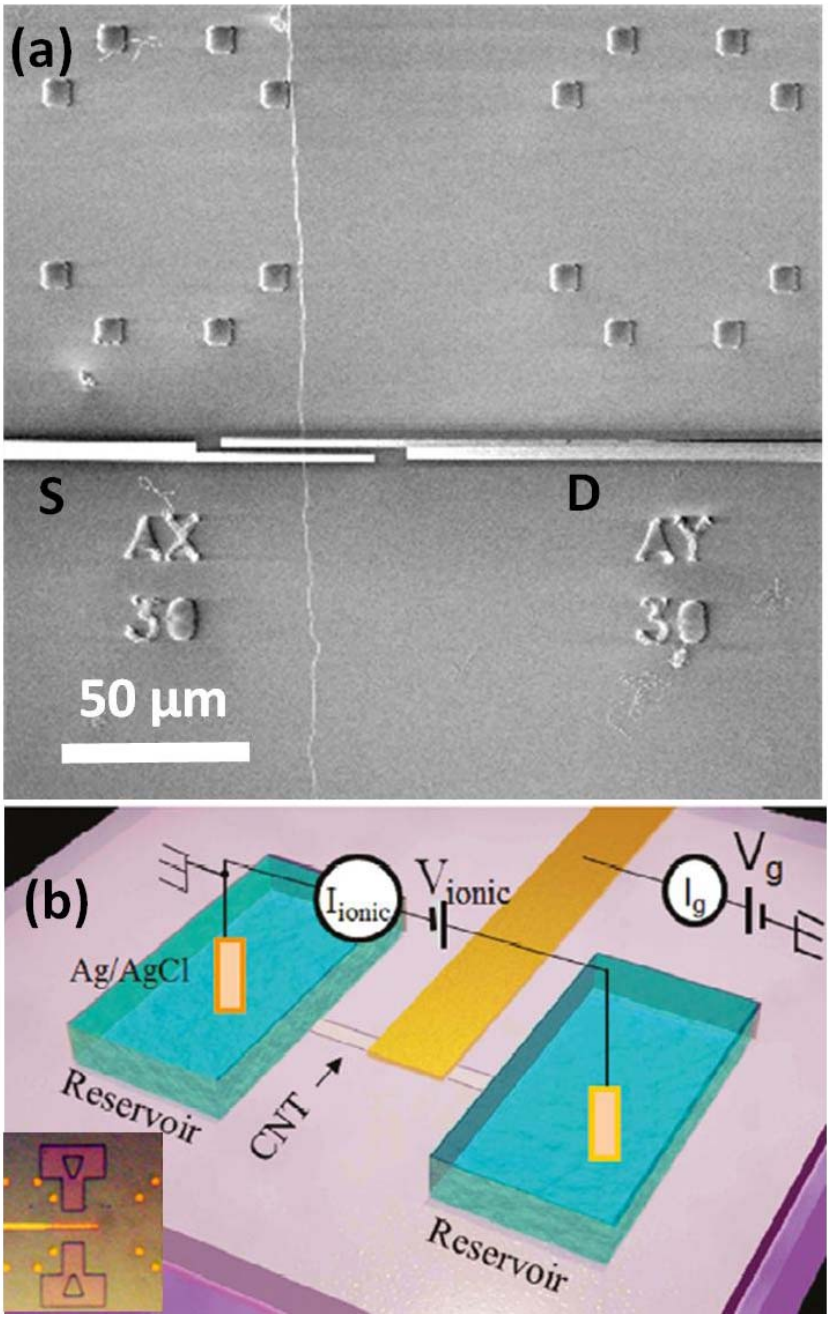

Figure 2.4 Patterns fabricated by electron beam lithography (EBL). (a) SEM image of gold sour-drain electrodes connecting one SWCNT working as CNT-FET. Back gate electrode is set at the back surface of the silicon wafer chip, not shown here. (b) Schematic of a CNT based ionic field effect transistor (ionic FET), including the top gold gate electrode and two fluid reservoirs connected by one SWCNT. Inset is the optical image of this kind of device.

2.3 Fabrication of the PDMS Microfluidic Delivery Device

2.3.1 Polydimethylsiloxane (PDMS)

Microfluidic devices offer significant benefits to physical and biological analysis in scientific research. The fabrication of microfluidic delivery devices[10, 11] which can be easily sealed onto poly(methyl methacrylate) (PMMA) film with good sealing conditions leads to the choice of polydimethylsiloxane (PDMS). **Figure 2.5** shows the chemical structure of PDMS. Due to the stable crosslinked network, PDMS offers advantages on chemical resistance, flexibility and can be even used as encapsulants in application. Here we use PDMS to manufacture the microfluidic delivery devices, which introduces the solution into the fluid reservoirs of SWCNT based nanofluidic devices referred in last section.

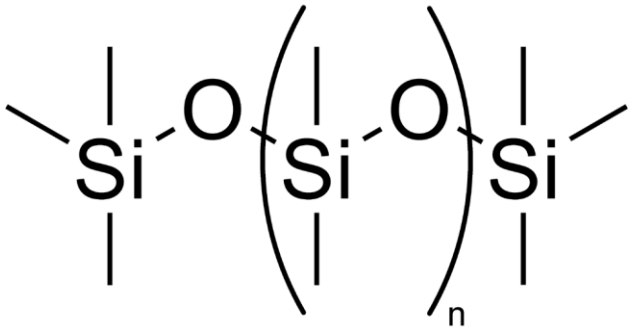

Figure 2.5 Chemical structure of polydimethylsiloxane (PDMS) where crosslinking occurs.

2.3.2 Master fabrication

For the fabrication of PDMS microfluidic device there are two key challenges, the creating of the embedded microchannels and the good sealing between inlet/outlet stainless steel tubes and holes drilled in PDMS block.

The microchannel design is shown in **Figure 2.6a**. There are two layers in the PDMS device, the lower layer (shown in red) and upper layer (shown in blue). The two channels (red lines) in the bottom layer are separated by 30 μm. In order to provide reliable sealing, a PDMS stamp with embedded channels is used to avoid any possible leakage caused by stamp deformation. The mold of microfluidic channel pattern is prepared by deep reactive ion etching (deep RIE) method. Image reversal technique is also used to make these microchannel patterns (protected by photoresist) on the silicon wafer, then followed by the deep RIE to etch away the uncovered SiO_2/Si to around 50 μm in depth. The wafer containing the mold was silanized overnight with silanizing agent (tridecafluoro-1,1,2,2-tetrahydrooctyl trichlorosilane) in order to make its surface hydrophobic so that the PDMS will not bind with it in curing process. After this the molded wafer can be used as a "master" for creating the PDMS device, as shown in **Figure 2.6b** and **Figure 2.6c**.

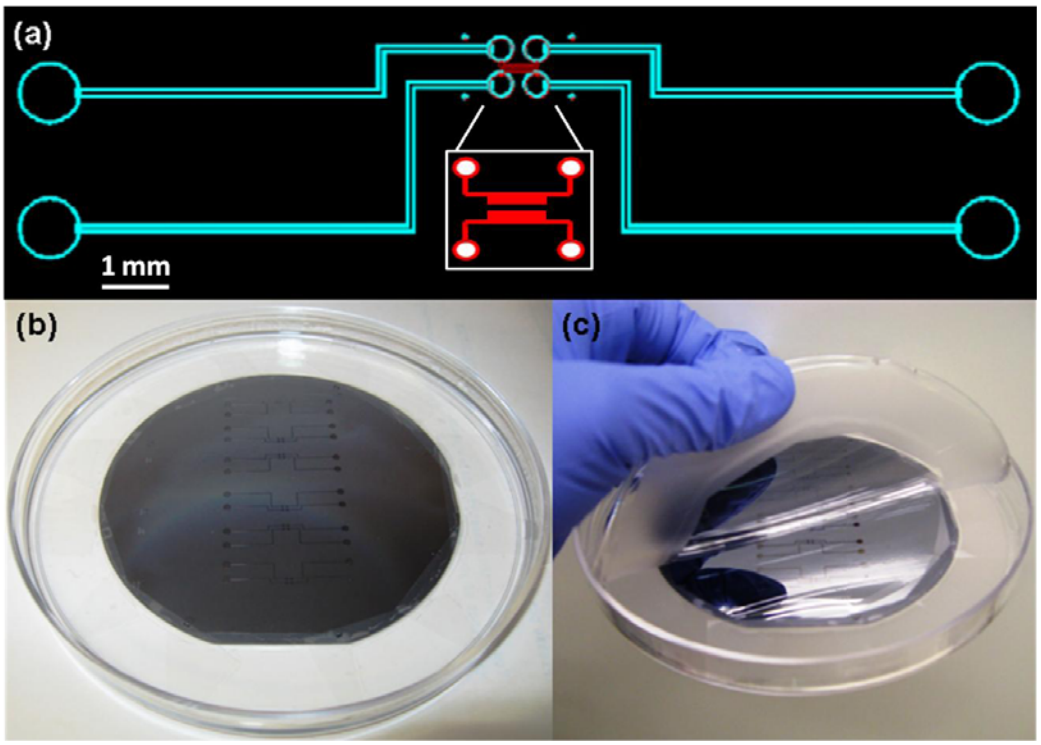

Figure 2.6 (a) Schematic design of PDMS stamp with two layers of microchannels: red lines (—) indicate the microchannels in the lower layer (inset) and blue lines (—) represent the ones in the upper layer. The channels in lower and upper layers are connected by the four small holes in the center. (b) Silicon master for creating the PDMS device sealed in petri dish. (c) Cured upper PDMS layer is peeled off from silicon master

2.3.3 PDMS microfluidic device

The PDMS prepolymer (Sylgard 184 Silicone Elastomer Base, Dow Corning) is mixed with its curing agent at a volume ratio of 10:1. The mixture is then degassed in a desiccator under vacuum (~40 torr) for about 40 minutes until all air bubbles are totally removed. The PDMS is cast onto the prepared silicon mater wafer and then hardened for 48 hours at room temperature (~22°C).

The interconnecting holes are punched prior to bonding the two PDMS layers together. The coring tube (tool) is made of a stainless steel (SS) with 838 μm in inner diameter and the profile is like a sharp, beveled edge needle, as shown in **Figure 2.7a**. The cored hole was created by pressing the coring tool through the PDMS to the embeded microchannel and pulling it out with a twisting motion, by which the core part in the hole can be taken out (step Ⅰ to Ⅲ in **Figure 2.7b**). The cored hole has a diameter identical to the inner diameter of SS tube (838 μm).

Once the holes for the interconnection are created, the top and bottom PDMS layers can be treated in oxygen plasma (29.6 W at 550~600 mTorr) for 40 seconds to activate the PDMS surface. After proper alignment under an optical microscope, the two layers are brought into contact and then baked at 65°C for 1 min. When another stainless steel tube with outside diameter of 902 μm is inserted into the drilled hole, a compression seal is formed around the tube (step Ⅳ in **Figure 2.7b**) and the interconnection between the microchannels in PDMS stamp and the outside world is built. Standard silicon tubings are used to connect the stainless steel tube and the syringe works as the output pump, shown in **Figure 2.7c**. Then a complete set of PDMS microfluidic delivery device is done, shown in **Figure 2.7d**, which can be integrated with the SWCNT based nanofluid device.

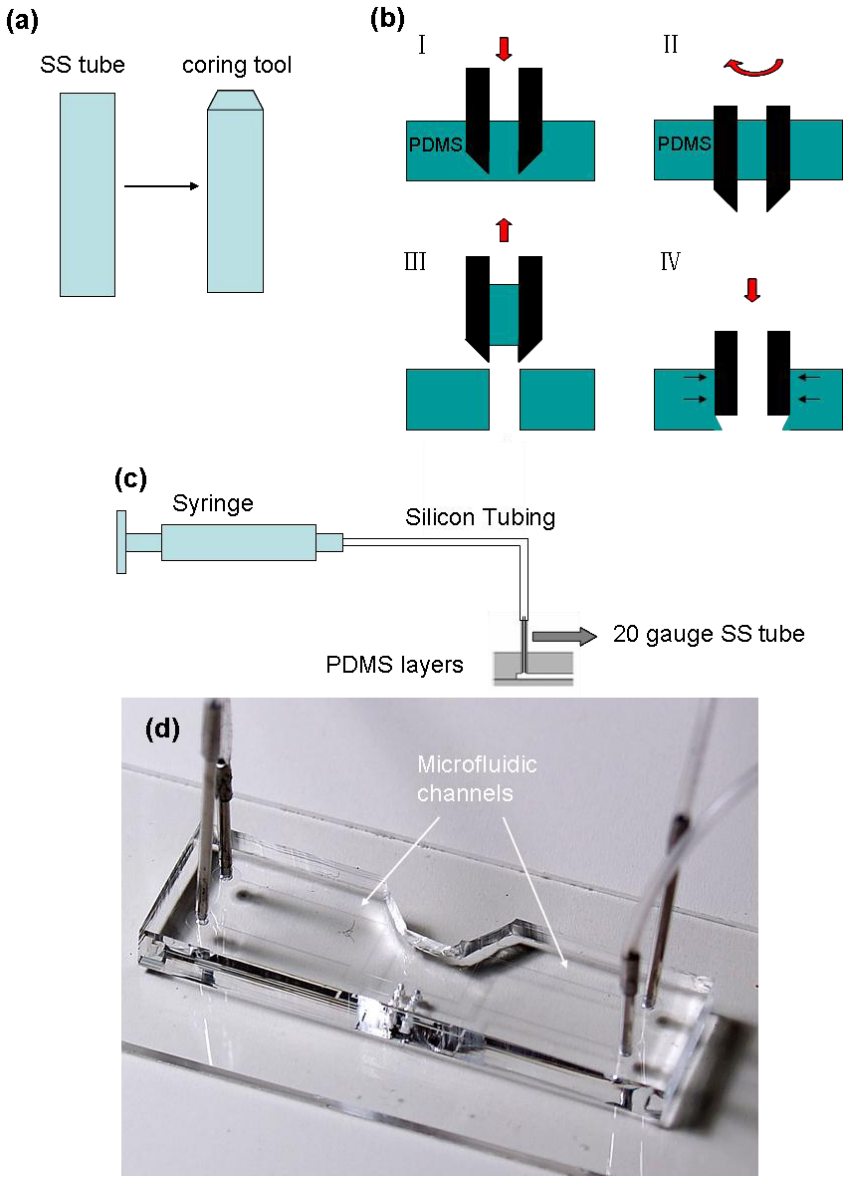

Figure 2.7 (a) Schematic coring tool: a sharp, beveled edge needle (838μm in inner diameter). (b) Schematic process to make cored hole and insert the tube into it: I. press the coring tool through the PDMS layer; Ⅱ. twist the tool to cut the core part away from the whole block; Ⅲ. pull out the core part in the hole, Ⅳ. Insert a stainless steel tube (902μm in outside diameter) into the drilled hole, which leads to good sealing between it and the PDMS layer. (The red arrows indicate the direction of the force applied on the tool or tube). (c) Illustration of the interconnection between syringe and the PDMS microfluidic channel. (d) A complete set of PDMS microfluidic delivery device on a glass slide.

3. ION TRANSPORT IN NANOFLUIDIC CHANNELS

3.1 Ion Channel and Electrical Double Layer

Inspired by nature's delicate creation of the nanofluidic system, namely, the ion channels inside of transmembrane protein, we applied the carbon nanotubes (CNTs), due to their hydrophobic inner walls and nanometer channel size, as perfect artificial candidates in the form of nanofluidic channel/pore devices to mimic and study the mechanism of ion and biomolecular transport process.

The first step to understand the ion transport in nanofluidic channels is to understand the electrostatic interaction in ionic solutions. Here we consider the liquid is in proximity to a charged surface, mostly due to mechanism such as ionization, ion adsorption and ion dissolution. For example, when the thermally grown SiO_2 surface is stored in ambient air, it consists of Si-OH silanol groups.[12] When the surface is brought into contact with water solution (pH>3), the silanol groups behave as an acid and donate protons to water.[13] Thus, the channel surface obtains a small negative charge ($Si\text{-}O^-$). When electrolyte solution is introduced into the channel, the counterions are electrostatically attracted to such a surface to maintain the electroneutrality of the solid-liquid interface, while the coions are repelled. This can form a screening region, composed of two layers of shielding countions, called electrical double layer (EDL),[14, 15] shown in

Figure 3.1. The first layer, adjacent to the surface, is Stern Layer with immobile ions adsorbed to the charged surface, while the second one with mobile ions is diffuse layer. The interface between the two layers is the shear plane or slip plane, at which the zeta potential ζ is defined. A characteristic length of EDL, λ_D, over which the electric potential decays to its bulk value, is called the Debye screening length,

$$\lambda_D = \sqrt{\frac{\varepsilon_r \varepsilon_o k_B T}{2nz^2 e^2}}$$

where ε_r is the dielectric constant of water, ε_o is the permittivity of vacuum, k_B is the Boltzmann constant, T is the absolute temperature, n is the bulk ion concentration, z is the valency of the ions, and e is the charge of an electron.[15] Normally, λ_D is between 1 and 100 nm under most ionic conditions.

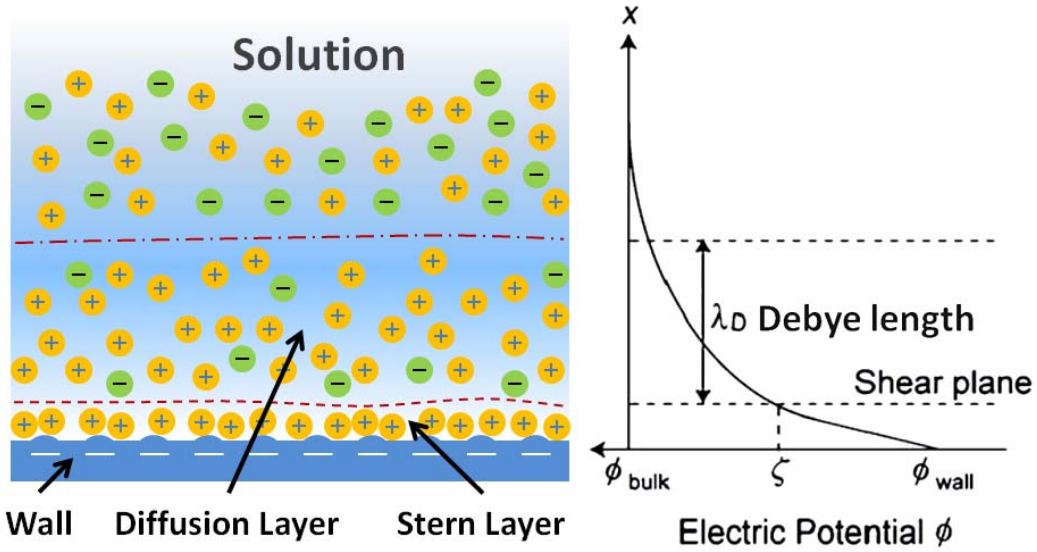

Figure 3.1 Illustration of the electrical double layer (EDL) and electric potential profile normal to the negatively charged wall.

In a nanochannel with the charged wall, the channel dimension normally is comparable to or smaller than Debye length λ_D, which means the entire region inside the channel is within EDL. In this case, the channel will be filled with unipollar solution of counterions, because of ion screening effect (**Figure 3.2**); the electric potential is not equal to the bulk potential; and the counterion concentration is higher than the bulk concentration. Whereas in a microchannel, whose dimension is much larger than λ_D, the solution inside will keep neutral or bulk state. Both of the electric potential and counterion concentration decay to bulk value rapidly within a distance of the order of λ_D (**Figure 3.2**).

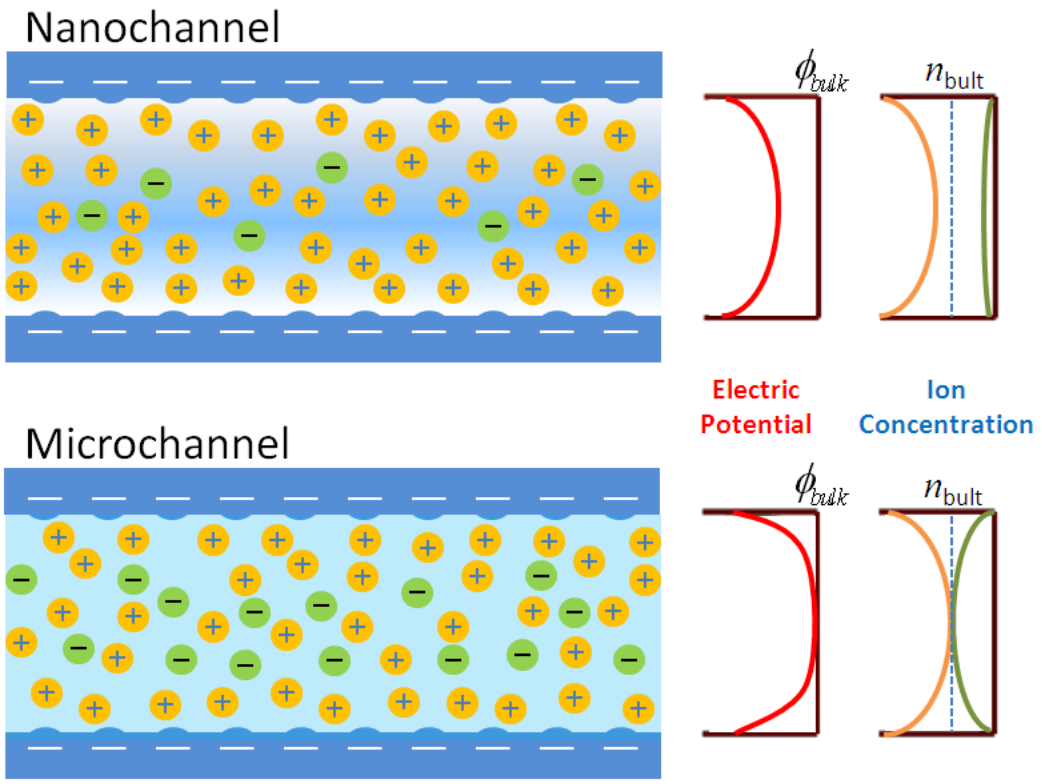

Figure 3.2 Surface charge effects in nanochannel and microchannel. *Left side*: in a nanochannel, the solution is charged when the Debye length is larger than the channel dimensions, whereas in a microchannel, the Debye length is typically much smaller than the channel dimensions and most of the solution in the channel is neutral. *Right side*: the electric potential (red) in the nanochannel is not equal to the bulk potential (ϕ_{bulk}) even at the center of the channel, whereas the electric potential in the microchannel decays rapidly to its bulk value (ϕ_{bulk}) in a distance of the order of the Debye length. The counter-ion concentration (orange) in a nanochannel is much higher than the co-ion concentration (green), whereas the concentration of cations (orange) and anions (green) in the microchannel is equal to the bulk concentration (n_{bult}).[16]

Based on the description above, the manipulation of surface charge density of the channel wall or the direct modulation of the counterion concentration by electrostatic field added by a gate electrode will have the control effect on the ion conductance in the channel. This kind of device is

called nanofluidic transistor,[16] which mimics the modulation of major carrier density to control the channel conductance of the tranditional metal-oxide-semiconductor field effect transistor (MOSFET). Here, for nanochannel device, the major carriers are the net excess of counterions in it. Nanoscale channels made of silicon nanotubes (inner diameter: ~50nm) with added gate electrodes have been employed to realize the electrostatic control of the movement of ions and molecules by Karnik *et al*.,[16] as shown **Figure 3.3**.

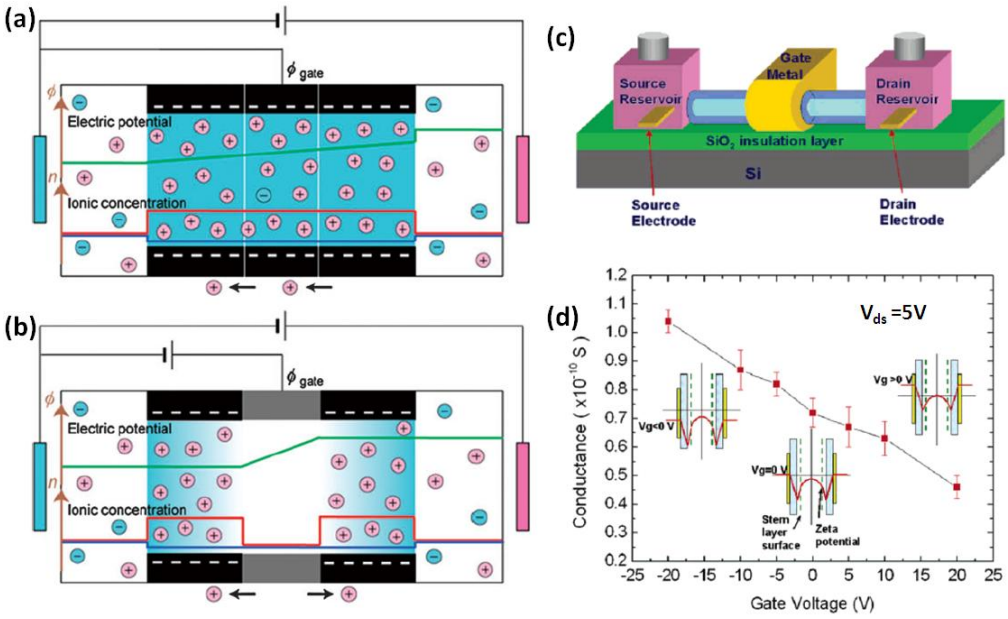

Figure 3.3 Schematic of ions, electric potential (green) and counter-ion concentration (red) in nanofluidic field-effect transistor without (a) and with (b) a positive gate potential.[15] (c) Schematic of a nanofluidic transistor based on a silicon dioxide nanotube with negative charges on the wall. (d) Ionic conductance through the silicon dioxide nanotube can be modulated by a gate voltage. The insets schematically illustrate the electric potential from the gate electrode and across the nanotube when applying negative, zero, and positive gate voltages, which accordingly modulates ionic density and conductivity.[16]

3.2 Electroosmotic Flow

Electroosmotic flow (EOF) is the movement of liquid adjacent to a stationary surface drawn by the net excess of couterions in the diffuse layer of EDL with a tangential electric field applied parallel to the interface, as shown in **Figure 3.4**. The migration of liquid is due to the viscous interaction. Normally at the shear plane (**Figure 3.1**), the liquid velocity is regarded as zero due the immobile ion in Stern layer, then increases to the maximum value and finally remains a constant, defined as electroosmotic velocity v_{eo} described by Smoluchowski:

$$v_{eo} = -\frac{\varepsilon_r \varepsilon_o \zeta}{\eta} E_z \tag{3.1}$$

where E_z is the electric field along the z direction and η is the viscosity of the fluid.[14]

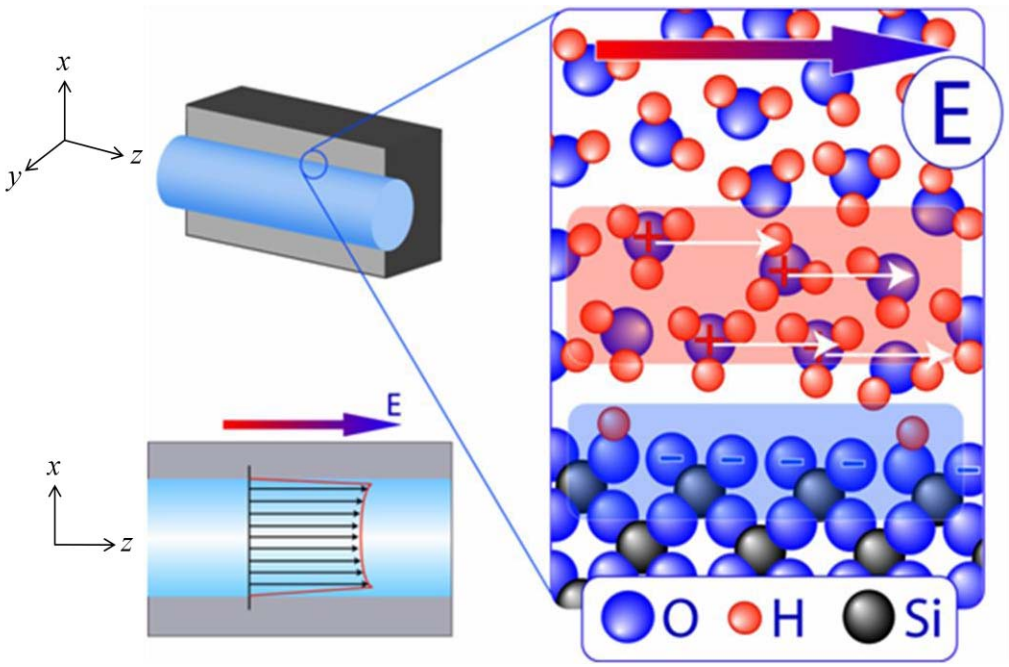

Figure 3.4 Electroosmotic flow (EOF).[13] When silicon dioxide surface, terminated by silanol groups (Si-OH), is brought into contact with water solution (pH>3), the silanol groups behave as an acid and donate protons to water. Thus, the channel surface obtains a small negative charge (zeta potential ζ <0) while the thin water layer carries a positive one. When applying a voltage, the charged water layer starts to move and if the channel is small enough, it drags the rest of the liquid with it.

When an externally applied EOF-generating voltage is applied across the fluid at the two ends of silica microchannel, the positive ions of the double layer move under along the direction of electric field, E, dragging the fluid with them by viscous coupling. Based on the Equation 3.1, the electroosmotic velocity v_{eo} is also related the zeta potential ζ. Thus, changing ζ of the channel wall can modulate the value of v_{eo} and even reverse its direction. Based on this idea, a flow field-effect transistor (flowFET) has been built by Schasfoort *et.,*[17] in which they applied a

perpendicular electric field between a third electrical contact (at the outside of the channel wall) and the bulk of the fluid, a way for spatial-controlled modification of ζ, to control the value (**Figure 3.5B**) and even the direction (**Figure 3.5C**) of EOF.

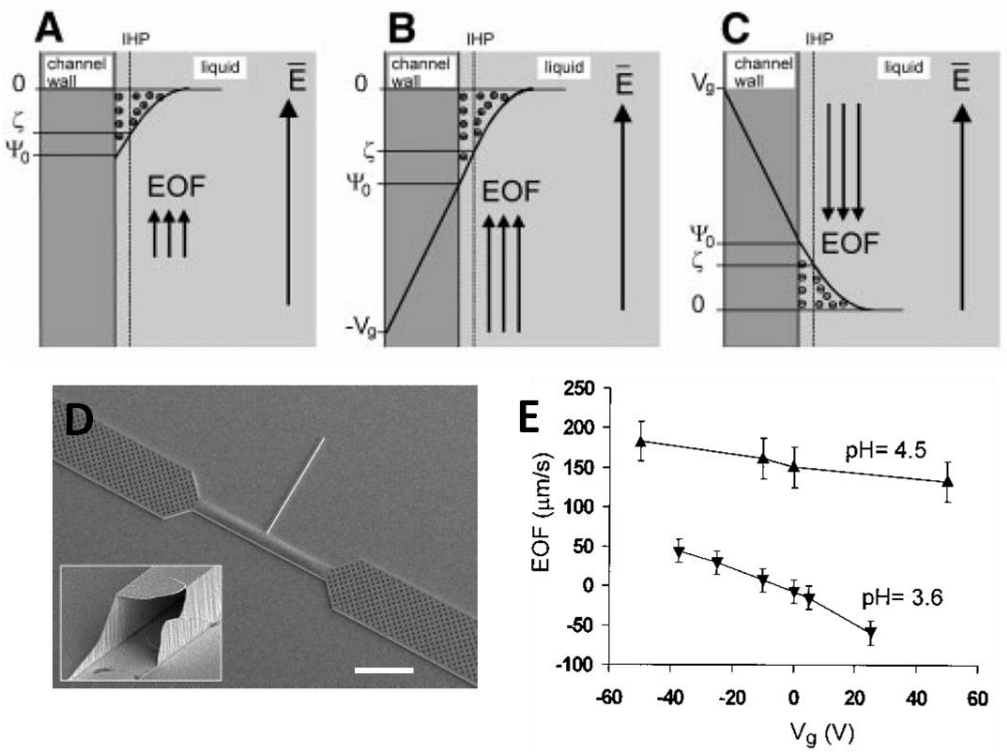

Figure 3.5 The influence of zeta potential ζ on EOF.[17] (A) The development of ζ and EOF without gate voltage. (B) An enhancing EOF with negative gate voltage. (C) An inverting EOF with positive voltage. (D) SEM image of the silica channel junction region (scale bar: 400 μm). Inset shows the side channel cross section (25μm x25μm) with insulating wall as 390nm thick. (E) EOF as a function of applied gate voltage Vg. For pH=3.6, the EOF direction can be reversed with positive gate voltage.

3.3 Theoretical Aspect: Continuum Dynamics

The theoretical analysis of our CNT based nanofluidic devices is built on the continuum model. Continuum dynamics is concerned with the kinematics and the mechanical behavior of materials modelled as a continuous mass rather than as discrete particles. Although the matter around us consists of small units, like atoms and molecules, the motion of individual such small particles is not the concern when the analysis target is put on the behavior of matter in some average sense, especially on a relatively large scale. In continuum dynamics, the material is treated as uniformly distributed throughout regions of space and meanwhile the quantities, such as density, velocity, displacement, *etc*. can be defined as continuous functions of position.[18] Specifically for fluid case, the Knudsen number Kn is useful for determining whether statistical mechanics or the continuum dynamics of fluid system should be used:

$$Kn = \frac{\lambda}{L} \tag{3.2}$$

where λ is mean free path of a moving particle (such as an atom or a molecule) and L is representative physical length scale. If Kn is smaller than one, the collision between the particles can be ignored, and the continuum assumption of fluid mechanics is a good approximation. For the CNT nanofluidic system, a typical mean free path in water is λ~3 Å and using the diameter of CNT as a characteristic system length (d = 2 nm), so the Knudsen number λ/d~0.1 is still small enough. Besides, there is

another dimensionless number for fluid dynamics, the Reynolds number Re, which is used to characterize different flow regimes, laminar or turbulent flow:

$$\mathrm{Re} = \frac{\rho v L}{\mu} \tag{3.3}$$

where ρ is the density of the fluid (kg/m³), v is the mean velocity (m/s), L is a characteristic linear dimension and μ is the dynamic viscosity of the fluid (N·s/m²). For our CNT based nanofluidic system, Re is normally at the order of 10^{-4} to 10^{-2}, indicating there is laminar or steady flow in it. Besides, this is also a micro-nano incompressible Newtonian fluid system. Thus, the continuum approximation is valid for the similuation of this system with conservations of mass, energy, momentum and charge.

The space-charge model is one of the most complete physical interpretations of ion transport through nanometer-sized channels, which are assumed to be straight and bear a surface charge. This model assumes ions as point charges, so the steric effects of the size of ions are neglected.[14, 19] Here a set of time-independent coupled partial differential equations, the Poisson-Nernst-Planck-Stokes (PNPS) equations, will be used to analyze the ion transport in the CNT channel.[14, 15, 20-22]

The Poisson equation (Equation 3.4) defines electrostatic scalar potential ϕ as response to the local excess electric charge, $\rho_e=(c_+-c_-)F$, in the environment of relative dielectric constant ε_r, where $c_\pm$ are the instantaneous volume densities of the positive (+) and negative (-) ions, and F is the Faraday constant.

$$\nabla\cdot\left(\varepsilon_r\nabla\phi\right)=-\frac{\rho_e}{\varepsilon_0},\quad \rho_e=\left(c_+-c_-\right)F \tag{3.4}$$

This equation in its integral version describes the total electric field flux through a surface enclosing an excess charge.

The Nernst-Planck equation (Equation 3.5), in its integral form, defines the conservation of the flux, $\vec{\Gamma}_\pm$, of charged particles (of charge $z_\pm e$, where e is an elementary charge) through an arbitrary closed surface, i.e. the conservation of the total electric current, and contains diffusive (diffusion constant $D_\pm$), electrophoretic (proportional to the ion mobility $\mu_{m,\pm}$) and electroosmotic terms (proportional to the velocity of the fluid element $\vec{u}$), and its local form is

$$\nabla\cdot\vec{\Gamma}_\pm=\nabla\cdot\left(-D_\pm\nabla c_\pm+z_\pm\mu_{m,\pm}Fc_\pm\nabla\phi+c_\pm\vec{u}\right)=0 \tag{3.5}$$

Finally, the Stokes equation (Equation 3.6) is the approximation of Navier-Stokes equations with a negligible inertia term,

$$-\nabla p+\eta\nabla^2\vec{u}=-\rho_e\nabla\phi \tag{3.6}$$

and yields the fluid velocities, which depend on the electric potentials, charges, external pressure gradients ∇p and the fluid viscosity η through the assumption of the full hydration of charged particles. Thus, the fluid moves with the charged particles. The conservation of the mass flux, i.e. zero total flux of the fluid exiting any closed surface, compatible with the assumption of the fluid non-compressibility, adds the equation below.

$$\nabla \cdot \vec{u} = 0 \tag{3.7}$$

The coupled Poisson-Nernst-Planck-Stokes (PNPS) equations can be solved under the boundary conditions by using the adaptive numerical method.[20, 23] If the computed solutions, like the electric potential, ionic concentration, velocity, and pressure profiles in the system are known, the ionic current through the channel can be calculated by integrating the ionic fluxes over the cross-section, i.e.,

$$I_{\pm} = \int_S z_{\pm} F \, \vec{\Gamma}_{\pm} dS \tag{3.8}$$

where S is the cross-sectional areal of the channel. The detailed application of these equations and the corresponding quantitative analysis will be discussed in the following chapters.

The theoretical analysis and simulation work in the following chapters are all done by Professor Predrag Krstić's group at Oak Ridge National Laboratory (ORNL).

4. TRANSLOCATION OF SINGLE-STRANDED DNA AND NUCLEOTIDE THROUGH SINGLE-WALLED CARBON NANOTUBES

4.1 Nanopores for Molecular Transport Studies

Nanopores are orifices of molecular diameter that connect two fluid reservoirs.[24] At this length-scale, the passage of even a single molecule generates a detectable change in the flow of ionic current through the pore. Single molecule DNA sequencing is one of the exciting applications proposed for nanopores.[25] The principle underlying nanopore use is straightforward: nanopores can act as Coulter counters. When a single molecule carrying net charges is driven through a molecular size pore by an applied electric potential, it can physically block the pore during the translocation, which produces measurable and distinctive changes in ionic current.

There are two main kinds of nanopores: biological nanopores (e.g., α-hemolysin nanopores) and synthetic nanopores (also known as solid state nanopores). The first nanopore devices were based on pore-proteins, and the translocation of DNA through an α-hemolysin protein nanopore under an external electrical field was demonstrated in 1996.[26] Since then, there has been growing interest in applying nanopores as single-molecule sensors and biophysics tools for studying biomolecules (DNA, RNA, protein, etc).[27-29] The channel (~5 nm long) through α-hemolysin protein

nanopore comprises a transmembrane β-barrel that is ~2.6 nm wide and a 1.4 nm constriction point where the vestibule meets the β-barrel (**Figure 4.1a** left). For this protein nanopore structure, only single-stranded DNA (ssDNA) can pass through it, but double-stranded DNA (dsDNA) cannot.[30] In particular, recent results[31] demonstrated the ability of an aminocyclodextrin-modified α-hemolysin nanopore to distinguish individual mononucleotides (dAMP, dCMP, dGMP, dTMP) from the reduction in the ionic current caused by the translocation of these molecules through the nanopore (**Figure 4.1a** right**)**, suggesting the potential of α-haemolysin as a next-generation DNA sequencing tool.

Recently synthetic nanopores or solid-state nanopores have been fabricated by drilling (and sometimes followed by partially refilling) solid state materials.[32-38] As the versatile alternative to biological nanopores, solid-state nanopores, whose size and shape can be tuned with subnanometer precision, are more robust and durable. **Figure 4.1b** and **Figure 4.1c** show the two typical solid-state nanopres (Al_2O_3 nanopore[37] and graphene nanopore[38]) and the corresponding distribution of the DNA translocation event blockage *vs.* event duration time. One of important purposes to use solid-state nanopore is that it is more friendly and easier to fabricate the nanoscale electrodes around the pore, by which the

electron tunneling method[39] has been proposed for next-generation DNA sequencing. [25, 30]

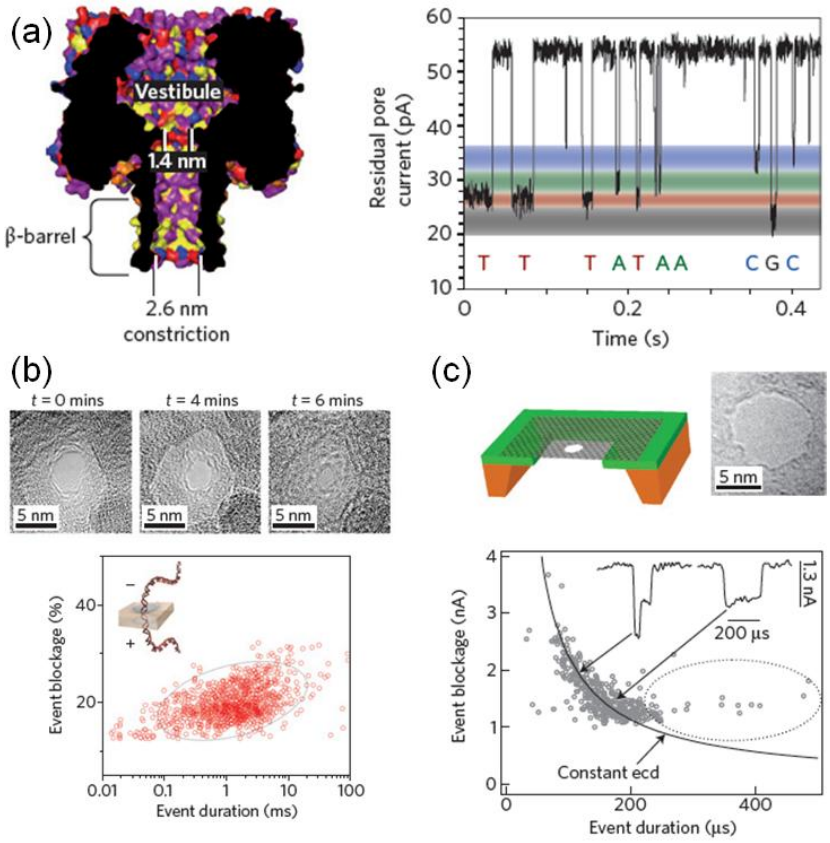

Figure 4.1 Protein nanopores and solid state nanopores for DNA analysis.[30] (a) Left: structural cross-section of α-haemolysin. Right: typical plot of residual ionic current through an aminocyclodextrin-modified α-haemolysin nanopore versus time for individual mononucleotides (dAMP, dCMP, dGMP, dTMP).[29] (b) Top: TEM images showing the formation (by a focused electron beam) and controlled contraction of nanopores in Al_2O_3 membranes. Bottom: scatter plot of event blockage (the percentage of open pore ionic current that is blocked as a molecule passes through the pore) versus event duration for the translocation of segments of dsDNA containing 5,000 base pairs through a 5-nm-diameter Al_2O_3 pore showing a single blockage level (~20% of the open pore current) corresponding to linear, unfolded dsDNA transport. (c) Top: schematic (left) and TEM image (right) of a nanopore in a suspended graphene film containing just one to two layers of carbon atoms. Bottom: scatter plot of event blockage versus event duration showing that folded DNA (left of inset, deep blockade level) and unfolded DNA (right of inset, shallow blockade level) can be distinguished. The solid line represents a constant electronic charge deficit.

4.2 Carbon Nanotube Based Nanopore/ Nanochannel Devices

The carbon nanotube (CNT) recently emerged as a new type of synthetic nanopore. CNT based nanofluidics is a burgeoning field.[14, 40-42] From a biological point of view, the CNT is an ideal model for helping us understand the biological membrane channels that work in aqueous environments with hydrophobic inner walls and nanometer channel sizes. From a fundamental research point of view, it is an exciting system with which to test classical theories of fluid flow at the nanoscale. From an application point of view, CNTs are perfect candidates for providing nanopores or nanochannels in nanofluidic devices. (1) They require no special nanofabrication to achieve a pore size of less than 5 nm. They have an atomically smooth surface and perfect uniformity over large distances. (2) For high quality CNTs, the chemistry and structures of the interior surface are well-defined, which simplifies theoretical simulations. (3) The excellent electrical properties of CNTs provide new routes to electrical detection, trapping and manipulation of charged biomolecules and nanoparticles. (4) Well-defined sites are available for chemical functionalization at the ends of the tubes. Such modifications will be extremely useful for ion and molecule selection, gating or separation.

To utilize the CNT as a nanopore or nanochannel, it is important to first understand the transport of water through the CNT. It seems

counterintuitive that water will enter and transport through hydrophobic and nanometer sized CNTs. However, Hummer *et al.* have used large scale molecular dynamics (MD) simulations to observe the spontaneous wetting and filling of a (6, 6) CNT (0.81 nm in diameter, 1.34 nm in length) with water molecules.[43] The nanoscale confinement and the interactions between water and the CNT surface are found to be critical. The water molecules form ordered structures inside the CNT, which makes confined water within the CNT more stable than bulk water. The lower free energy of confined water drives water molecules into the CNT automatically. Very fast water transport through CNTs was predicted, because of the frictionless motion. Following the pioneering work on water molecule transport, the translocations of more complicated molecules, such as long chain polymer molecules[44], DNA[45] and RNA[46], through CNT were simulated as well. Simulations revealed that DNA molecules enter CNT spontaneously with the aid of van der Waals and hydrophobic interaction forces[47] and the translocation events can be driven by an electric field.[45]

So far, experimental studies using nuclear magnetic resonance (NMR),[48] x-ray diffraction (XRD),[49] IR spectroscopy,[50] transmission electron microscope (TEM)[51] and scanning electron microscope (SEM)[52] have confirmed that water could enter and form ordered structures in SWCNTs or MWCNTs. More direct transport measurements are finished by using a

CNT membrane, which consists of millions of carbon nanotubes in parallel.[42] Hinds' group has pioneered a MWCNT membrane fabrication strategy.[53] They cast a polystyrene polymer layer on a vertically aligned MWCNT forest to fill the gaps between MWCNTs and form an impenetrable membrane. Then both ends of the MWCNTwere opened by oxygen plasma exposure. Holt *et al.* followed the work by replacing the polymer with low stress silicon nitride and using smaller sized DWCNTs.[54] Both groups found that the mobility of gas, water and ions can indeed be greatly enhanced inside the tube. The transport of small redox and fluorescent molecules through CNTs has also been measured.[55, 56] The CNT membrane is relatively easy to fabricate and is perfect for applications such as in molecular separation and sea water desalination.[56, 57]

Inspired by these experiments and theories, we set out to fabricate a nanofluidic device based on a single carbon nanotube. There are several reasons for pursuing nanofluidic devices based on individual CNTs. First, the CNTs are heterogeneous as regards physical properties. The single-CNT approach allows us to carefully study the properties of individual CNT nanopores, facilitating the development of a fundamental understanding of the mechanisms. Second, the single-CNT approach provides great potential for detecting and controlling the translocation of water, ions and

small organic molecules or biomolecules through CNTs. The excellent electrical properties of individual CNTs are readily utilized. Crook's group did some preliminary experiments in the single-CNT direction by fabricating devices containing only one carbon nanofiber (about 150 nm in diameter) in an epoxy membrane.[58] Shashank *et al.* also reported fabrication and fluid flow measurements for devices based on individual carbon nanopipes (about 300 nm in diameter).[59] DNA has been passed through a 100 nm diameter carbon nanotube[60] and 50 nm wide hydrophilic channels.[61] It seems counter-intuitive that hydrophilic DNA would enter the hydrophobic interior of a SWCNT but theoretical simulations show that both RNA[62] and DNA[63] will translocate through 1.5 to 2 nm diameter tubes. The simulations are carried out using very large electric fields (tenths of a volt per nm) to generate observable motion on the simulation timescale. This result leaves open the possibility that some measurable translocation might occur at much the smaller fields that could be implemented in the laboratory.

In this chapter, the translocation of single stranded DNA oligomers and nucleosides (guanosine triphosphates) respectively through the SWCNT, marked by giant current pulses, will be shown.

4.3 CNT Device Fabrication and Instrument Setup

The device fabrication has been described in chapter 3 previously. In brief, well-separated and high quality SWCNTs were grown on a silicon oxide surface by the chemical vapor deposition (CVD) method using ethanol as the carbon source and cobalt nanoparticles as the catalyst.[6] The average outer diameter of the SWCNTs is about 1.7 nm as determined by atomic force microscopy (AFM). After the growth, gold alignment marks (AM) were patterned on the substrate to register the location of the CNTs (inset of **Figure 4.2a**). Then the substrate was coated with an 800 nm thick poly(methyl methacrylate) (PMMA) layer and the reservoir patterns were generated by electron beam lithography (EBL). An optical image of the device is shown in **Figure 4.2a**. The SEM image of the barrier area (**Figure 4.2b**) shows that only one CNT is buried under the 2 μm wide barrier and bridges the two reservoirs.

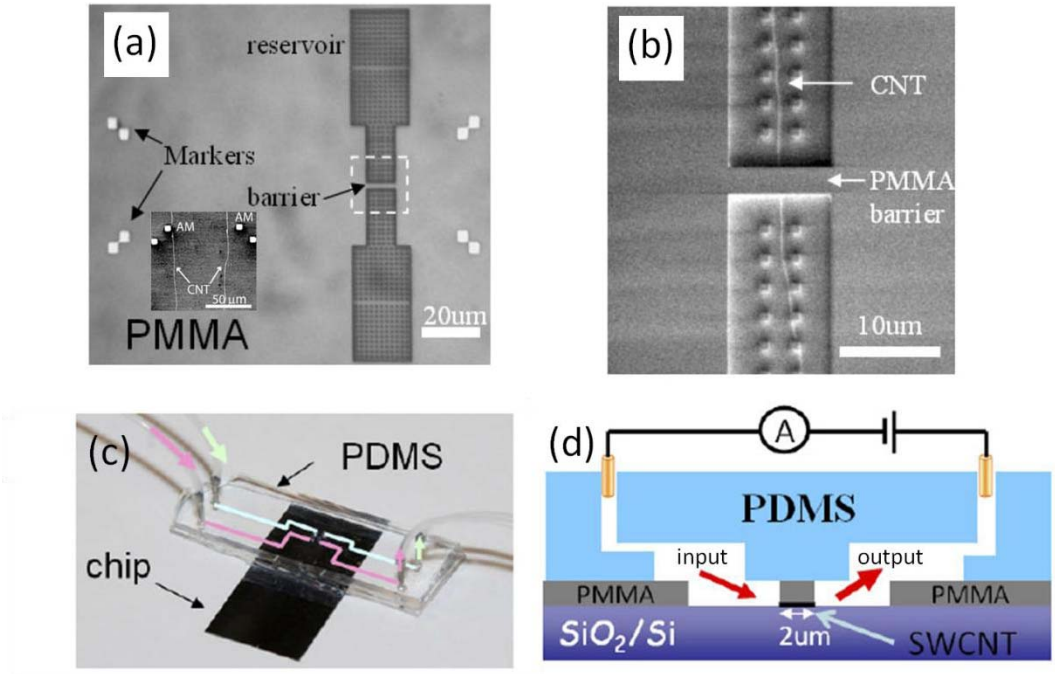

Figure 4.2 A single SWCNT nanopore device.[64] (a) Optical image of a fabricated device after the EBL step. Gold alignment markers and reservoirs are clearly seen. The white dashed square indicates the barrier area. The inset is a SEM image of as-grown SWCNTs relative to alignment markers (AM). (b) SEM of the barrier area (~2 μm in width). One SWCNT passes over the barrier and bridges two reservoirs. The SWCNTs in the reservoirs will disappear after oxygen plasma exposure. (c) Optical image of an assembled device with one pair of silicon tubes for flushing the input channel (green pathway) and a second set for flushing the output channel (pink pathway). (d) Schematics of the cross section of the assembled device and the ionic current measurement setup.

As shown in **Figure 4.2c** and **Figure 4.2d**, a polydimethylsiloxane (PDMS) stamp with embedded microfluidic channels seals the top surface of the device. The fluid reservoirs were filled with buffered KCl solution (1 mM phosphate buffer (PB), pH = 7), and Ag/AgCl electrodes (BASI MF-2078), immersed in the salt soulution, were used to measure the ion conductance across the reservoirs connected by the SWCNT. A voltage is applied

between the two reservoirs and the ionic current is recorded (**Figure 4.2d**) using an Axopatch 200B (Molecular Devices, Inc., CA).

4.4 Ionic Current

The first priority is to guarantee that the ionic current is just through the SWNCT channel, rather than the other leakage paths. Mild oxygen plasma treatment was used to remove the exposed CNT in the reservoirs and open the ends. Each chip also contained a control device lacking the bridging CNT to check the integrity of the barrier, including devices with unopened SWCNTs. The intensity of the oxygen plasma needs to be carefully controlled to avoid damaging the PMMA surface (**Figure 4.3A**). 100% of the devices lacking CNTs did not leak, although the approach resulted in a large fraction of tubes that were not opened (20%), as determined by SEM imaging.

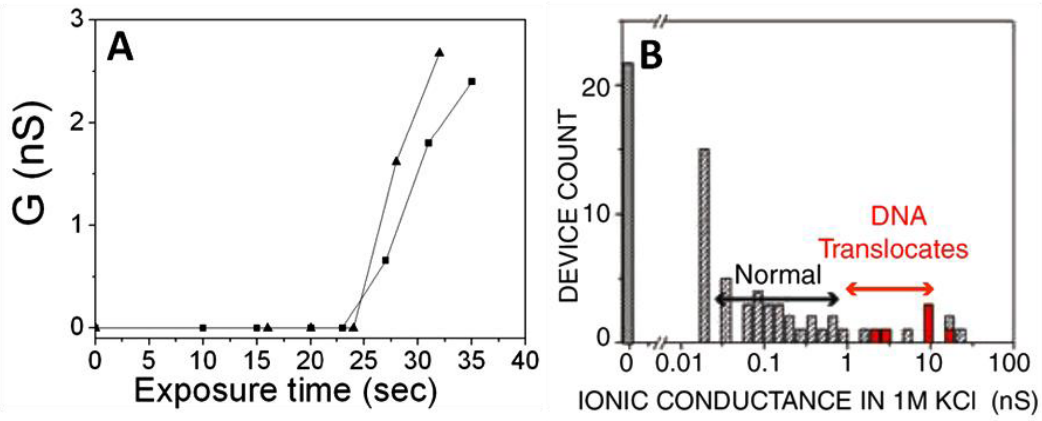

Figure 4.3 (A) Conductance owing to leakage of two control chips (2μm gap) versus oxygen plasma exposure time. The oxygen plasma is 7.2 W at about 550 Torr. (B) Current flows through the single SWCNTs and not

through a leakage path. With the SWCNT bridging the gap and opened, most tubes pass currents in the expected range (Normal), but 20% pass unexpectedly large currents. Some of these (marked in red) also passed DNA oligomers. These data are limited to the subset of devices exposed to short plasma etches for which control experiments show no leakage.[65]

The devices passed current if, and only if, they were spanned by a SWCNT that was opened, so the interface between the tube and the poly(methyl methacrylate) (PMMA) does not appear to provide a leakage path. The ionic conductance of a tube of electrolyte should be given by

$$G = 6.02 \times 10^{26} \left(\mu_K + \mu_{Cl} \right) c_{KCl} e \pi D^2 \Big/ 4L$$

where μ_K =7.62 x 10^{-8} m^2/Vs, μ_{Cl} =7.91 x 10^{-8} m^2/Vs, c_{KCl} is the KCl concentration in mole/l, e the electronic charge, D the tube diameter and L the tube length. **Table 4.1** shows that there is no correlation between the tube diameter and ionic conductance. The ionic conductance spans nearly four orders of magnitude (**Figure 4.3B**), with only the lowest conductances (the range marked “normal” in **Figure 4.3B**) being consistent with the classical formula for c_{KCl} = 1M, 1 nm < D < 5 nm and L = 2 μm. We also measured the electronic properties of some of the tubes (**Table 4.1**) using both their response by Raman scattering and as field-effect transistors (**Figure 4.4a** to **d**). The SWCNTs with the highest ionic conductance are normally all metallic.

FET device ID	Ionic current	Diameter (nm)	Electrical property
HL_4_1_41 AP3	10.7 ± 0.05 nA/0.4 V	2.0	Metallic
HL_4_1_10 AB6	3.4 ± 0.04 nA/0.5 V	1.7 (1.5*)	Metallic†
HL_4_1_39 P6	2.5 ± 0.07 nA/0.4 V‡	4.2	Metallic
HL_4_1_41 AZ3	1.91 ± 0.05 nA/0.4 V	–	Metallic
HL_4_1_41 N2	0.98 ± 0.04 nA/0.4 V (V_T ~ 10 V)	0.9	Semiconducting
HL_4_1_37 AB20	0.46 ± 0.03 nA/0.5 V (V_T ~ 10 V)	1.3*	Semiconducting†
HL_4_1_41 AS3	0.07 ± 0.02 nA/0.4 V (V_T ~ 25 V)	1.8	Semiconducting
HL_4_1_37 Z22	0.10 ± 0.03 nA/0.5 V (V_T ~ 10 V)	1.1*	Semiconducting†
HL_4_1_41 M8	<10 pA/0.4 V(V_T ~ 25V)	3.4	Semiconducting

Table 4.1 Relation of ionic conductance with electrical properties (V_T is the threshold voltage for semiconducting tubes). These measurements do not discriminate between metallic SWCNTs and bundles containing a metallic tube, but most of the tubes are single-walled.[66] Raman scattering was used to determine diameters marked * and confirm electronic properties marked †. The tube marked ‡ translocated DNA.[65]

We also considered whether the excess current could be accounted for by electrochemical currents stemming from reduction and oxidation reactions at the end of metallic tubes. A conducting tube suspended in a potential gradient in an electrolyte acts as a bipolar electrode,[67] but enormous fields are required to drive electrochemical processes at the ends of a bipolar carbon nanotube electrode.[68] Measurements with an electrode contacting the SWCNT directly revealed that electrochemical currents were negligible for the potentials used here (**Figure 4.4e** to **g**).

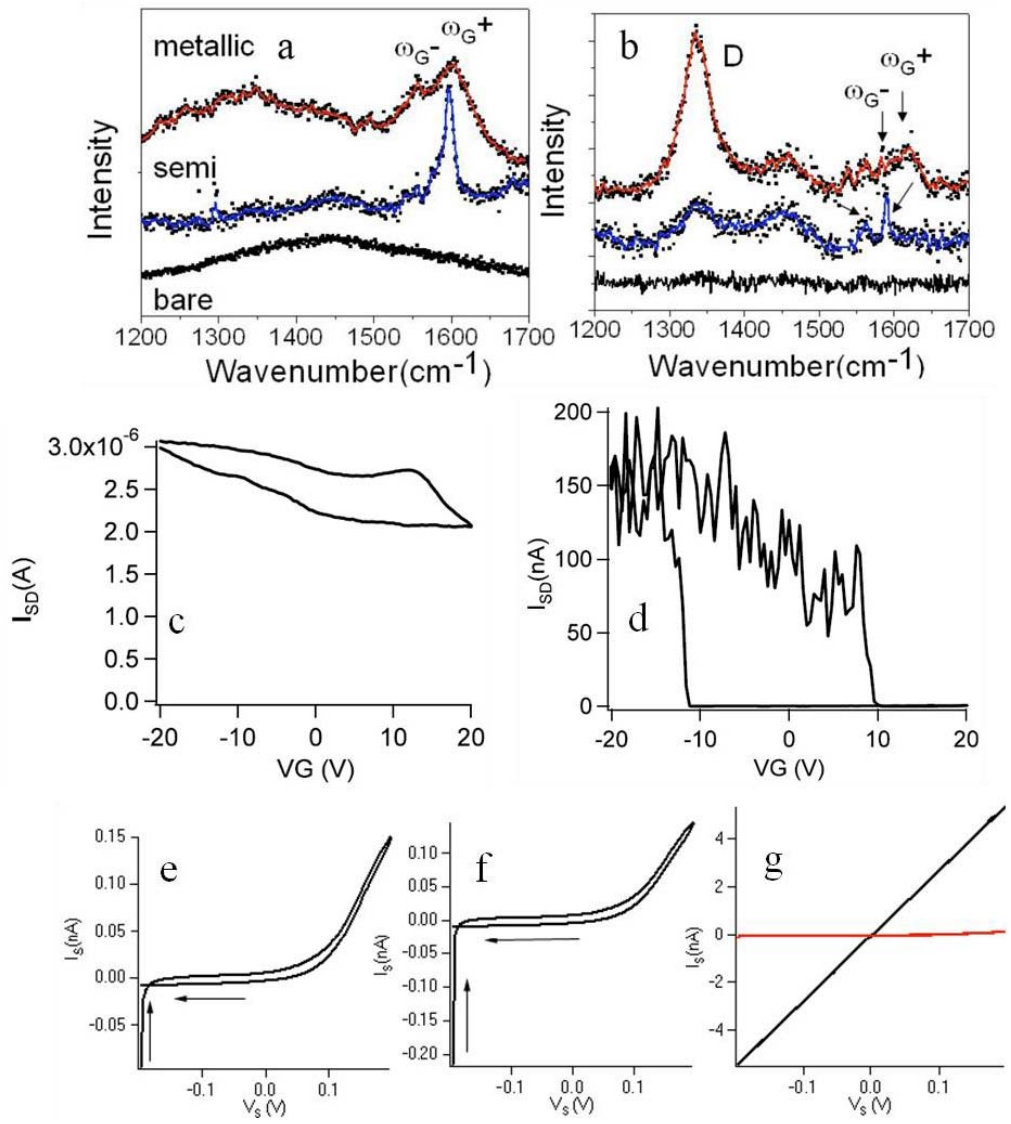

Figure 4.4 CNT properties characterization. Raman spectra of (a) pristine CNTs and (b) CNT after treatment to remove the covering PMMA layer, for both a metallic (red) and a semiconducting (blue) tube. The black dots are raw data and solid lines are obtained after smoothing. Raman septra of SiO_2 substrate alone are shown at the bottom (black). Typical plots of drain current vs. gate bias for a metallic (c) and a semiconducting (d) tube for Vsd= 0.50V. Electronic currents into the tube as a function for a bias V_s between the tube and a AgCl reference electrode in the input reservoir (e) and the output reservoir (f). (g) shows both this current (red curve) and the ionic current through the tube (black curve). For the red curve, V_s is the bias between the AgCl reference electrode in one reservoir and the tube, while for the black curve, V_s is the bias applied between the reference electrodes in the input and output reservoirs.[65]

To look for clues to a mechanism for the large ionic currents, we used molecular dynamics simulations coupled with solutions of the Poisson-Nernst-Planck equation (in Chapter 3) for transport in the SWCNT and the outside reservoirs. The flow rate of water is greatly enhanced inside SWCNTs,[54] but the molecular dynamics simulations showed that the electrophoretic mobility of ions is similar to that in the bulk electrolyte. However, the selective filtering of anions or cations owing to charged end groups[69] can result in a net excess concentration, n, of one charge inside the tube. This charge will, in turn, drive an electroosmotic current. Molecular dynamics simulations further showed that both water and ions flow with an electroosmotic velocity, v, given by $v \propto n^{0.74}$ for a (10,10) SWCNT. Both anions and cations are driven in the same direction by an extremely large electroosmotic flow, but only the charge imbalance inside the tube results in a net ionic current proportional to nv, that is, $\propto n^{1.74}$. The mechanism of charge accumulation which is related with the charges on the end groups will be analyzed in detail in next Chapter.

The current-voltage curves obtained at different salt concentrations in the reservoirs, c, can be fitted if n = 3.31$c^{0.22}$ M (**Figure 4.5A**). This result is equivalent to an ionic conductance that varies as $c^{0.39}$, shown by the red curve passing through the measured data in **Figure 4.5B**. This dependence on concentration is quite different from the linear dependence

expected for a tube of electrolyte or the saturation at low salt observed for a planar nanopore carrying a surface charge.[70]

In contrast to the full set of devices, the subset with anomalously high conductance does show some relation between conductance and tube diameter (**Figure 4.5C**, green squares). The red dashed lines show simulated values of ionic conductance as a function of diameter for n = 2, 3, and 4 M. The measured data can be accounted for by assuming that variability in the charge of end groups leads to some variability in n.

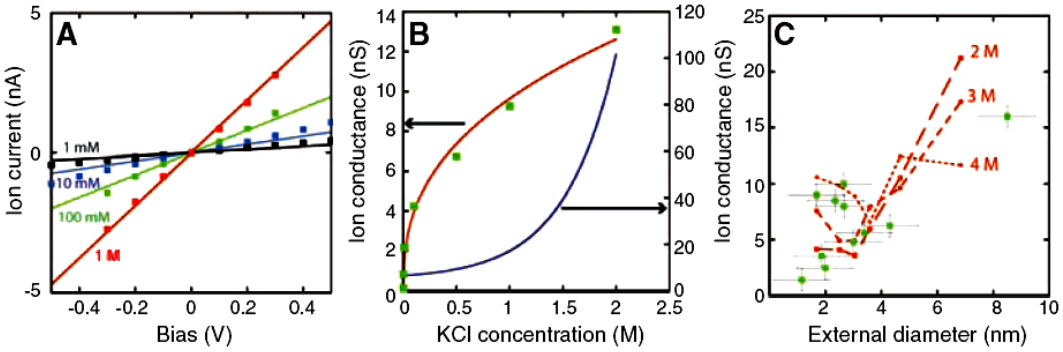

Figure 4.5 Ion transport in the subset of SWCNTS with high ionic conductance. (A) Current versus voltage applied to Ag/AgCl reference electrodes for a 2-μm long, 1.7-nm diameter SWCNT for various concentrations of KCl electrolyte as marked. The solid lines are simulated as described in the text. (B) Ionic conductance as a function of salt concentration. The red line is a fit to the c^m dependence suggested by molecular dynamics simulations. We found 0.33 < m < 0.4 in three different tubes. The blue line shows the salt dependence of conductance measured in a planar nanopore.[70] (C) In this subset of tubes, current at 1 M KCl is better related to diameter (green squares). The red dashed lines show simulations for excess charge densities of 2, 3, and 4 M.[65]

4.5 DNA Translocation

We used 60-nt and 120-nt DNA oligomers with sequences that were predicted to be relatively free of secondary structure to test for DNA translocation of SWCNTs, with forward and reverse primers chosen to have high melting temperatures to minimize primer dimers and false priming. Devices were characterized by measuring current flow with 1 or 2 M KCl alone, and then a DNA solution [1 or 2 M KCl, 1 mM phosphate-buffered saline (PBS), pH 7] was flowed into the input reservoir side, shown in **Figure 4.2d**. A control sample was collected from the output reservoir to check for DNA contamination, and a positive bias was then applied to the output side of the device. In the subset of high current tubes, we first observed a slow increase in the background current (**Figure 4.6A** and **B**; data are for 0.1 nM DNA). After a time, which varied from a few to tens of minutes, depending on the DNA concentration in the input reservoir, large transient increases in current were observed. These "spikes" were accompanied by large fluctuations in the background current (**Figure 4.6C**). The spikes disappeared when the polarity of the bias across the tube was reversed and reappeared when the original bias (positive on the output side) was restored. Quantitative polymerase chain reaction (QPCR), for detecting and counting small numbers of molecules, showed that DNA was translocated in devices manifesting these large spikes, shown as the inset of **Figure 4.6C**. Translocation occurred only in

tubes with conductances (before DNA addition) of >2 nS (**Figure 4.3B**). Some devices that showed instabilities in the background but no large current spikes (**Figure 4.6F**) gave negative PCR results. We also tested for translocation in “failed” control devices (i.e., lacking the CNT and deliberately overetched) that displayed leakage current. A few with very large leakage current showed evidence of DNA in the output well, but none displayed spikes, regardless of the magnitude of the leakage current. Thus, the spikes signal translocation of DNA through the SWCNTs. Although it might be instructive to study the translocation of simpler polyelectrolytes as a prelude to the study of DNA, methods such as dye-labeling are much less sensitive than polymerase chain reaction (PCR) for detecting and counting small numbers of molecules.

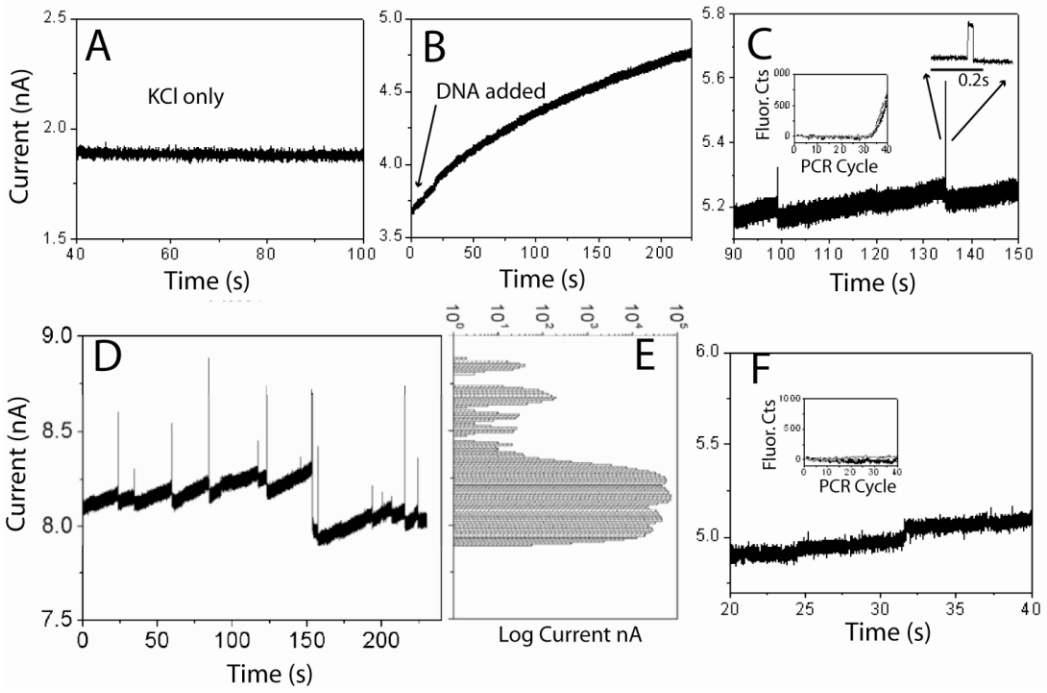

Figure 4.6 Ion current signals of DNA translocation.[65] (A) Current (2 M KCl, 1 mM PBS, pH 7) before DNA addition. (B) After DNA addition, current slowly increases. (C) 5 min after addition of 0.1nM 60-nt DNA, large positive current spikes appear. These spikes are followed by a drop in baseline over a periodof a second or so and then by a gradual rise leading to the next spike. (D) Representative data from another tube (also 60-nt DNA), with the distribution of currents shown in (E). The DNA causes large changes in baseline in addition to the spikes. (F) Data from a tube that showed both a current increase on DNA addition and baseline fluctuations but no spikes. No translocation was detected by PCR. The insets in (C) and (F) show the fluorescence signal from double-stranded DNA dye labels as a function of the PCR cycle number for samples collected from these particular runs.

QPCR also provides a measure of the number of molecules collected. We collected small samples of fluid from the output reservoir by flushing the system through with excess buffer and concentrated the solution using a Microcon YM-10 centrifugal filter so that we could redilute with PCR buffer. We calibrated the PCR reaction with known amounts of DNA and carry out

a PCR analysis of both the target and calibration samples. The final molecule count was corrected for filter losses and dilution during the sample collection. PCR was limited to the first use of a device, and we rejected samples from chips that showed contamination in the control samples collected.

We were able to carry out PCR on samples collected from 12 devices that had a conductance >2 nS. Of these, four had DNA contamination in control samples, leaving the eight devices listed in **Table 4.2**. Two of these showed no spikes and yielded no PCR signal. The remaining six all appeared to pass more than one molecule per spike. In particular, tubes HL-4-1-36 and A136, for which the filter recovery was directly measured with a control sample, passed at least 30 to 40 molecules for each spike. It is possible that the tube fills entirely with DNA, the spike signaling the cooperative emptying (or possibly filling) of the tube.

Tube	Tube conductance nS (1 M KCl)	DNA sample (nt)	Number of spikes	Number of molecules	Molecules per spike
AD1	9.7	60	350 ± 50	8000 ± 2000	23 ± 10
AD2	9.5	60	30 ± 10	400 ± 200	13 (+17, −13)
AA New1	19.6	120	64 ± 10	8500 ± 3100	88 (+126, −88)
AA New2	2.7	120	1500 ± 200	24,400 ± 5700	16 ± 7
HL-4-1-36	9.6	60	36 ± 4	1224 ± 774*	34 ± 21*
A136	1.6	60	46 ± 5	1900 ± 200*	41 ± 10*
HL-4-1-41	4.8	60	0	0	–
HL-4-1-40 O8	2.7	60	0	0	–

Table 4.2 Results of QPCR tests for translocation in tubes with conductance >2 nS that gave uncontaminated control signals (data from four other devices that showed contamination in the control sample were rejected). Errors in spike count reflect the consequences of different cut-off criteria for selecting spikes. Errors in the molecule count were dominated by uncertainties in the filter recovery efficiency, except for the data marked *, which were calibrated with a second oligomer.[65]

Figure 4.7A shows data for the spiking rate as a function of bias for two different tubes passing 60-nt DNA. The spike rate increased with applied bias, and the two tubes showed different threshold biases for the onset of spikes (and hence translocation). For the 60-nt DNA, the spike amplitudes are about 5% of the baseline current (**Figure 4.7B**), and their duration is between 3 and 100 ms, independent of applied bias, as long as it is above the threshold for translocation. The product of the spike duration and amplitude yields the charge contained in each spike (**Figure 4.7C**). This is remarkably large, at about 1 pC or 10^7 electrons in each spike. Fan *et al.* explained positive charge spikes observed in nanochannels as a consequence of additional mobile ions brought into the channel by DNA molecules.[71] Filling the tubes (2 μm long) with 100 (20 nm long) 60-nt DNA

oligomers, each carrying 60 excess electronic charges would account for only 1 part in 10,000 of the observed charge in each spike. The spikes must originate with large changes in the polarization outside the tubes, much as observed in junctions between micro- and nanochannels.[72] Recent modeling (P. Krstić *et al.*, unpublished) shows that the large current increase may be due to a large electroosmotic current accompanied by charge filtering by the DNA (which only passes cations when it is stuck inside the CNT according to molecular dynamics (MD) simulations).

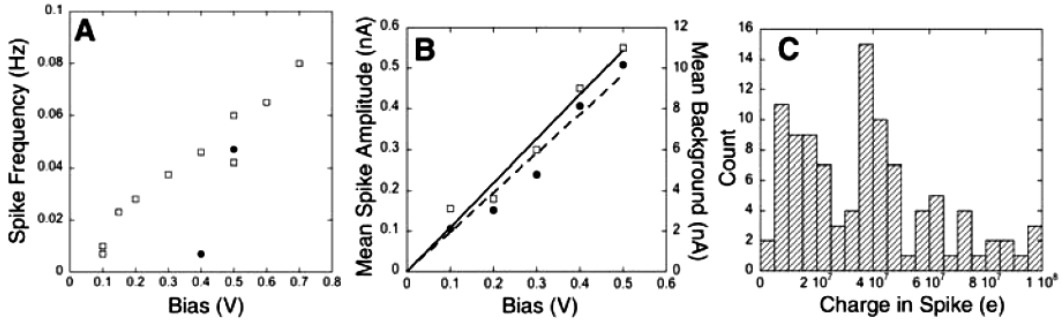

Figure 4.7 Characteristics of the translocation signals for 60-nt DNA.[65] (A) Spike rate increases with bias after a threshold that depends on the particular CNT; the two devices here show spike signals above 0.1 (squares) and 0.4 V (circles). (B) Spike amplitude (squares) increases linearly with bias and is about 5% of the background current (circles). (C) Distribution of the charge in each spike for the SWCNT in units of the electronic charge, e.

The excess ionic conductance appears to be a characteristic of metallic tubes, and we have proposed a mechanism based on electroosmotic flow resulting from trapped charge. Tubes with high ionic conductance will

transport DNA molecules, giving a distinctive and unexpectedly large electrical signal of translocation. This kind of nanopore combines a long channel (in which translocation speed might be slowed) with an "integrated" electrode that might prove useful in new schemes for sequencing DNA by tunneling.[25] The ability to select metallic SWCNTs of a desired diameter[73] may open the way for production of devices with particular pore sizes.

4.6 GTP Translocation

Short ssDNA oligomers were chosen for the CNT translocation experiments. Quantitative PCR (Q-PCR) was used to verify DNA translocation. PCR is a fascinating molecular biology technique that a few or even single copies of DNA can be quickly and exponentially amplified to millions of copies. Therefore PCR is an ideal tool to detect trace amount of DNA with known sequence. However, the minimum length of DNA that can be amplified is about 20 nt. We have measured the translocation of 60nt, 120nt and 180nt long oligomers. In all the experiments, large transient increases ("spikes") in ionic current were observed. Those spikes signal the molecular translocation events, as confirmed by Q-PCR for the 60 and 120 nt oligomers. In general, the shorter oligomers show shorter spike width, but these widths are large compared to the translocation times observed with conventional nanopores.[74] This raises the question of

whether a single nucleoside, like guanosine triphosphate (GTP), can generate a measureable signal.

To test for this possibility, we used a guanosine 5'-triphosphate or GTP (Sigma Aldrich, HPLC grade) molecule. The device has a SWCNT bridging 2 μm barrier. Two control devices were fabricated on the same chip to test the leakage current. Before the introduction of 5 μM GTP into the input reservoir, the ionic current of the device at 1M buffered KCl (1mM PBS buffer, pH=7) solution was measured by applying a 700 mV bias at the output reservoir (input reservoir is grounded) for several minutes. An example of the ionic current time trace is shown in **Figure 4.8a**. The ionic current was about 1.2 nS. No spikes or other fluctuations were observed in the ionic current. After the introduction a solution of 5 μM GTP in 1M buffered KCl solution, the ionic current gradually increased to 2.9 nS and large transient increases in ionic current were observed at 700 mV. These "spikes" were accompanied by fluctuations in the background current (**Figure 4.8b** and **c**). No spikes were observed, at smaller or negative biases. These spikes must be induced by GTP and are most likely due to the translocation of GTP molecules, although this cannot be tested by PCR. The average spike duration is about 0.86 ± 0.15 ms (**Figure 4.8d**).

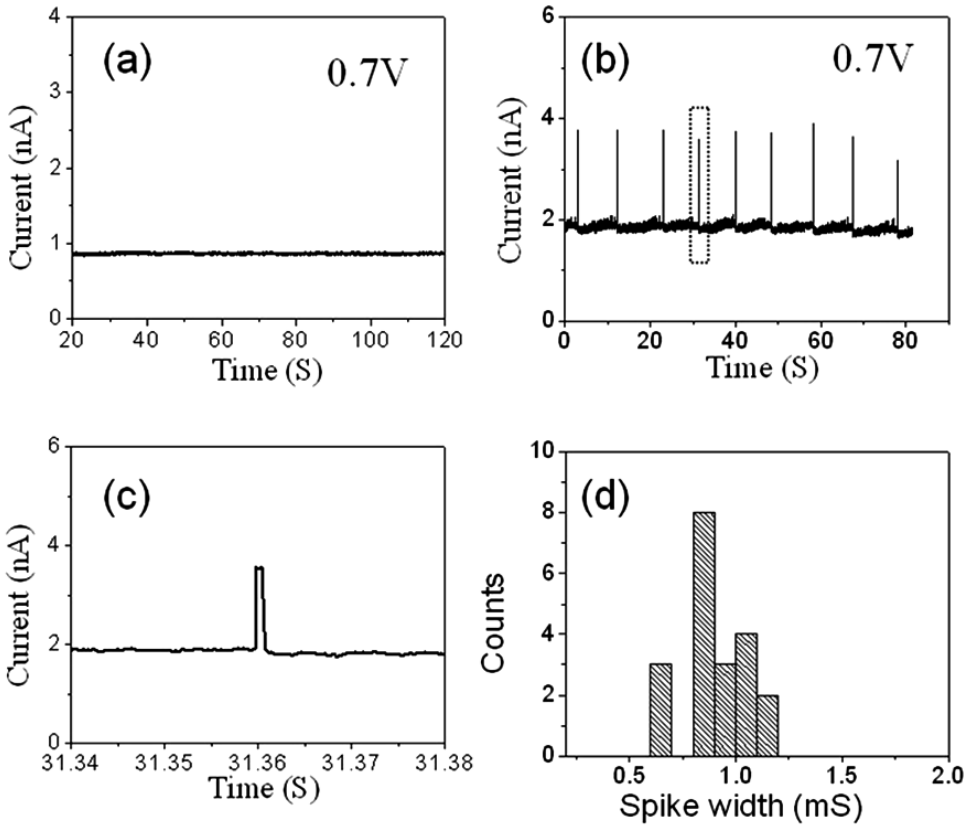

Figure 4.8 (a) An example of ionic current versus time at an applied voltage of 700 mV in 1M buffered KCl solution (1mM PBS, pH 7). (b) Upward spikes appear in the ionic current versus time at an applied voltage of 700 mV after the addition of 5μM guanosine triphosphate (GTP) GTP (1M KCl, 1mM PBS, pH 7) into the input reservoir. (c) A zoom-in of one typical current spike in (b) (inside the dot lines). (d) The histogram of the spike width. The average duration of the spike is 0.86 ± 0.15 ms.[64]

Figure 4.9 shows a plot of the log of the average pulse width for 120 and 60 nt DNA (both at 500 mV). The pulse widths are widely distributed, but plotted together with the datum for GTP (at 700 mV), they suggest a non-linear, power-law relationship (~$0.08N^{1.2}$) between the number of nucleotides and translocation time. For the purposes of this plot, GTP has been shown as N=1. If the backbone charge is the important physical

parameter, then the GTP data point should be moved to N=3. The errors in the data are such that this would not alter the important implication of a power-law relationship between pulse width and polymer length. Certainly, this relation needs to be further verified on much longer ssDNA.

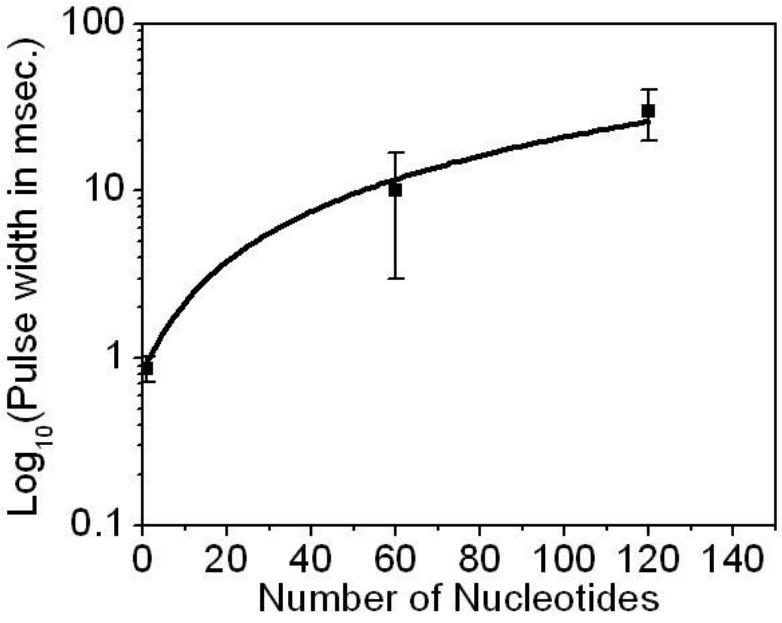

Figure 4.9 Semi-log plot of the average pulse width versus the number of nucleotide in the ssDNA oligomers. The solid line is a non-linear, power-law fitting (~$0.08N^{1.2}$) to the experimental data. The bias is 500 mV for oligomers and 700 mV for GTP.[64]

4.7 Accumulation Times for DNA Translocation

Here we turn to investigate in more detail the timescale associated with DNA accumulation at the input to the SWCNT. The reference electrode in the DNA input reservoir is grounded as shown in **Figure 4.10a.** 0.1 nM 60

nt ssDNA is injected into the input reservoir. Both reservoirs contain 1M KCl solution with 1mM PBS buffer (pH 7). Translocation requires that the output reservoir is biased positive with respect to the input reservoir. After the onset of tranlocation signals, we investigated the effects of reversing the polarity applied to the device.

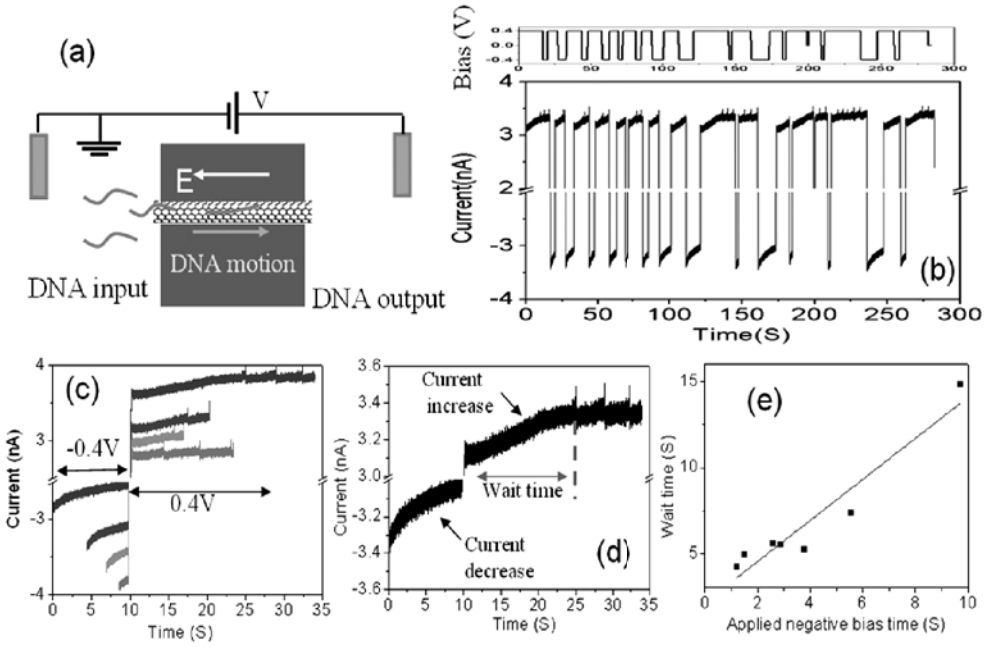

Figure 4.10 (a) The schematic of a DNA translocation measurement setup. The electrode at input reservoir is always grounded. 0.1nM 60 nt ssDNA is injected in the input reservoir. (b) The time trace of ionic current when switching the polarity of bias at output reservoir. (c) Re-organized ionic current data by aligning ionic current at voltage transition position. (d) The zoom-in of one typical data. The current magnitude always increases at positive bias and decreases at negative bias. Spikes appear after a wait time at positive bias and no spikes at negative bias. (e) The relationship between the wait time and the applied negative bias time. The solid line is a linear fit to the experimental data.[64]

We switched the bias between -0.4 V and 0.4 V back and forth frequently and recorded the ionic current through the device. A typical time trace of

the current is shown in the lower panel of **Figure 4.10b**. The applied voltage versus time is shown in the upper panel of **Figure 4.10b**. The ionic current data in **Figure 4.10b** can be reorganized by aligning ionic current at the negative to positive voltage transition position. The re-plotted data is shown in **Figure 4.10c** – lines to the left of 10s (arbitrarily set to the transition time) represent current versus time as the output reservoir was at -0.4V (time stopping at 10s), while those to the right represent current versus time as the output reservoir sat at +0.4V (time starting at 10s). Note that translocation spikes are only observed when the output reservoir is positive, the same situation as in the DNA translocation experiment (section 4.5).

One recording through a bias reversal is expanded in **Figure 4.10d** to show the wait time for the onset of translocation spikes more clearly. The wait time is plotted versus the period for which bias was reversed in **Figure 4.10e**. Clearly, DNA is swept away from the entrance to the device when the input reservoir is biased positive. The recovery time for the onset of signals is very close (slope = 1.2) to the time for which the bias was reversed. This suggests that the wait time reflects the time needed to acquire an adequate concentration of DNA on the input side of the tube. Such a pre-concentration process has been demonstrated in other microfluidc to nanofluidic interfaces.[72, 75] So the existence of a wait time

may suggest that the DNA translocation can only start when the local DNA concentration at the entrance achieves a critical level. This might imply a collective DNA translocation (i.e. more than one molecule translocating at a time), consistent with the measured relationship between the number of translocation spikes and amount of DNA translocated.

4.8 Conclusion

In this chapter, the development of nanopore application on DNA transport analysis is introduced. Then, the SWCNT nanopore device is illustrated, in which SWCNT spans a barrier between two fluid reservoirs, enabling direct measurement of ion transport through the tube. A fraction of the tubes pass anomalously high ionic currents. Electrophoretic transport of small single-stranded DNA oligomers through these tubes is marked by large transient increases in ion current and was confirmed by quantitative polymerase chain reaction (QPCR) analysis. Each current pulse contains about 10^7 charges, an enormous amplification of the translocated charge. In addition, the translocation of GTP through SWCNT was also carried out and the data for the translocation times is suggestive of a power-law relationship between translocation time and polymer length. If this turns out to be a generally valid result, it is important because it predicts a very slow translocation speed of very long DNA through devices. More data is needed on the relationship between translocation time, applied bias,

polymer length, tube diameter and tube length. The correct choice of tube dimensions might permit translocation of long DNA while also slowing it to a speed that matches sequence readout speed. This is a critical missing component of current nanopore devices where translocation is generally much too rapid.[25] Our study of the wait times points to the pre-concentration of DNA at the entrance to the device. This is clearly important because it suggests that very small amounts of DNA could be handled simply by increasing the wait time for translocation.

Individual SWCNT based nanofluidic devices, which simplify the construction of nanopores, may open new avenues for fundamental research, such as molecular confinement and mass transport at nanoscale, and practical applications, such as new schemes for DNA sequencing and new type of single molecule sensor. To achieve these goals, significant efforts in experiment and theory are still needed.

5. ORIGIN OF GIANT IONIC CURRENTS IN CARBON NANOTUBE CHANNELS

5.1 Background of Nanofluidic Devices and Research

New phenomena arise as fluid flows in channels that are small on the scale of a Debye length. Molecules and ions are transported selectively both as a consequence of the finite channel size and because of chemical and electrostatic interactions with the walls of the device.[14, 21, 74, 76] Devices have been fabricated by cutting nanochannels into silica[77, 78] and drilling nanopores into solid membranes.[24, 74, 79] Flow of aqueous electrolytes inside carbon nanotubes is particularly interesting because of the prediction that it should be nearly frictionless,[80-82] a prediction born out by measurement of flow in well characterized membranes spanned by millions of carbon nanotubes.[54, 83] This thesis describes the new devices we have built in which just one single walled carbon nanotube (SWCNT) connects two fluid reservoirs.[65] This device allowed measurement of the voltage-driven flow of electrolyte and molecules through individual tubes of a few microns in length. Ion currents through the SWCNTs were approximately two orders of magnitude larger than predicted using the classical formula for the resistance of a tube of fluid and the known resistivity of the electrolyte. Furthermore, these ion currents have a power-law dependence on electrolyte concentration (in the range of 1mM-1M) that is quite different from the concentration dependence observed in any

other form of nanochannels. This behavior is probably limited to SWCNTs of nm-diameter and micron lengths, because current transport through much longer tubes (0.5 mm length) is dominated by protons.[84]

Electrophoretic ion mobilities are not enhanced inside SWCNTs,[65] so electrophoretic flow cannot account for the large currents that were observed. If electrolyte in the SWCNT carries an excess charge of one sign, this can be transported selectively, resulting in nearly frictionless flow of water which drives very large electroosmotic currents. In this chapter, I will show how we tested these ideas using an ionic field effect transistor (ionic FET)[16, 17, 85-87] in which an insulated gate controls the potential and charge of the SWCNT while the flow of ionic current between fluid reservoirs is measured. The experiment results match well with the solutions of the coupled Poisson, Nernst-Plank and Stokes (PNPS) equations, carried out at Oak Ridge National Laboratory (ORNL). This confirms that the giant currents are a consequence of electroosmotic flow.

5.2 CNT Device Fabrication

The construction of the ionic FET is shown in **Figure 5.1**. Long SWCNTs were grown from Co or Fe catalyst particles on an oxidized silicon substrate as described in Chapter 2. Index markers (**Figure 5.1a**) were fabricated to align subsequent lithographic steps with the axis of the

SWCNTs. A 20-30nm thick SiO_2 layer is deposited on top of the SWCNTs as a dielectric for supporting the gold gate electrode. An optical image of the final device (taken through the PDMS microfluidic cover) is shown in **Figure 5.1b**. **Figure 5.1c** shows the overall device arrangement with the Ag/AgCl reference electrodes used as the source and drain electrodes in the fluid reservoirs. The length of the SWCNT connecting the reservoirs is typically 20 μm. **Figure 5.1d** shows a cross-section through the barrier. In addition, a number of such ionic FET devices were made with an electronic FET fabricated at one end of the same SWCNT simultaneously (**Figure 5.1e**), in order to obtain the electrical properties of the SWCNT. Thus, assuming that the tubes do not change their chirality over their length, we can use measurements of the electronic properties of the SWCNTs to determine whether a given ionic FET was made from a metallic or semiconducting tube.[88]

A critical step lies in opening SWCNTs using an oxygen plasma etch without damaging the insulating bridge that separates the fluid reservoirs. The use of a 20-30 μm wide barrier (comparing with 2μm wide barrier used earlier) has now pushed the yield of working devices to about 40%. The ionic conductance distribution of all the working devices at 1mM KCl solution with floating gate is shown in **Figure 5.1f**. These devices display higher conductances than the devices we built with PMMA barriers on the

SWCNTs.[65] This may be due to the new device geometry and/or the differences of the charge density in the barrier region.

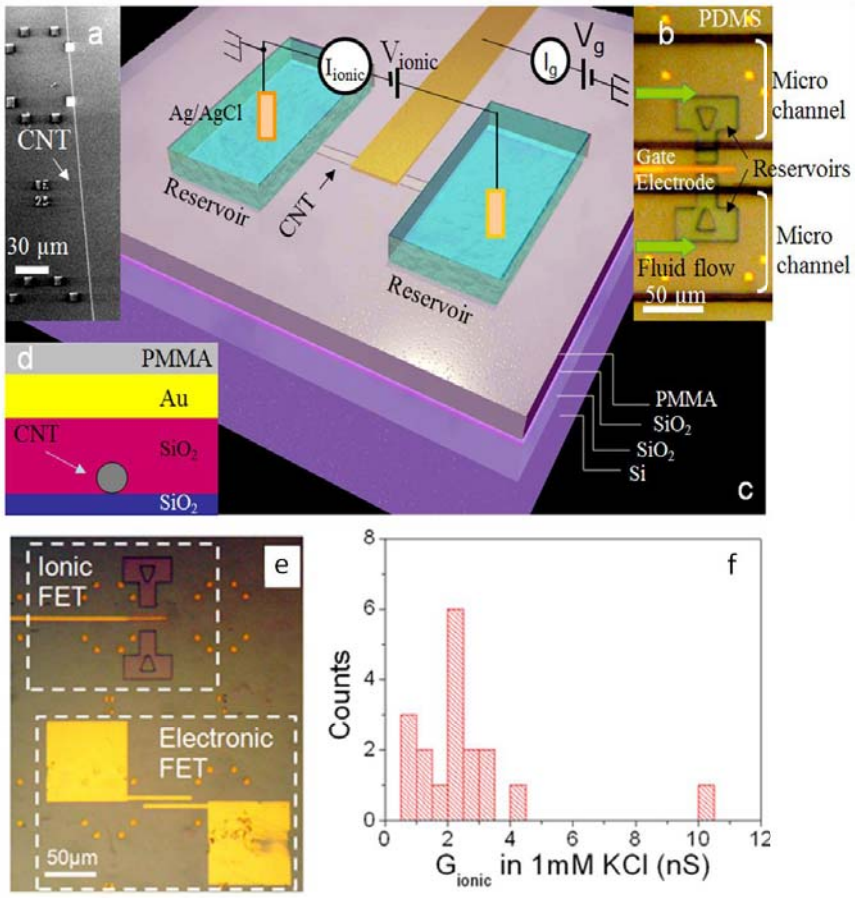

Figure 5.1 Device fabrication and measurement setup.[89] (a) Scanning electron microscope image of a SWCNT on silicon oxide surface with gold alignment markers. The CNT is typically 1.7 nm in average outer diameter. (b) Optical microscope image of a device looking down into the PDMS microfluidic system that covers it. The scale bar is 50 μm. (c) Schematic of the device and the electrical connections. A 10-30μm long CNT connects two reservoirs with a 20-30 nm thick silicon oxide layer used as dielectric between the top gate (voltage V_g) and the CNT. A voltage (V_{ionic}) is applied across the two reservoirs using Ag/AgCl electrodes. Ionic current through the tube (I_{ionic}) and the gate charging current (I_g) are recorded. (d) Schematic cross-section through the barrier region. (e) Optical microscope image of a device showing both ionic CNT FET and electronic CNT FET. Both FETs were fabricated on the same CNT, guided by the metal markers. The electronic FET is gated using the Si substrate as a backgate. (f) Conductance distribution of all the working devices.

5.3 Ionic Conductance and Ionic-FET based on CNT Nanofluidic Devices

With several hundred working devices, the simplest check on device quality is to measure the ionic current as a function of salt concentration (**Figure 5.2a**). A particular form of power law dependence of conductance, G, on salt concentration, c, $G \sim c^b$ (where $c > 0.1$mM, $b < 1$) is unique to transport through SWCNTs. Other types of nanochannels (e.g.,silicon based) often have an approximately constant conductance at low salt and the conductance become proportional to concentration at high salt (> 0.1M), giving rise to an opposite sign of curvature in the plots of conductance versus salt concentration.[65, 90] In our experiment, b is sensitive to barrier materials and CNT electrical properties. A small range of b values (~0.3-0.4) is found for devices with PMMA barriers. The range is much bigger with SiO_2 barriers. Nonetheless, this form of power law is found only for ion transport through small diameter SWCNTs. It is a consequence of electroosmtic flow in a very small channel, which will be shown below. For the particular device used to generate the data shown in **Figure 5.2b**, b = 0.37 for the case of a grounded gate, and 0.44 for the floating gate, values fall well within the range measured for tubes without a gate.[65] Since grounding the gate changes the electrical properties of the system, it implies that the floating gate carries a charge. The change of slope of this plot (**Figure 5.2a**) on grounding the gate electrode also

indicates that the exponent, *b*, is probably affected by the total charge on SWCNT. Also, this charge, Q, is a critical factor in determining the electroosmotic flow through the tube, and it can be found by fitting these conductance curves using solutions of the PNPS equations with different charges, as discussed in details in the Quantitative Analysis part (section 5.4) of this chapter. An example of such a fit is shown by the red hollow squares in **Figure 5.2a**.

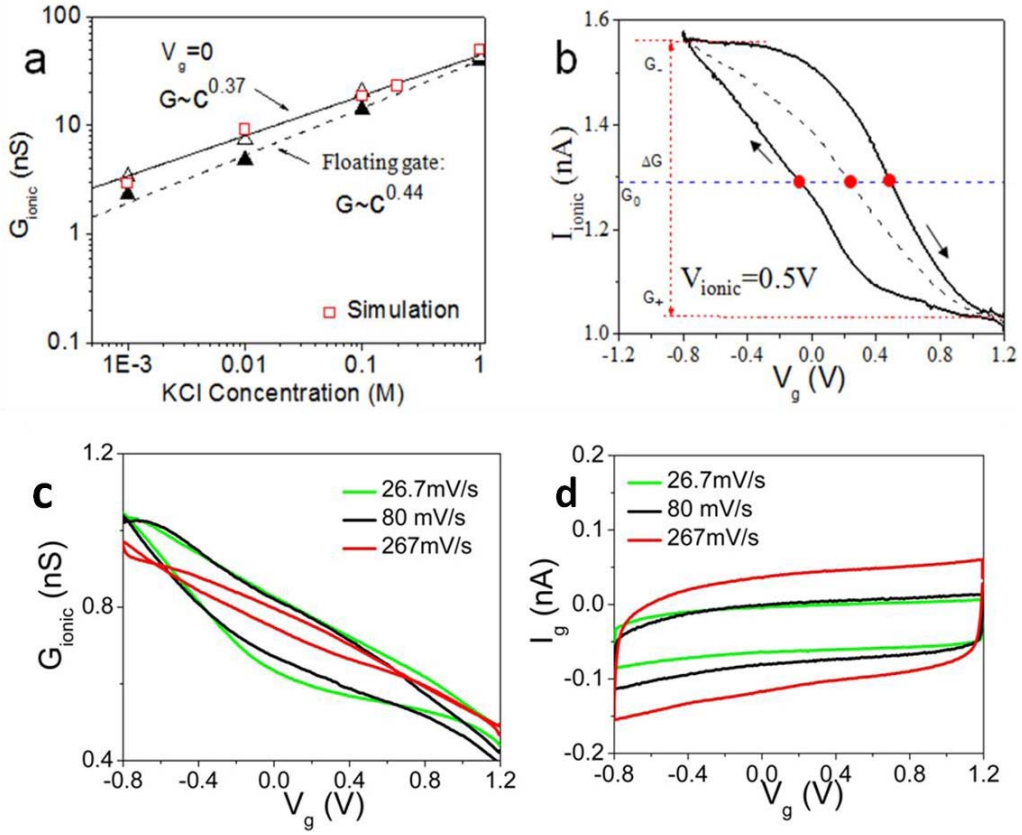

Figure 5.2 SWCNT ionic-FET characteristics.[89] (a) Concentration dependence of ionic conductance on salt concentration. Filled triangles are for a floating semiconducting tube, opened triangles are for a tube with the gate held at zero volts and the lines are fits to $G_{ionic} \approx c^b$. The red squares are simulations in which the charge on the tube was adjusted to fit these data. (b) Ionic current vs. V_g at V_{ionic}= 0.5V for a semiconducting SWCNT with a V_g sweep rate of 80mV/s. The sweep direction is indicated

by arrows. The black dashed line is the average of the sweep-up and sweep-down currents. The horizontal blue dashed line is the ionic current recorded when the gate is floating. The solid red circles label the points where the current through the gated device equals the current recorded with a floating gate. The definitions of the quantities G_+, G_-, ΔG ($=G_- - G_+$) are illustrated by the red dashed lines. (c) G_{ionic} vs. V_g curves of one device at different sweep rates. The salt concentration is 1mM. (d) The I_g vs. V_g curves at different sweep rates measured at the same time.

Figure 5.2b shows the typical ionic FET data and the dependence of the ionic current flowing between the Ag/AgCl source and drain electrodes on the bias applied to the gate electrode embedded in the barrier region. The response shows a significant hysteresis characteristic of the extrinsic charges that dominate SWCNT devices, but the ionic current is always reduced when the gate is swept to a positive bias. The hysteresis of G_{ionic} vs. V_g curves decreases with increasing sweep rate, shown in **Figure 5.2c**, indicative of a slow polarization process in the gate region. A sweep rate of 60-80 mV/s for all measurements was used. The corresponding I_g vs. V_g curves are shown in **Figure 5.2d**. The hysteresis increased with sweep rate, suggesting a capacitive current origin of I_g. The reduction of ionic current on positive gating implies that the current is carried predominantly by cations. The dashed line shows the average of the sweep-up and sweep-down curves, and this average is always displaced to the right of $V_g=0$. That is to say, zero conductance occurs at a positive gate bias. The presence of a charge on the device was indicated by the change of the salt concentration dependence on grounding the gate (**Figure 5.2a**). The

measured FET characteristic implies that this charge on the tube (and its immediate environment) is negative. This charge is most likely largely extrinsic, associated with the SiO_2/CNT interface, charge inside the barrier material close to the CNT and at the ends of the tubes, both on the barrier material and in the form of charged carboxylates on the ends of the SWCNTs. In the modeling, we simplify what is possibly a complicated and extrinsic charge distribution on SWCNT by assigning a fixed total charge Q to the surface of the SWCNT. This is to be distinguished from the surface charge density σ_s, the two being connected by $Q = \int_S \sigma_s dS$. We allow the simulations to self-consistently adjust the surface distribution of charge on the tube as the gate bias and other parameters of the system are changed.

The measured ion current as a function of both drain-source bias (vertical axis, V_{ionic}) and gate bias (horizontal axis, V_g) is shown in **Figure 5.3a**, where the magnitude of the ion current is shown by the color scale (blue is negative, red is positive - the raw data are shown in **Figure 5.3b** and **c**). These data show "p-type FET" characteristics over a wide range of drain-source bias. The ion current is only partially gated, as is characteristic of ionic FETs,[16, 17, 85] the ionic conductance falling to a lower limit, G_+, at the highest positive gate bias (G_+ is shown for a single value of V_{ionic} in **Figure 5.2b**). The fraction of conductance that can be switched is characterized

by the "gating efficiency" $\Delta G/G_+$ (where $\Delta G = G_- - G_+$, see **Figure 5.2b**). A distribution of this parameter for 24 devices is shown in **Figure 5.3d**. Gating increases the ionic current many times in some devices (up to 5x) while other devices were barely gated.

One possible source of this variability of gating efficiency lies with the carbon nanotubes themselves. Metallic tubes might be expected to screen the gate field more effectively than semiconducting tubes,[91] leading to a lower gating efficiency for devices made from metallic tubes. An outlined data set is shown in **Figure 5.3d**, with the tubes identified as metallic by red and the ones identified as semiconducting by blue. Clearly, gating is more effective in semiconducting tubes, as expected (the outlying point might be a consequence of a tube that changed chirality between the electronic FET and the ionic FET portions of the device). There is considerable spread in the characteristics of the semiconducting tubes, suggesting that external factors (such as variation in external surface charges) also contribute to the range of characteristics.

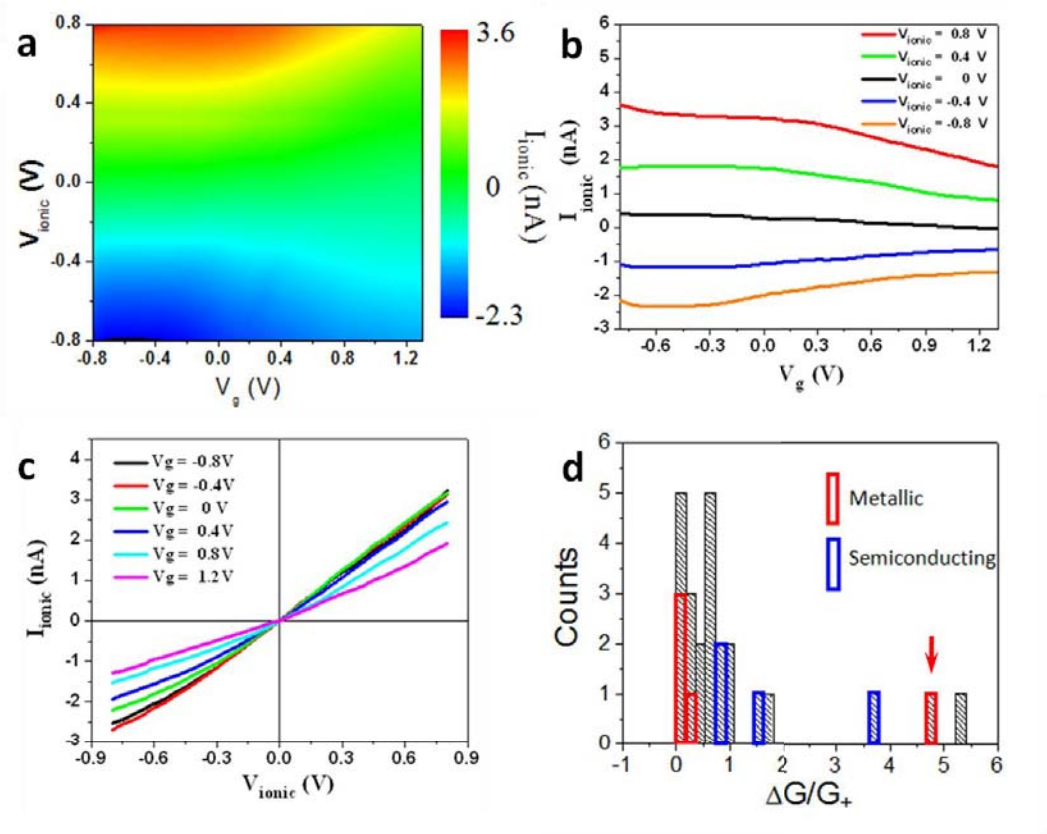

Figure 5.3 SWCNT ionic-FET characteristics.[89] (a) Heat map of the ionic current vs. V_{ionic} and V_g based on sweep-down curves. P-type transistor action is clearly displayed. (b) The I_{ionic} vs. V_g curves at different V_{ionic}. (c) The I_{ionic} vs. V_{ionic} at different V_g. (d) Histogram of the gating efficiency, $\Delta G/G_+$, for all the measured devices for 1mM KCl solutions (pH=7). The gating voltage range is -0.5V to 0.8V on average. Bins outlined in red and blue indicate metallic and semiconducting CNT devices as measured independently using an electronic FET fabricated on the same tube. The datum pointed to by an arrow is an outlier that might be a consequence of a change in chirality of the SWCNT between the ionic and electronic FET devices.

Table 5.1 lists the ionic gating efficiency of all the working devices, measured at a V_g sweep rate of 60-80mV/s in 1mM buffered KCl solution, pH=7.4. In order to reveal the relationship between the electrical properties of the CNT and the gating efficiency, we measured the

electrical transport properties of several devices, as color coded in the table. The results of three devices, representing semiconducting, metallic and small band gap semiconducting CNT devices, are shown in **Figure 5.4**. The ambipolar behavior in the electronic transport characteristic suggests a small band gap SWCNT (outside diameters are estimated to be 3-5nm).[9] The ionic gating efficiency of this device is about 0.1.

Device Name	Gating efficiency ($\Delta G/G_+$)	Device Name	Gating efficiency ($\Delta G/G_+$)	Device Name	Gating efficiency ($\Delta G/G_+$)
S032L5L6	0.23	S058R8	1.01	SN00116R12	0.25
S028L9	0.58	S065L13	0.65	SN009R4	0.55
S028L5L6	0.46	S065L14	1.46	PF01L11*	0.007
S054R11	0.68	S110L7	0.47	PF01L14*	0.151
S054R9R12	0.95	S110L1	5.24	HF5L7*	0.10
S054L8L11	0.88	SN009R12	0.7	PF03L11*	1.62
S058R11	0.22	S204L13	0.83	PF03R2*	3.76
				PF03L4*	4.85

Note: 1. Red = metallic CNTs, blue = semiconducting CNTs, orange = small gap semiconducting CNT.
2. * CNTs grown using the ferritin method.

Table 5.1 Gating efficiency of all the measured devices in 1mM buffered KCl ,pH=7.[89]

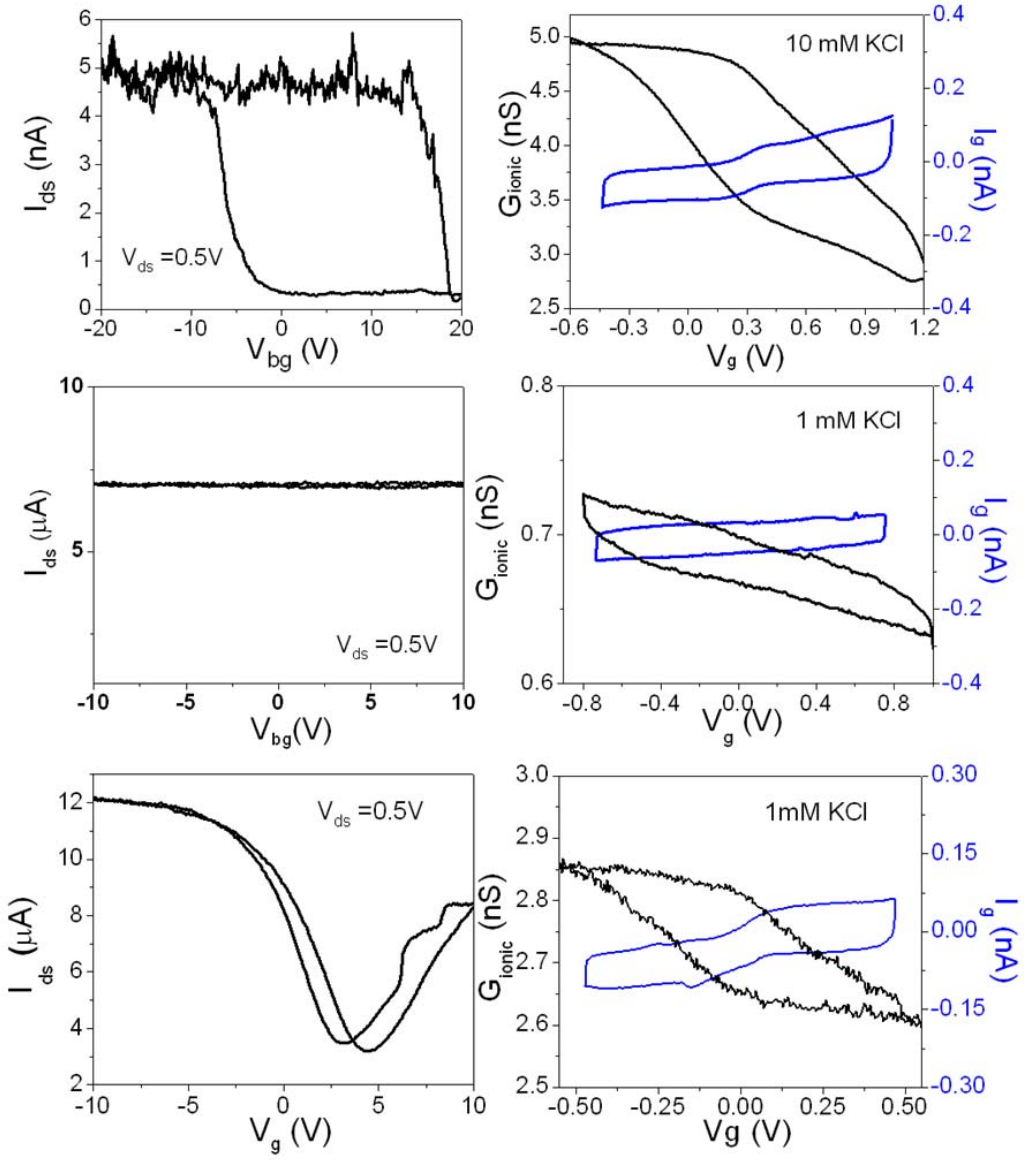

Figure 5.4 The electrical transport characteristics (left column) and ionic transport characteristics (right column) of device SN009R12 (upper row), PF01L14 (middle row), and HF5L7 (lower row). The CNT in Device HF5L7 was grown by ferritin method. The CNT length is about 20 μm.[89]

In addition, the ionic conductance using an electrolyte with a large cation, $Ru(bipy)_3Cl_2$ was also analyzed. As shown in **Figure 5.5**, the measured ionic conductance using $Ru(bipy)_3Cl_2$ through the device is about 10 times

smaller (at Vg=0) than when using the same concentration of a KCl solution. A reduced $Ru(bipy)_3Cl_2$ flux (30% of the KCl) was also observed in MWCNT membranes (~7nm inner diameter).[92] However, the measured conductance of $Ru(bipy)_3Cl_2$ is still much bigger (~3-4 orders of magnitude higher) than the calculated results based on a model of pure electrophoresis. In addition, the ionic current of $Ru(bipy)_3Cl_2$ through a non-damaged SWCNT device is gatable, as shown in **Figure 5.5d**. Interestingly, we obtained n type ionic transistor behavior (the transistor changed to p type when switching to KCl electrolyte). This suggests that the movement of bigger $Ru(bipy)_3^{2+}$ cation was hindered even at negative gate voltage. The anion Cl^- became the major carrier at positive gate voltage (the positive gate voltage will attract the Cl^- to get into the CNT, overcoming the repulsion from the negative charged carboxyl groups at CNT ends).

The bulk diffusion constants of K^+, Cl^- and $Ru(bipy)_3^{2+}$ are 1.96×10^{-5}, 2.00×10^{-5} and $0.52\text{x}10^{-5}$ cm^2/s, respectively. If the contribution of current is mainly from diffusion and electrophoresis, the conductance of the same concentration KCl and $Ru(bipy)_3Cl_2$ solution should be similar (note the Cl^- concentration in $Ru(bipy)_3Cl_2$ is twice the value of Cl^- in KCl).

Control devices were also fabricated with various leakage pathways by deliberately damaging the devices. For a control device with a big leakage pathway, made by a mechanical scratch on PMMA surface or by using longer times and higher intensities of oxygen plasma treatment, the measured conductance of KCl and $Ru(bipy)_3Cl_2$ are similar. However, the ionic conductance of $Ru(bipy)_3Cl_2$ obviously suppressed for device with 40-90 sec oxygen plasma treatment (**Figure 5.5a**). The decrease in ionic current is similar to the working device. The small PMMA pathways may also hinder the movement of bigger cations. Thus, an ion size dependence of the current is not necessarily a signature of transport through SWCNTs. However, no gatable current was observed in all the devices that were made to leak via deliberate damage (**Figure 5.5c**). Thus the degree of gatability is a conclusive test of transport via the SWCNT.

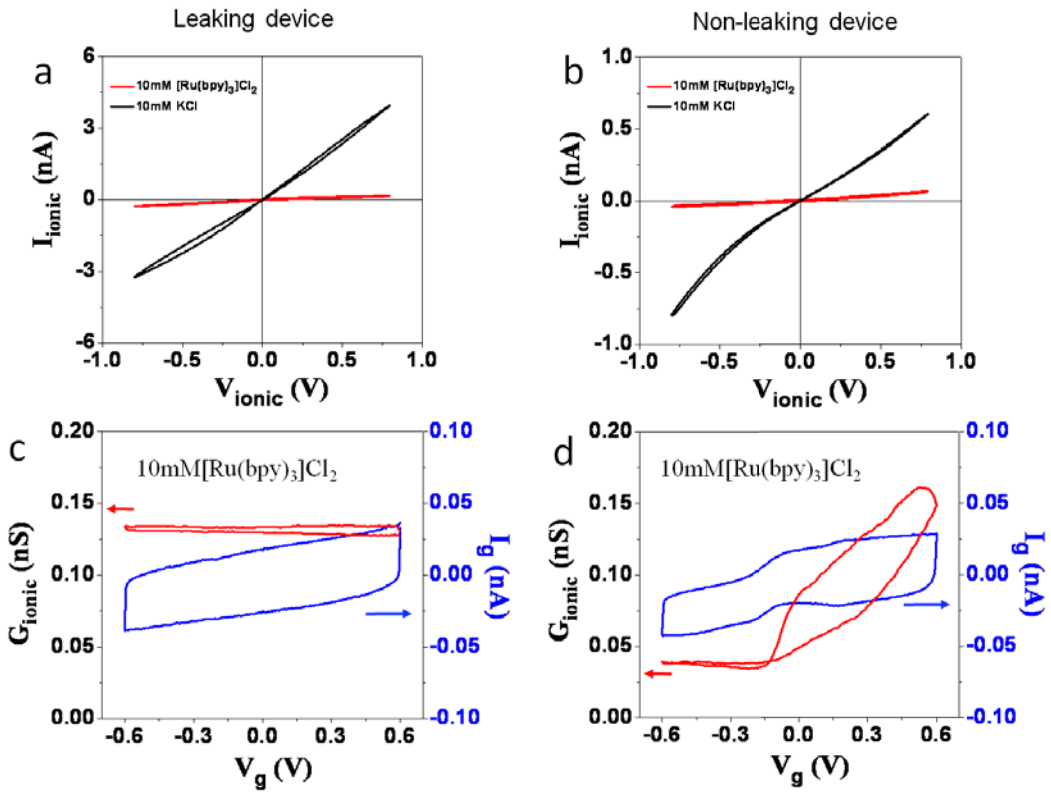

Figure 5.5 The I_{ionic}-V_{ionic} curves of both a leaking (deliberately damaged) device (a) and working (non-leaking, non-damaged) device (b) for both 10mM KCl (black curve) and $Ru(bipy)_3Cl_2$ (red curve) electrolytes. The G_{ionic}-V_g (red curve) and I_g-V_g (blue) curves of both the leaking device (c) and the non-leaking device (d).[89]

5.4 Quantitative Analysis and Simulation of Ionic-FET response

The simulations were carried out at ORNL based on the continuum approximation (Chapter 3), assuming a micro-nano incompressible Newtonian fluid system in a steady flow, with small Knudsen and Reynolds numbers, with conservations of mass, energy, momentum and charge. Approximating the geometry with the an azimuthally symmetric system (illustrated in **Figure 5.6a**) the problem is reduced to a two-dimensional set of the Poisson-Nernst-Planck and Stokes (PNPS) time-

independent coupled partial differential equations (Chapter 2), which were solved numerically, self-consistently, while achieving high accuracy and full convergence. The huge range of scales, from micron sized reservoirs and CNT lengths, to the ~ 2 nm diameter of the SWCNT channel poses significant numerical challenges. In particular, errors in the regions around the ends of the tubes are manifested in breakdown of the required conservation of the total currents through the device. These problems were overcome with the use of an adaptive numerical mesh and a slight rounding the ends of the SWCNT.[89] These difficulties preclude modeling of a full sized system with a 20 μm long SWCNT. It was decided not to compromise the small diameter of the nanotube (here d=2 nm), but rather to reduce the axial length of the tube to L=50 nm, keeping d/L<<1, with appropriate adaptations of other system dimensions as in **Figure 5.6a**. Some tests of length effects are done using model SWCNTs with L of 200 nm and 500 nm.[89] Detailed analysis is carried out only for the numerically most convenient 50 nm case. Scaling to longer tube lengths is not straightforward because of the variation of the electric fields through the tube length. A particularly large voltage drop close to the tube ends and large gradients of the excess charge concentrations cause strong mixing of various components of the electric current in that zone (electroosmotic, electrophoretic, diffusion), as discussed in detail.[89] The significance of the end effects decrease with the tube length, and the tube model of L=50 nm

is not immune to these effects. However, this complication does not invalidate a key outcome of the simulation: the ratio of the electroosmotic conductance to the electrophoretic conductance is found to be >20 for L=50 nm, accounting for the very large conductances observed in the experiments. In the longer model tubes, the current is almost entirely electroosmotic in origin (the ratio of electroosmotic to electrophoretic conductance is >200:1 in 200 nm long tubes and > 3000:1 in 500 nm long tubes).

A perfect slip boundary condition, applied at the CNT inner surface[93], is responsible for large electroosmotic current through the tube.[65] The molecular dynamics simulations[89] show that the slip length on SWCNT inner surface is much larger (at least one order of magnitude) than the diameter (2 nm) of the SWCNT, for all charged CNT surfaces considered in this study, which validates use of the perfect slip boundary conditions at the inner surface of the model SWCNTs. The total negative charge, Q, assumed to be on the CNT surface, is a key parameter that has to be determined by fitting experimental data because it almost certainly arises from sources external to the tube. In case of V_g=0, our experimental measurements with both L=20 μm (present) and L=2 μm[65] SWCNT show almost perfect linear dependence of conductance on salt concentration when plotted on a log-log scale, having the slope in range 0.3-0.4. Our

calculations for various (much shorter) lengths of 50 nm and 200 nm also show a similar dependence of G on c, where the slope and the quality of the power law fit depends on Q. Therefore, a reasonable hypothesis for determination of Q is that the G(c) for V_g=0 is in the form of the power law, $G=A(L)c^b$, where possible length effects are contained in the prefactor *A(L)*, while the exponent *b* is independent of the tube length. The set of measured data in **Figure 5.2b**, showing b=0.37 for V_g=0, is used as input in our fitting procedure. We discuss the inverse problem of finding Q by solving the PNPS equations for various *c* and Q, and finding the best fit of the hypothesized exponent *b* from the computed results with the experimental value of 0.37. The value of Q obtained this way is length dependent. Thus, Q=37.5*e* for L=50 nm (~0.003*e* per carbon atom), and Q=312.5*e* for L=200 nm (~0.006*e* per carbon atom), with b=0.37 in both cases. With Q determined, we have calculated the mean electroosmotic mobilities in the model CNTs, which are about 10^{-6} m^2/Vs for L=50 nm and about $1x10^{-5}m^2$/Vs for L=200 nm at c=0.1M. These values are about one (L=50 nm) or two orders (L=200 nm) higher than the electrophoretic mobility of potassium ion in bulk solution. The calculated mobilities are also comparable to the recent experimentally determined mobilities for potassium ions in one or a few SWCNTs[84] and about 2 or 3 orders higher than the value measured in big modified MWCNTs[94] (where electrosmosis probably does not dominate).

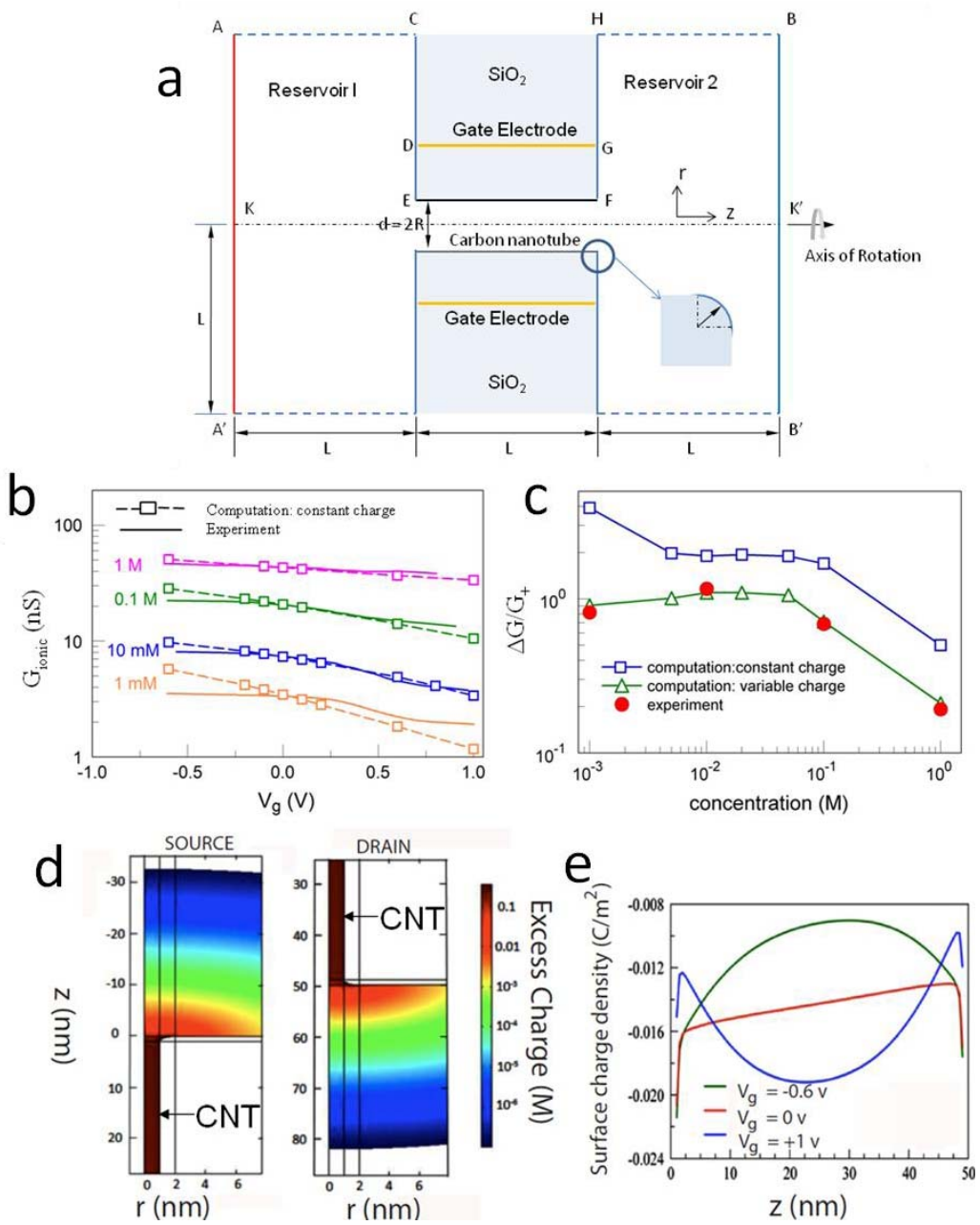

Figure 5.6 Comparison between simulated and measured FET characteristics.[89] (a) Geometry of the idealized axially-symmetric system. (b) G_{ionic} vs. V_g at different KCl concentrations as marked. Lines are measured data (sweep down only). Squares are simulated conductances based on solution of the PNPS equations with constant charge. (c) Gating efficiency, $\Delta G/G_+$, as a function of salt concentration. Blue squares and green triangles are predictions from solutions of the PNPS equations at constant charge and variable charge conditions respectively (lines serve as guides to the eye). Red filled circles are experimental data. (d) Spatial

distribution of excess volume charge density ($\log(c_+-c_-)$ in M units) in the reservoirs near the CNT mouths (only one side is shown here) for V_g=-0.6V at 10mM KCl. Distortions owing to the small size of the model reservoir (50 nm) are not significant because excess charges in the reservoirs fall more than three orders of magnitude at 10 nm away from the CNT mouths. (e) Axial distribution of the surface charge density along the CNT surface for different values of V_g. (V_g, -0.6V (green), 0V(red) and 1V(blue)). All the simulations in this study were carried out at 10x the experimental electric field to avoid numerical noise, but this is in a region where the current to voltage scaling is linear, so that the calculated conductances are unaffected.

With the simulated G_{ionic}-V_g curves for various concentrations, the solutions of PNPS equations show the general agreement with the experimental data. **Figure 5.6b** shows typical experimental data (sweep-down only) as solid lines. The general trend of G_{ionic} vs. V_g is fitted quite well using the constant charge Q deduced from the G_{ionic} vs. c curves in **Figure 5.2a**, and normalizing G at one *c* to the experimental conductance. A nearly perfect fit can be obtained by allowing Q to vary by a small amount with gate bias, to reflect polarization of the barrier material.[89]

The amount of gatable current (*i.e.*, the gating efficiency, $\Delta G/G_+$) varies non-monotonically with salt concentration. The gate efficiency versus concentration, obtained both from the measured (filled symbols) and simulated data (hollow symbols) is shown at **Figure 5.6c**. In addition to values of the KCl concentrations in experiment, there are also the calculations for additional concentrations (for 5, 20, 50 mM). Both constant and variable charge PNPS simulations reproduce well the shape of the

measured gate efficiency curve for c > 5 mM including the plateau between 5 and 50 mM, while the curves diverge from each other at small concentrations (1mM). Further insight in the gating efficiency is given in **Table 5.2** below, illustrating its dependence on c, based on just the electroosmotic currents. The difference of about factor 2 between the two curves in **Figure 5.6c** reflects the difference between the measured and calculated data in **Figure 5.6b**, which reaches a maximum at the ends of the range of V_g considered. This observation suggests possible strong sensitivity of the CNT charge to gate potential in low salt concentration conditions.[89]

Very large excess charge gradients (with correspondingly high electric fields) accumulate near the entrance and exit of the SWCNT as shown for the case of 10 mM electrolyte and a 50 nm long SWCNT in **Figure 5.6d**. The reservoir width in these simulations was also 50 nm, but the large charge gradients in the reservoirs are localized to within 10 nm of the tube entrances, confirming that the present reservoir size is good enough for describing the behavior of the real reservoirs. The excess charge accumulation within the tube is relatively constant and set mainly by the surface charge on the tube. This excess volume charge increases with electrolyte concentration and negative gate bias (**Table 5.2**). Electroosmotic current within the tube is driven by the axial field caused by

the imbalance between the charge accumulation at the source and drain ends of the tube. **Figure 5.6e** shows the axial distribution of surface charge that gives rise to this driving field. The axial surface charge gradient along the tube is essentially constant at V_g = 0 (red line). The surface charge has a positive peak when V_g = -0.6V (green line) and is reduced when V_g = +1V (blue line - note the charge accumulation near the ends of the tube that balances the fields at the entrance and exit reservoirs near the mouths of the tube). The electric fields in the entrance and exit regions of the reservoirs are decreased as the bulk concentration of electrolyte approaches the concentration of excess ions inside the tube, with the consequence that much more of the applied bias is dropped in the form of an axial field inside the tube. The increased axial field gives rise to increased electroosmotic flow. However, as the internal field grows larger, it is less influenced by the gate field, whose magnitude is limited by the breakdown value of the dielectric layer. Thus, at low salt, the amount of current that can be gated increases with increased electroosmotic flow, but above 10 mM salt the field inside the tube is too large to be affected significantly by the gate. This leads to the peak/plateau in gating efficiency shown in **Figure 5.6c**.

Salt concentration	V_g (V)	Excess charge n(M)	E-field E (V/m)	nE	$(nE)_-/(nE)_+$-1
	-0.6	0.175	4152.0	726.2	0.732
1 mM	0.0	0.252	2975.9	749.9	
	1.0	0.276	1518.1	419.3	
	-0.6	0.329	8242.1	2713.3	
10 mM	0.0	0.302	7938.0	2401.2	1.542
	1.0	0.168	6357.7	1067.4	
	-0.6	0.401	15383.0	6170.1	
0.1 M	0.0	0.376	15126.8	5681.6	0.661
	1.0	0.268	13849.9	3714.5	

Table 5.2 Analysis of fields, charges and flow along r = 0.9 nm for a 50 nm long tube. Note that this selection of the tube volume results shows a volume charge that is not the same for each value of V_g=0 (but the integrated charge is, of course).[89]

5.5 Origin of the Charge on SWCNT

The CNT based ionic FET characteristics were strongly dependent on pH (**Figure 5.7**). The current through the SWCNTs is greatly reduced at pH 3 and is no longer gatable. The amount of gatable current is a maximum near pH 4, close to the pK_a of the terminal carboxylates on the SWCNTs. These observations suggest that charged residues on the ends of the SWCNT (and possibly the surface of the reservoirs) contribute to the charge on the tube.

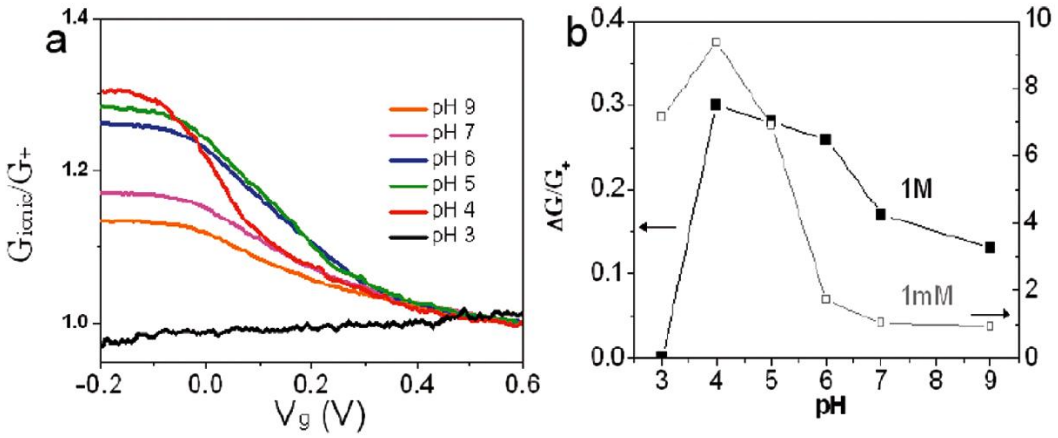

Figure 5.7 Tube charge is extrinsic and modulated by pH.[89] (a) G_{ionic}/G_+ vs. V_g at different pH (sweep-down curves). (b) Gating efficiency $\Delta G/G_+$ vs. pH in 1M (black) and 1mM KCl (gray, right axis).

5.6 Conclusion

We successfully fabricated ionic FETs using individual SWCNTs. They display stable p-type ionic transistor characteristics, showing that the charge carriers are cations when a KCl electrolyte is used. Ion transport is turned off by the application of a positive gate bias, indicative of a negative charge on the channel. The characteristics of the devices are well-accounted for by simulations that show that the vast majority of the current is carried by electroosmosis, with only a small amount carried by electrophoretic and diffusion currents. The very large electroosmotic current arises from the nearly frictionless flow of water inside the SWCNTs, accounting for the giant ionic currents that flow through these devices. Devices based on a single SWCNT nanofluidic channel will probably offer new approaches for controlling the flow of biological molecules in

nanochannels based on the charge sensitivity of the large electroosmotic flow.

6. ELECTRONIC SENSITIVITY OF CARBON NANOTUBES TO INTERNAL WATER WETTING

6.1 Introduction and Motivation

The excellent electronic properties, small pore size and large surface to volume ratio of single-walled carbon nanotube (SWCNT) form the basis of a large number of new types of electronic sensors[95-97] in which analytes generate a signal by binding to the outside of a SWCNT. However, the interior of SWCNT is unexplored territory for chemical and biological sensor applications. How does *internal* water wetting affect the electronic properties of the SWCNT (and the properties of the contacts to it)?

Counter intuitively, the hydrophobic interior of SWCNTs is readily wetted because the surface tension of water is much lower than the threshold value.[98, 99] Microscopically the chemical potential of water is lower inside the SWCNT than in the bulk,[43] and water can be transported at many thousand times the speed possible with classical Poiseulle flow.[43, 53, 54, 100] Internal wetting of CNTs has been verified by transmission electron microscopy (TEM)[101] and a number of spectroscopy methods,[102-107] showing that water is ordered inside a CNT. The transport of water, ions and small molecules through CNTs has also been studied experimentally using membranes consisting of billions of carbon nanotubes in parallel.[53, 54, 108] Besides, in our studies of ion and DNA translocation through

individual SWCNTs[65] by making devices in which just one SWCNT connects two fluid reservoirs, ionic currents were found to be much larger than predicted by a standard electrophoresis model and DNA translocation was accompanied by electrical signals that differed drastically from what is observed in other inorganic nanopores.[109-111] A very recent study showed yet another (proton dominated) mode of transport in very long SWCNTs.[107]

SWCNT field effect transistors (FETs), show that the electronic properties of SWCNTs are sensitive to their diameter, chirality, defects, doping,[112] adsorbates[113, 114] and environment[96], though these effects can be masked by the dominant role of Schottky barriers at the metal-SWCNT junction.[115, 116] Wetting of the outside of SWCNT-FETs by water changes their hysteresis and shifts their threshold gate voltage (V_{th}).[117-120] The resistivity of SWCNT mats falls when they are wetted (possibly both inside and outside)[104, 121] but these results are difficult to interpret in terms of the response of individual SWCNTs. Thus, we have used our new devices, in which just one SWCNT connects two fluid reservoirs to compare the effects of external and internal wetting on SWCNT-FETs.

6.2 CNT Device Design and Experiment Methods

The combined nanofluidic-CNT-FET is shown in **Figure 6.1**. It consists of a single CVD grown SWCNT that connects two fluid reservoirs formed in a PMMA resist using e-beam lithography. Source and drain electrodes are evaporated onto the SWCNT under the barrier [122, 123] and a heavily doped p-type silicon substrate acts as a backgate. Only the SWCNT under the barrier remains after the exposed SWCNT in the reservoirs has been etched with an oxygen plasma.[65] The fluidic path is completed by attaching a PDMS cover containing microfluidic channels. Further details of the fabrication are given in the Fabrication part (Chapter 2).

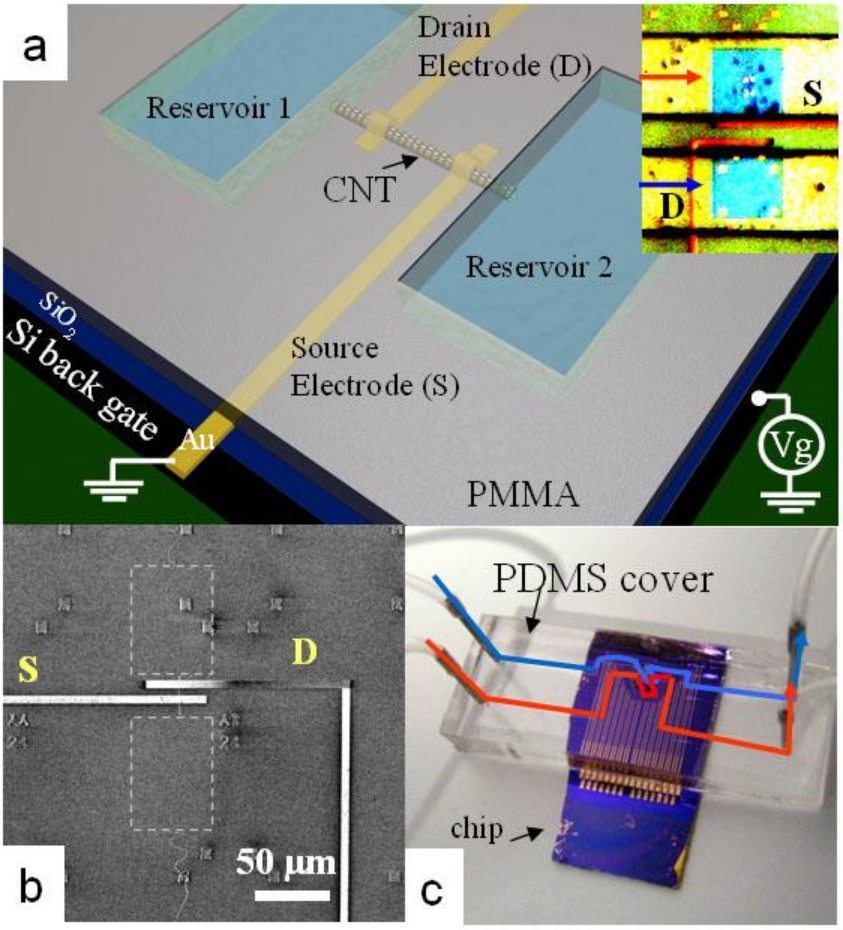

Figure 6.1 Measurement of a SWCNT nanofluidic channel integrated with a SWCNT field effect transistor.[124] (a) Schematic of the device structure and electrical measurement configuration. The inset shows an optical image of a device. The two blue squares (*i.e.*, 60 µm x 60 µm) are the fluid reservoirs cut into the PMMA (yellow). Areas contacted by the PDMS cover are shown in green. Fluid flow in the PDMS channels is indicated by the red and blue arrows. The distance between source (S) and drain (D) electrodes (red) is 15µm. (b) Scanning electron microscopy (SEM) image of a single reservoir device after stripping off the PMMA layer to show the SWCNT lying under the electrodes. The areas labeled by the gray dashed squares indicate the position of the reservoirs. (c) Optical image of a device assembled with a PDMS cover for solution delivery. The red and blue lines show the fluid paths.

Individual p-type semiconducting CNT-FETs were first characterized prior to open the SWCNTs, both dry and with the exposed SWCNT wetted externally, followed by the opening of the SWCNTs and the recording of FET characteristics with the tube dry and wet. Only internal wetting had a significant effect on the characteristics of the device. Furthermore, vacuum drying of the SWCNT restored the pre-wetting characteristics. For controls, we (a) exposed the SWCNT between source and drain electrodes and wetted the tube externally in this region; (b) connected an electrode to the fluid reservoir and altered its potential (the extent possible with pure water) (c) varied the degree of plasma treatment of the reservoirs to alter surface charge in the reservoirs. None of these controls altered the response of the SWCNT significantly. Thus, we conclude that water inside of the tube affects the contacts (and probably the band structure) of the tube in a way that water on the outside of the tube does not.

6.3 Internal and External Water Wetting of CNT

Representative data for one tube before opening are shown in **Figure 6.2a**. The source-drain current (I_{DS}) versus backgate voltage (V_{GS}) curves are for the dry tube in air (black curves) and for the tube externally-wetted in the reservoir area (red curves). We observe an increase of hysteresis and a shift of the threshold gate voltage (V_{th}) as reported earlier for external wetting.[117-120] Immediately after a gentle (~30sec, 7.2 W) oxygen

plasma treatment to open the SWCNT, we find that I_{DS} decreases a little in the saturation current region and V_{th} shifts slightly (black curve, **Figure 6.2b**). The characteristics change dramatically a few minutes after injection of water into the reservoir to wet the interior surface of the tubes (red curve, **Figure 6.2b**). The backgate bias no longer has any effect over the range of bias we can apply without breakdown. The transition is independent of drain-source bias as shown in heat maps (**Figure 6.2c** and **d**) of I_{DS} as a function of both V_{DS} and V_{GS}. Transistor action in the dry device (**Figure 6.2c**) is abolished over the entire range of V_{DS} and V_{GS} when it is wetted internally (**Figure 6.2d**). Furthermore, the effect is quite reversible: vacuum drying restores the function of the backgate (green curve, **Figure 6.2b**). Note that the "on" conductance of the tube does not change dramatically when the tube is internally wetted, the main effect being abolition of the action of the backgate.

When a p-type SWCNT-FET (keeping the electrodes protected) is externally wetted, its threshold moves towards more negative gate bias and hysteresis increases.[117-120] Internal wetting produces exactly the opposite result: the threshold moves to more positive gate bias and the hysteresis decreases.

Internal wetting abolished gating reversibly in 11 out of 18 measured semiconducting CNT devices, and diminished it in 3 of the remaining 7 devices. Thus, the observation is not a result for a specific chirality or diameter, but a rather general property of single-walled semiconducting carbon nanotubes.

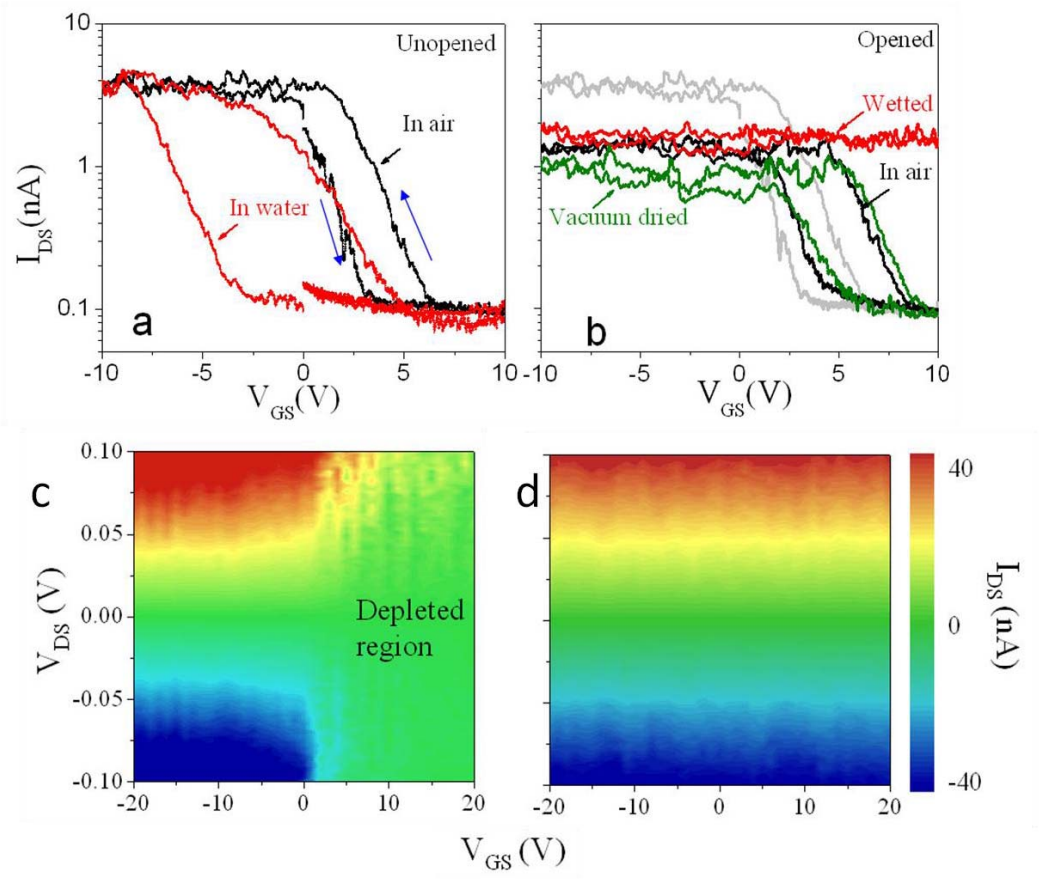

Figure 6.2 Effects of wetting on electronic transport in a SWCNT.[124] (a) External wetting: I_{DS}-V_{GS} semilog curves for an unopened p-type SWCNT device before (black) and after (red) filling the reservoirs with water at V_{DS}=0.5V. The blue arrows indicate the direction of the V_{GS} sweep. (b) Internal wetting: I_{DS}-V_{GS} curves (V_{DS}=0.5V) before opening (grey), after opening with an oxygen plasma (black), after water is added to the reservoirs (red) and after the tube is subsequently dried in vacuum (green). (c) Heat map of I_{DS} (green = zero current) as a function of V_{GS} and V_{DS} for an unopened p-type SWCNT-FET. (d), as in (c) but internally wetted. The SWCNT is now ohmic over the entire range of V_{GS} and V_{DS}.

Some trivial causes for this effect can be ruled out. It is not a consequence of a short circuit between drain and source caused by external wetting. No amount of exposure to water alters the p-type FET response unless the SWCNTs are opened. The influence from oxygen plasma treatment on tube can be also ruled out. Freshly opened tubes that are not exposed to water show p-type transistor action with characteristics only a little different from those measured prior to opening the tubes (black curves, **Figure 6.2b**).

Another possibility is that the surface charges in the water reservoirs generated by oxygen plasma treatment may "pin" the potential of the CNT (through the poorly conducting medium of the water) out of the range of the backgate potential. A water gating measurement is carried out to measure the effect of sweeping the potential of a quasi-reference electrode (Pt wire) in contact with the water (**Figure 6.3a**). This reference electrode ("V_{wg}" in **Figure 6.3a**) plays the role of introducing a strongly-charged surface into the reservoir. The electronic transport characteristics of the CNT-FET device (with both unopened and opened CNT) were not sensitive (**Figure 6.3b** to **d**) to the potential applied to the "water-gate" potential over a range of three volts, a potential change much larger than could be produced by any reasonable change in surface charge. Thus we can conclude that surface charges in contact with the water reservoir do

not play an important role in our device. The most likely explanation for this is the high resistivity of (reasonably) pure water. Thus the potential of water inside the tube will be dictated by interactions with the tube, unless salt is added to the reservoirs.[125]

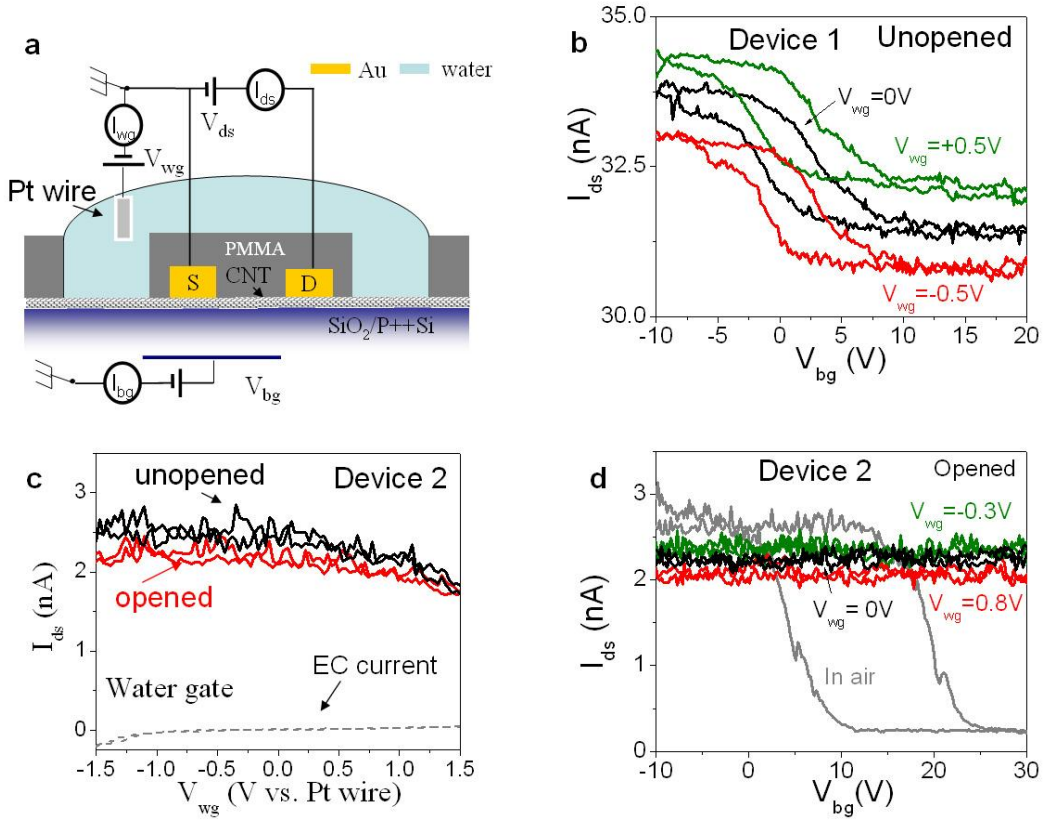

Figure 6.3 (a) The illustration of the water gating experiment for an unopened CNT.[124] Pt wire is used as the water gate electrode. Pure water filled the reservoirs. Both water gate bias (V_{wg}) and back gate bias (V_{bg}) are applied to gate the CNT FET device in the measurements. (b) The source drain current (I_{ds}) of device 1 with unopened CNT as a function of V_{bg} at different V_{wg}. The V_{ds}=0.1V. (c) The I_{ds} as a function of V_{wg} of device 2 both for unopened CNT (black) and opened CNT (red). The V_{ds}=1V. The electrochemical (EC) current between Pt wire and the source electrode was measured and the value was negligibly small. (d) The I_{ds} as a function of V_{bg} for device 2 with opened CNT. The p-type transistor behavior was observed in air (gray) but disappeared after been wetted. There different V_{wg} were applied to the device but they could not restore the p-type transistor.

We also measured 3 metallic CNT devices and all showed decreased conductance after water filling. Typical results for a metallic tube are shown in **Figure 6.4**. Before opening the tube by oxygen plasma, the device showed negligible response to water (**Figure 6.4a**). After the tube ends were opened by oxygen plasma, I_{ds} decreased. I_{ds} decreased further after water was added to the reservoirs and recovered after vacuum dried as shown in **Figure 6.4b**. The decrease of conductance during filling is shown in **Figure 6.4c**.

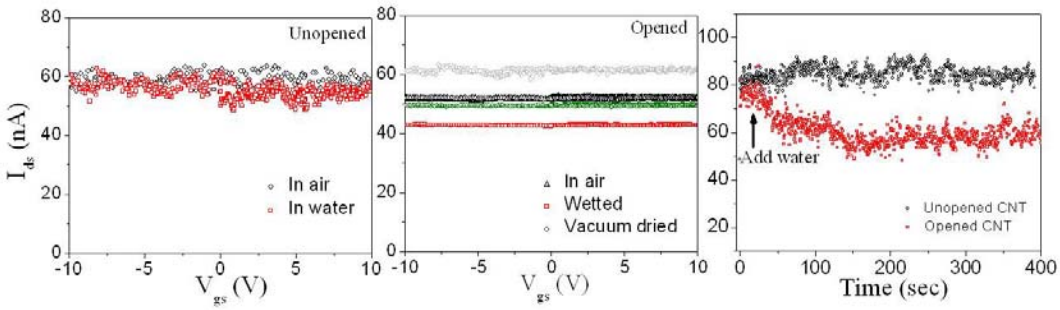

Figure 6.4 (a) I_{ds}-V_{ds} curves of a device with unopened metallic SWCNT before (black) and after adding water (red) into the reservoirs. (b) The same device was measured after opening with an oxygen plasma (black), after water was added to the reservoirs (red) and after the tube was subsequently dried in vacuum (green). Unopened CNT data (gray) measured in air are shown here as reference. V_{ds} = 0.8V for both (a) and (b). (c) I_{ds} time traces during adding water into the reservoirs for both unopened and opened tubes at V_{ds} = 0.8 V and V_{gs} = 10 V.[124]

Studies of external wetting[117-120] have been carried out using a window opened in dielectric material that covers the metallic contacts (**Figure 6.5**). The structures of the two devices are illustrated in the insets of **Figure 6.5a** and **c**, respectively: only a short section of the SWCNT between the

two electrodes is exposed to water. The source (S) and drain (D) electrodes are protected by a PMMA layer. In both devices the hysteresis increases and the device remains p-type. A trace of I_{ds} vs. time is shown in **Figure 6.5c**. No change was observed after adding water into the reservoir. The difference between internal and external wetting may just reflect the fact that the tube is not wetted all the way up to the contact in the external wetting process. To check for this, we opened a window that exposed the electrodes as well. The device structure is shown in the inset of **Figure 6.5d**. The reservoir size is 60 μm x 60 μm, the Au electrodes are 5 μm in width and the distance between the two Au electrodes (edge to edge) is 5 μm. We first checked the leakage current between two gold electrodes (**Figure 6.5d**). When the electrodes are completely covered with PMMA, the current between two electrodes is negligibly small. When the electrodes are exposed to air, some leakage current appears. After adding water to the reservoir, the leakage current increased only slightly. We then measured the device with a SWCNT between two electrodes (**Figure 6.5e**). After adding water, the transistor action still remains. However, the threshold voltage V_{th} shifted significantly to the positive direction and the current at subthreshold region increased. These changes may due to the modification of gold work function and the Schottky barrier at contacts during external wetting. External wetting of the tube all the way up to the contacts did move the threshold to more positive gate bias but

did not result in abolition of gating. So this difference between external and internal wetting does not account for the effects of internal wetting.

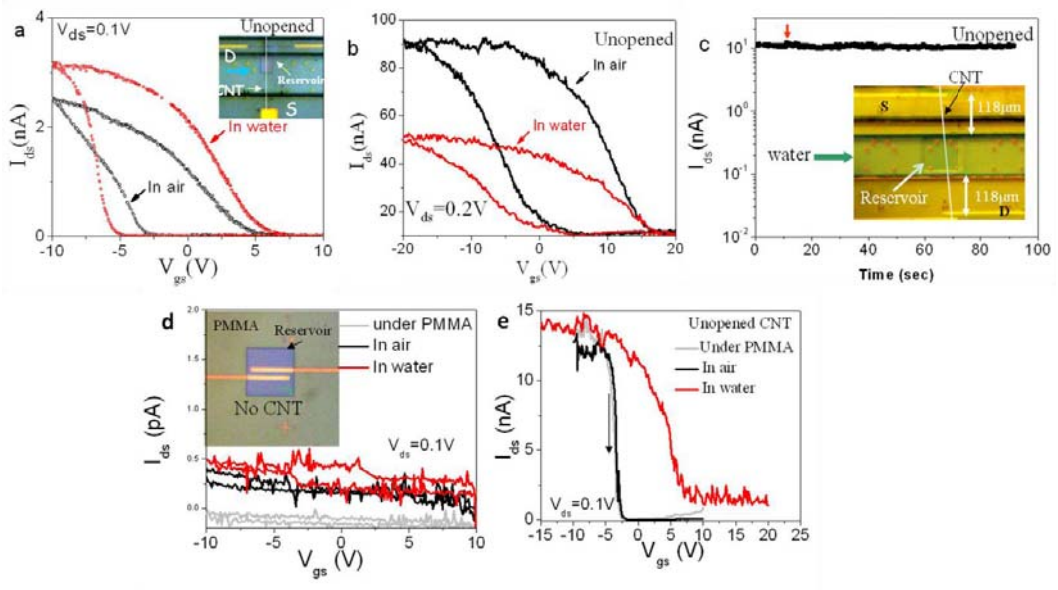

Figure 6.5 External wetting: (a) I_{ds}-V_{gs} curves for one control device with a section of CNT between source and drain electrodes, with dielectric material covered, in air (black curve) or in water (red curve). As shown in the inset, the reservoir opened along the CNT path is about 60 μm in length and the distance between D and S is about 140 μm. (b) I_{ds}-V_{gs} curves of another control device. (c) I_{ds} time trace of the same device as (b) when exposing the outside of CNT to a water bath at V_{gs} = 20V and V_{ds} = 0.5V. The optical image of the device structure was shown in the inset. (d) I_{ds}-V_{gs} curves of control devices with exposed electrodes without a CNT. The devices were measured before opening reservoir (gray), before (black) and after (red) exposing the metal electrodes to water. (e) I_{ds}-V_{gs} curves of another control device as (d) but with a CNT. For both devices, the reservoir size is 60μm x 60μm and the Au electrode is 5 μm in width and 45 nm in thickness (as shown in the inset of (d)).[124]

6.4 Mechanism of Water Wetting Process in CNT

Molecular dynamics and electronic structure calculations for water confined inside a SWCNT were carried out by our collaborators at ORNL to investigate these effects further. For the internal wetting of the tube, a 2.84 nm long semiconducting (10, 0) tube (0.78 nm diameter) was filled with equilibrated water structure. The resulting water structure is a single-file hydrogen-bonded "wire" (**Figure 6.6**). The dipole orientation of such water structure and the importance of the dipole orientation to the water transport through CNT have been studied before.[126, 127] According to these estimates, the dipole field of this water structure is in magnitude competitive or even stronger than the electrical field of the backgate in both axial and radial components. This dipole field causes redistribution of the charges at the CNT and contact electrodes which cancel the dipole field but also influences the electronic characteristics of the tube, including Schottky barriers. The water dipole will flip frequently[128] but the flipping can be suppressed by the drain-source field. In contrast, external water generates essentially no dipole field. Thus internal water may generate an electric field and polarizes the tube and metal electrodes that modify the Schottky barrier at the contacts. These effects are not seen at external wetting.

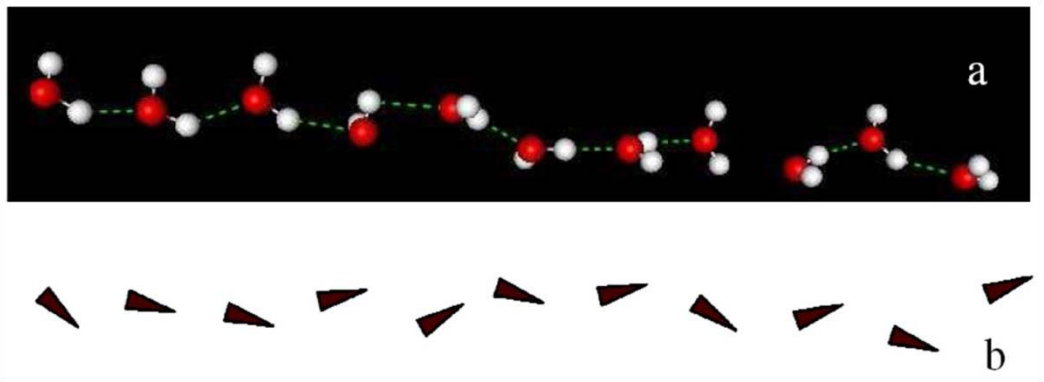

Figure 6.6 (a) Partially ordered nanosutructure of the waters, filling the narrow CNT, connecting with H-bonds. (b) Ordering of the water dipoles; an arrow tip in the direction of a dipole, which is by convention from negative toward positive charge.[124]

Secondly, internal water may also modify the electronic structure of CNT, as suggested by the IR spectroscopy.[105] Density Functional Theory (DFT) electronic structure calculations was also carried out by using the same CNT (10,0) tube. The CNT was filled with optimized and thermally equilibrated (300K) water structure (**Figure 6.7**), using molecular dynamics simulations as discussed in the previous paragraph. A decrease in the bandgap was observed when water molecules fully fill the CNT (red curve in **Figure 6.7c**). The gap was changing dominantly by shifting up the top of the valence band, while the bottom of the conduction band was almost unchanged. The bandgap is also reduced when water molecules are placed outside the tube. However, the decrease is much smaller (~15%) even when a large number (115) of external water molecules were used. The reduction in the bandgap of CNT originated from the enhanced

interaction between ordered structure of water molecules and the carbon atoms. Significantly stronger interaction is observed when water molecules are confined inside the tube (insets in **Figure 6.7c**), leading to a penetration of the occupied levels of oxygen into the CNT band gap. No shift in the CNT Fermi level was observed and there was no charge transfer between internal water molecules and carbons. The CNT bandgap reduction will lower the Schottky barriers and push V_{th} to a larger positive value.

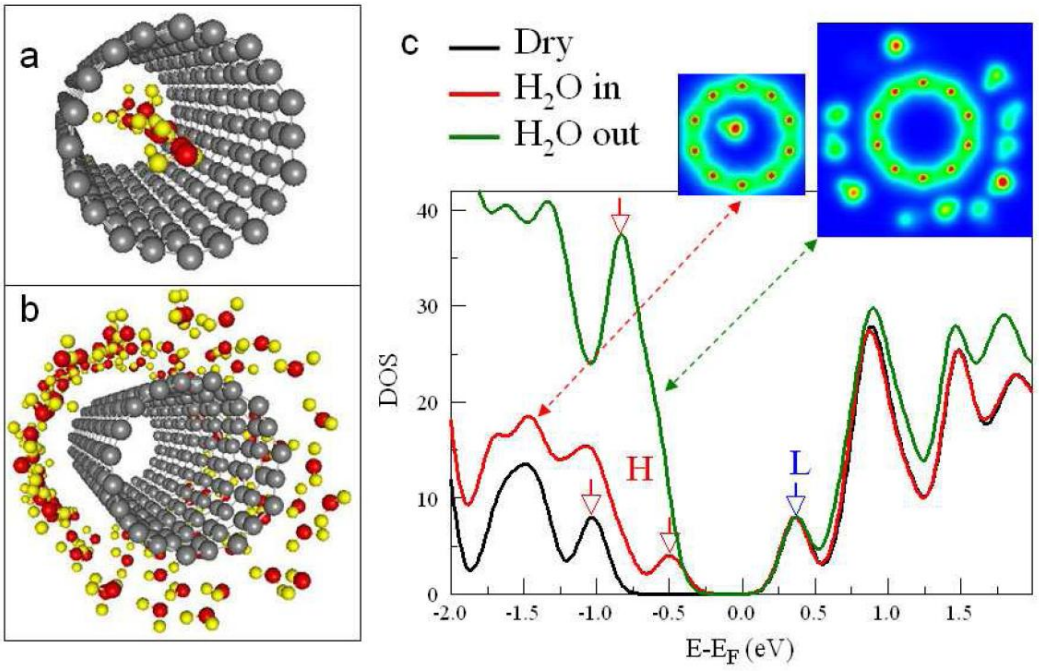

Figure 6.7 Calculated HOMO-LUMO gap for wetted SWCNT:[124] (a) Structure of a (10, 0) SWCNT of length 2.84 nm, filled with 11 water molecules (0.13 eV smearing). (b) Structure of a (10, 0) SWCNT with 115 water molecules surrounding at the outside of the CNT (0.54 eV smearing). (c) Density of States (DOS) for the pristine (black), fully water-filled (red) and externally wetted CNT (green). The arrows indicate the HOMO (H) and LUMO (L).The insets are the cut-plane visualization of the electron density of occupied states at the middle length region of the CNT.

Based on these simulations, it is clear that internal wetting can modify the electronic property of device either through dipole electric-field and induced polarizations mediated modification of the Schottky barriers and/or *via* the shift of the valence band owing to the bandgap reduction. We devised an experiment to separate the effects of internal wetting on the contacts from the effects on the electronic properties of the tube itself. To do this, we opened the SWCNT at one end only, so that the internal wetting would proceed slowly, passing first one contact, then the interior of the device, and finally the second contact, measuring the current through the device as the wetting proceeded. **Figure 6.8a** shows a typical current vs. time trace for a device gated partially "on" initially. Interestingly, the current first drops and then rises to the saturated "on" value (note the current scale is logarithmic). Since, as revealed quantum calculations, the internal wetting has a minimal effect to the valence band when the wetting is less than 25 % of one side, and becomes really significant at more than 75% of the tube filling, this result implies that wetting increases the Schottky barrier at the first contact, an effect that is eventually counteracted by the upward movement of the valence band. It was shown previously that asymmetric Schottky barriers (generated by different metal contacts,[129] or an extra gate near one contact[130]) will produce rectifying behavior. The wetting process was slowed down when the source and drain electrodes were separated to 100μm so that I_{DS} could be recorded

as a function of V_{DS} as wetting proceeded (the backgate was set to turn the device "on" initially). Initially (1 in **Figure 6.8b**) the I_{DS}-V_{DS} curve was symmetric. However, at intermediate times (2, and 3 in **Figure 6.8b**) the device showed rectification, returning to a symmetric response (4 in **Figure 6.8b**) as both contacts became wetted.

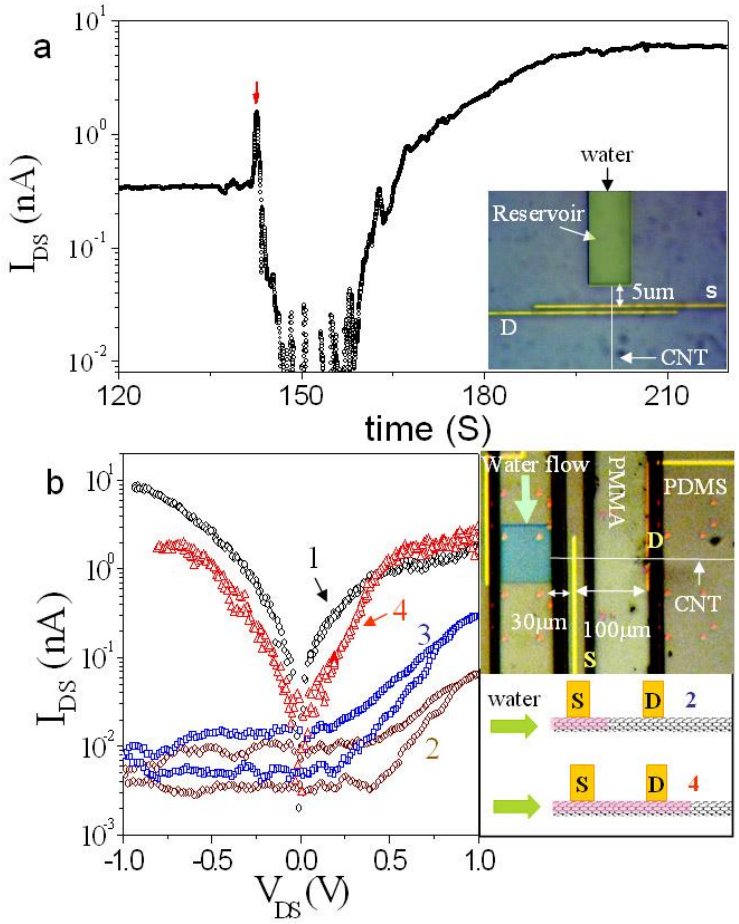

Figure 6.8 Change of electronic properties during wetting.[124] (a) I_{DS} vs. time for V_{GS} = 20V and V_{DS} = 2V. The red arrow marks the point of water addition, with current initially falling before rising to the equilibrium value. The optical microscopy image of the single reservoir device used for this measurement is shown in the inset. (b) I_{DS}-V_{DS} curves (V_{GS}=0 V) for a slow-filling device (inset top right) showing a transition from symmetric behavior (1) to rectification (2,3) and back to symmetric behavior (4) as the internal water propagates into the structure (inset down right).

We can qualitatively account for our observations by assuming (a) that the Schottky barriers is first increased due to the water dipole induced polarizations of the CNT and metal electrodes in particular, as predicted by the molecular dynamics simulations and (b) that the valence band is then shifted upward (narrowing the Schottky barriers) as predicted by the DFT calculations. **Figure 6.9a** shows the device switched "on" (blue dashed lines) at V_{GS}=0 and "off" (orange dashed lines) at V_{GS}>0 when the tube is dry. When water wets the inside of the CNT under the first contact, an increase of the Schottky barrier height (**Figure 6.9b**) leads to a current (I_{DS}) drop. With the further wetting of the CNT interior, the upward shift of valence band (E_V) (**Figure 6.9c**), lowers the Schottky barrier height, turning the device on. A significant shift in E_V and/or a large local polarization field at contacts (due to the induced image charges at electrodes from the polarized CNT) will overcome the ability of the backgate to modulate the conductance (indicated schematically by the smaller difference between the dashed orange and blue lines in **Figure 6.9c** and also turns the device "on" at V_{GS}>0. We often observed a similar or slightly smaller "on" conductance of the devices after water wetting, which implies a similar SB, or a large metal-CNT contact resistance.

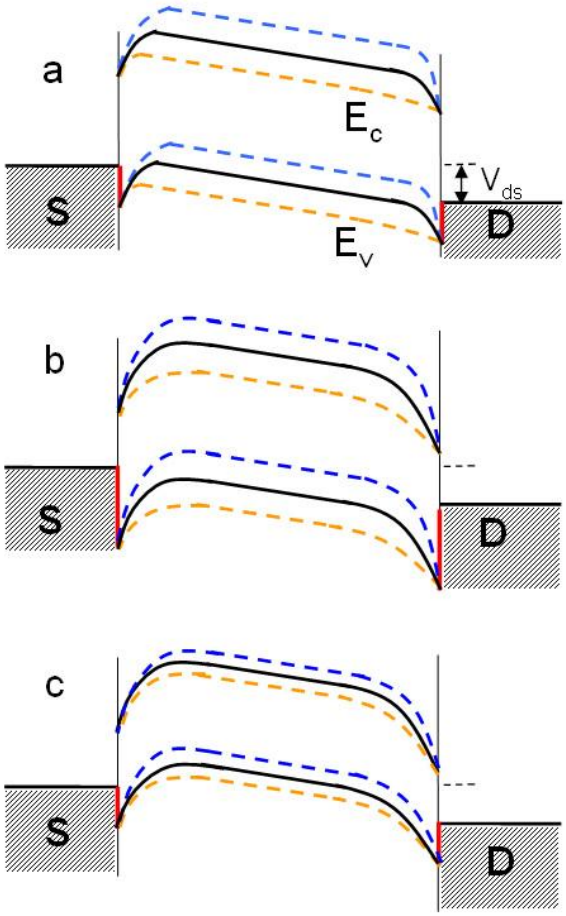

Figure 6.9 Sequential change of the energy band diagrams of a CNT-FET device during water wetting process at a fixed positive V_{DS} and different V_{GS} (orange-positive, black-zero, and blue-negative).[124] (a) The initial diagram before wetting. (b) The increase of SB at contacts. (c) The up shift of valence band (E_V) while the CNT Fermi level is fixed. The red lines indicate the heights of Schottky barriers. S and D are source and drain electrodes respectively. In the diagrams, the contact resistance is neglected and the Fermi level between metal contact and CNT is always in alignment.

Internal wetting with a salt solution (0.1 mM KCl) immediately restored p-type transistor action in tubes that had been rendered insensitive to gating by pure water (**Figure 6.10**). The change may be due to the disruption of the ordered water structure and the water-CNT interaction inside the CNT

by the hydrated salt ions. At 0.1 mM salt, a 15 μm long SWCNT contains approximately 3 K^+ and 3 Cl^- ions and 10^6 water molecules, so water ordering would have to be extremely sensitive to the presence of just a few ions. A second possibility is that the carbon nanotube potential needs to float with respect to the reservoirs for the abolition of gating to be observed. The addition of salt will add the capacitance of all of the electrolyte in the reservoir to that of the tube, effectively pinning the tube potential.

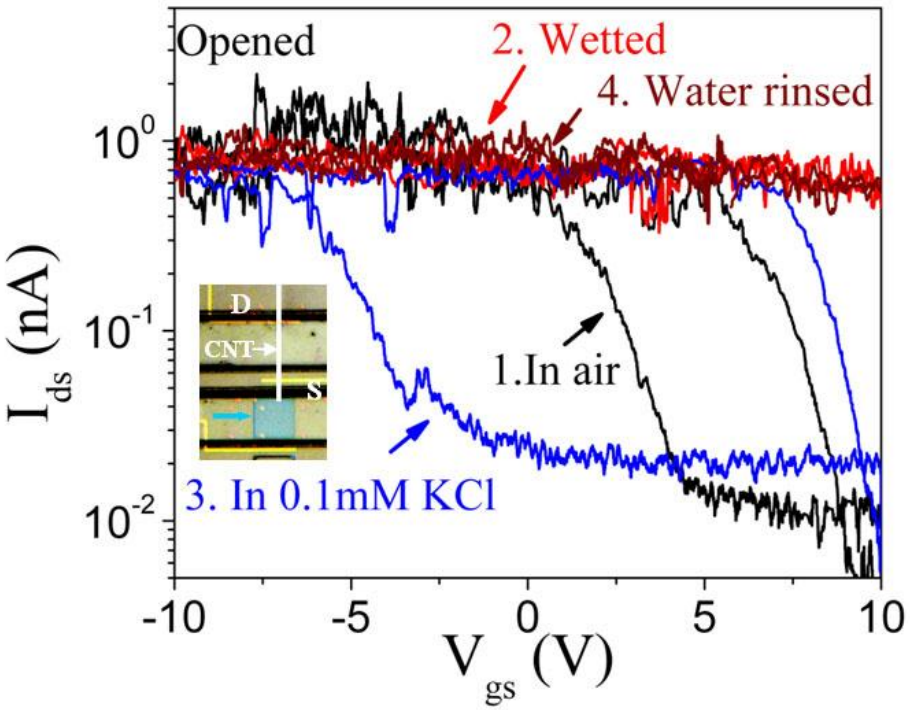

Figure 6.10 Semi logarithmic I_{ds}-V_{ds} curves of a device before (black) and after adding water (red) and 0.1 mM KCl (blue), and after flushing with water (wine).[124]

6.5 Conclusion

We have constructed devices in which the interior of a single-walled carbon nanotube (SWCNT) field-effect transistor acts as a nanofluidic channel that connects two fluid reservoirs, permitting measurement of the electronic properties of the SWCNT as it is wetted by an analyte. The tubes are extremely sensitive to internal water wetting, which turns the transistor on, while wetting of the outside has little effect. These observations are consistent with theoretical simulations that show that internal water both generates a large dipole electric field, causing charge polarization of the tube and metal electrodes, and shifts the valance band of the SWCNT, owing to the nanoconfinement of water, while external water has little effect. Thus this work provides a new method to investigate water at nanoscale. Furthermore, SWCNTs are likely to be even more sensitive to internal analytes than they are to external analytes. Using the inside of the tube as the sensing surface will also permit the SWCNT to be used as a nanopore (for analyzing single molecules[65]) and as a nanoscale sample concentrator because of the ion-selectivity of SWCNTs [131, 132] and the enhanced water flow inside them.[53, 54] Analytes dissolved in water that enter the CNT slowly will accumulate owing to the several-thousand fold enhancement of water flux through the tube.

7. SUMMARY AND FUTURE DIRECTION: MOLECULAR TRANSISTOR

7.1 Summary

In the previous chapters, I have listed the major works that I have performed, including the nanofluidic devices based on individual SWCNT nanochannels for ion and molecule transport, the origin of giant ionic currents through these kinds of devices and finally the electronic sensitivity of CNT to internal water wetting. The preliminary results have shown convincing evidence that single-stranded DNA molecules and nucleotides (GTP) could translocate through a single-walled carbon, when an ionic current is driven through the carbon nanotube channel. Simulations of ion current flow through the carbon nanotube show that it is dominated by electroosmostic flow of water which drags anions and cations with it. A net current flows because the entry of anions or cations into the tube is selective, depending upon factors like surface charges at the entrance to the carbon nanotube. Accordingly, the number of cations (as the major carriers) in the tube is not equal to the number of anions, giving rise to a net charge inside the tube and a net current flow through the tube.

The mechanism described above was also then confirmed by experiment with the CNT based ionic FET. The charge carried by the carbon nanotube is controlled by a gate electrode placed in close proximity to the

carbon nanotube, but insulated from it by a dielectric layer. The CNT based ionic FETs displayed stable p-type ionic transistor characteristics, showing that the charge carriers are cations when a KCl electrolyte is used. This characteristic implies that the charge on the tube (and its immediate environment) is negative. This charge is most likely largely extrinsic, associated with the SiO_2/CNT interface, charge inside the barrier material close to the CNT and at the ends of the tubes, both on the barrier material and in the form of charged carboxylates on the ends of the SWCNTs.

In addition, water wetting of the interior of the SWCNT has great influence on the SWCNT electronic properties, namely that it turns the electronic CNT transistor to “on” state, while wetting of the outside has little effect. With the experiment results, the theoretical simulations also confirm that internal water both generates a large dipole electric field, causing charge polarization of the tube and metal electrodes, and shifts the valence band of the SWCNT, while external water has little effect.

All of these works and findings may provide new methods to investigate molecule behavior at nanoscale and open a new avenue for building CNT based sensors in which the SWCNT simultaneously functions as

nanopore, concentrator or extremely sensitive electronic/electrochemical detector.

7.2 Future Direction: Molecular Transistor based on CNT Nanofluidic Device

7.2.1 Background

Recently, the field of electrically detecting and manipulating single molecules passing through individual nanopore has witnessed tremendous progress. Among various applications, nanopore-based DNA sequencing has been most attractive due to its label-free, amplification-free, single-molecule approach with high-throughput analysis.[30] However, there is a consensus that the electrophoretic translocation of DNA molecules through the nanopores (including protein nanopores and solid-state nanopore) has been too rapid for base identification. Thus, various strategies have been proposed and tested to actively or passively slow down the transport process before readout,[30, 133-136] typically as shown in **Figure 7.1**.

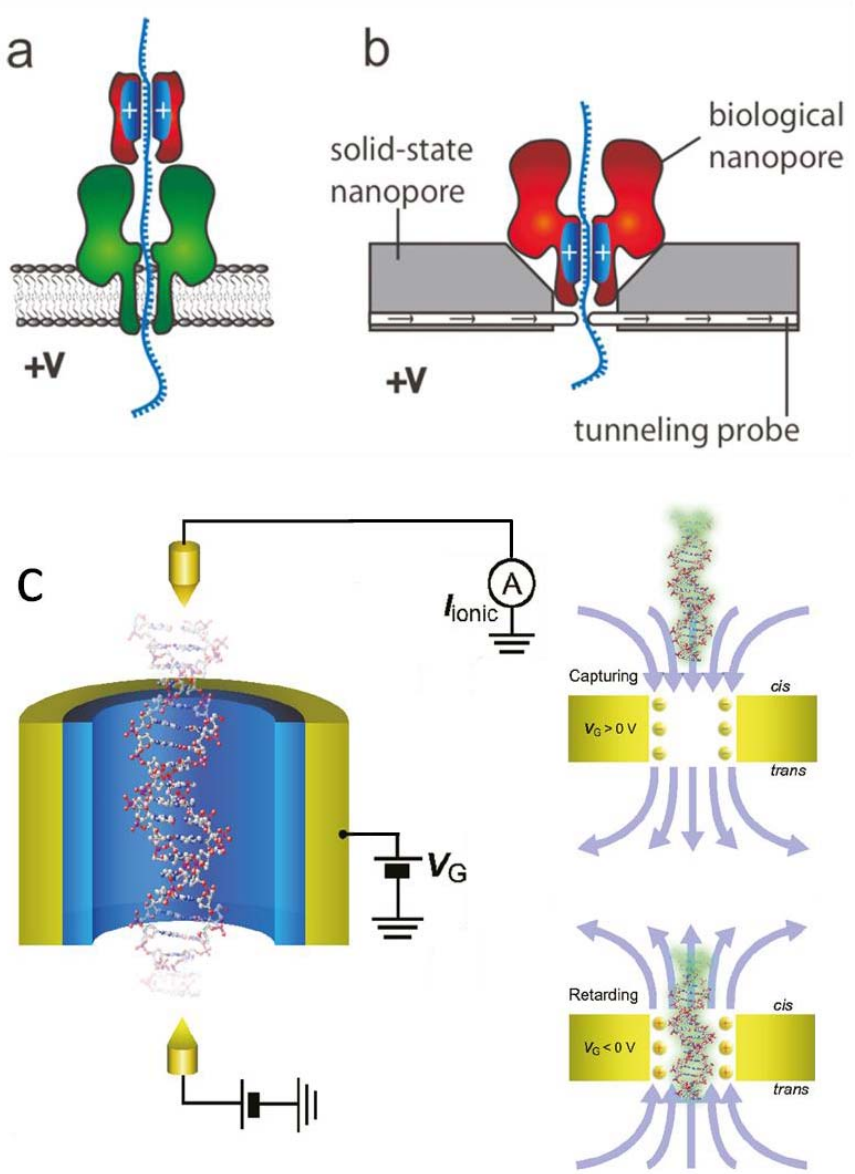

Figure 7.1 A proposed design of a translocation brake or gate in DNA nanopore sensors.[134, 136] (a) A molecular brake in the form of additional positive charge (red) placed outside an α-hemolysin nanopore (b) A reconstructed α-hemolysin nanopore with positive internal charge placed inside a solid state nanopore with a tunneling readout junction. (c) Solid-state nanopore with gate electrode to adjust the charge in the electrical double layers (EDL). There are two stages for this nanopore: *Capturing stage* in which a positive gate voltage V_G is applied to capture DNA and the induced electroosmotic flow (EOF) is to the same direction as DNA translocation; *Retarding stage* in which a negative gate bias minimizes DNA speed and the induced EOF is reversed to slow down the DNA translocation.

7.2.2 CNT Based Molecular Transistor

In our work, it was pointed out that translocation of DNA molecules through electrically-isolated single-walled carbon nanotubes was signaled by giant charge pulses, each containing about 10^7 units of electronic charge. Since this is more charge, by many orders of magnitude, than can be packed into the space available in the carbon nanotube channel, it was hypothesized that translocation of the channel by a charged molecule was accompanied by a large change in polarization of the channel. Accordingly, the charge on the channel must change by a large amount when a charged molecule translocates. The carbon nanotube acts as a "charge amplifier". It follows, therefore, that the potential of the carbon nanotube must change during translocation. Thus, by a reciprocal action, one might expect that control of the potential of the carbon nanotube would enable control of the rate of translocation of the tube by charged molecules. That action is demonstrated below.

Like the CNT ionic FET device described in Chapter 5, a single-walled carbon nanotube spans a barrier separating two fluid reservoirs from each other around 20μm. The barrier is still formed from a layer of dielectric material, silicon dioxide (~20nm) and a resist like polymethylmethacrylate (PMMA) (~800nm). Finally, the reservoirs etched into the barrier material are connected to an external fluidic system by means of a PDMS

microfluidic delivery device. The reservoirs are filled with an electrolyte like KCl, with concentration between 1 mM and 1M. The Ag/AgCl electrodes, in contact with a continuous electrolyte connected to the reservoirs, to measure the ionic current through CNT.

The introduction of a gate electrode has been used to control the ionic current, shown in Chapter 5. It is connected to external circuitry by means of a microfabricated lead that passes out of the device under a layer of dielectric material (SiO_2) that protects it from contact with electrolyte. A bias, Vg, may be applied to the gate via a voltage source, and a current to voltage converter, at the same time, monitors the gate current, Ig, shown in **Figure 7.2 (a)**.

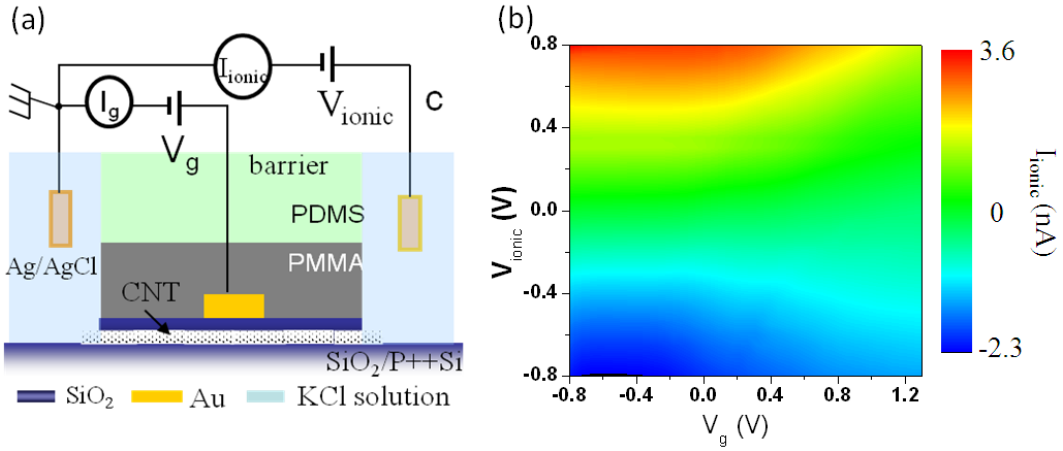

Figure 7.2 (a) A cross section of the molecular transistor device along the axis of the carbon nanotube. (b) Gating of ion current through the device (p-type ionic FET). Three dimensional "heat map" showing measured ion current through the transistor as a function of bias applied between the reservoirs, V_{ionic}, and the gate bias, V_g.

The device as described can control the flow of ionic current through the carbon nanotube, much as described in the prior art for the conical nanopore of Kalman et al.[137] **Figure 7.2 (b)** shows a typical set of p-type ionic CNT-FET characteristics. This is a three dimensional plot of V_{ionic} vs. V_g and I_i (shown by the color scale) for 1mM KCl electrolyte. Since this kind of device can control the flow of ionic current through the tube, can it also manipulate the translocation of any charged molecules dissolved in the electrolyte?

Here **Figure 7.3** shows what is observed when a 1mM solution of deoxycytidine monophosphate (dCMP) is introduced into the reservoir that is biased negative (so that this negative molecule is driven through the nanotube towards the positive reservoir). The background current climbs after introduction of the molecules, very large current pulses marking translocation events after a period of time, exactly as described for DNA molecules in Chapter 4. For the data shown here, the gate electrode is not connected, so the device performs exactly as reported for devices without a gate.[64, 65]

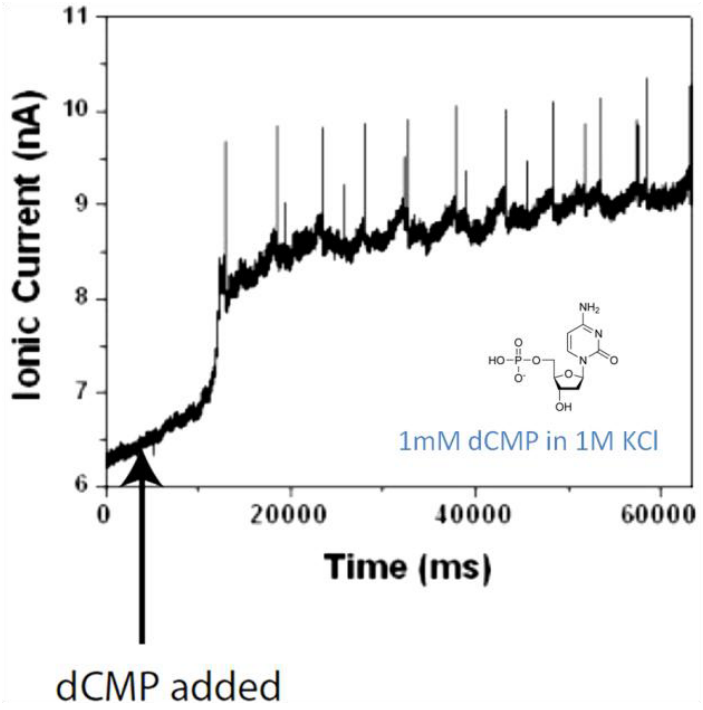

Figure 7.3 Change in ion current vs. time as a charged molecule dCMP (1mM), is added to the negatively biased reservoir. The spikes in current signal single molecule translocations. Inset shows the chemical structure of dCMP.

The effects of connecting the gate are illustrated in **Figure 7.4**. Here, a bias of V_{ionic} = 0.6V is applied, resulting about 3 translocation events per second. The spikes are closely spaced, and positive in direction, as shown in **Figure 7.4a**. Here, the gate is initially held at Vg=0V. When the gate is switched to Vg= -0.5V for 100s, it is switched back to Vg=0V. There is no measurable change in the translocation rate. The effect of making the gate positive is shown in **Figure 7.4b**. The conditions are the same as in the top trace, but the gate is switched from Vg=0V to Vg=+0.5V for 100s. The translocation rate is reduced from about 3 per second to less than 1 per

second. **Figure 7.4c** shows the effect of switching the gate bias to +1V. Again, the gate is set initially to Vg=0V and the translocation rate is about 3/s. When the Vg is set to +1V (for 100s), interestingly the pulse rate slows and stops, only being restored when Vg is set back to 0V. In this case, we believe this result means that the translocation process is not only stopped, but also the translocation speed of charged molecules is reduced. However, PCR cannot be used to directly test the tranlocated molecules and so we could not quantitatively calculate number of molecules per spike. Besides, we also found that the charging and discharging of the carbon nanotube is evident in spikes in the gate current (I_g) that accompanies the transit of molecules (**Figure 7.4d**). Actually, there is good alignment of spike singals between the ionic current and gate current. Thus it is possible not to monitor ionic current to detect a single molecule translocation event as these are also evident in the gate current signals.

The action of a molecular transistor is primarily demonstrated, definitely we still need to do more work to find out how the molecular translocation is switched between “on” and “off” states, to confirm the its reliability on slowing down the charged molecules (like DNA) translocation speed. Anyway, it still shows a promising method for building up the DNA sequencing nanopore devices.

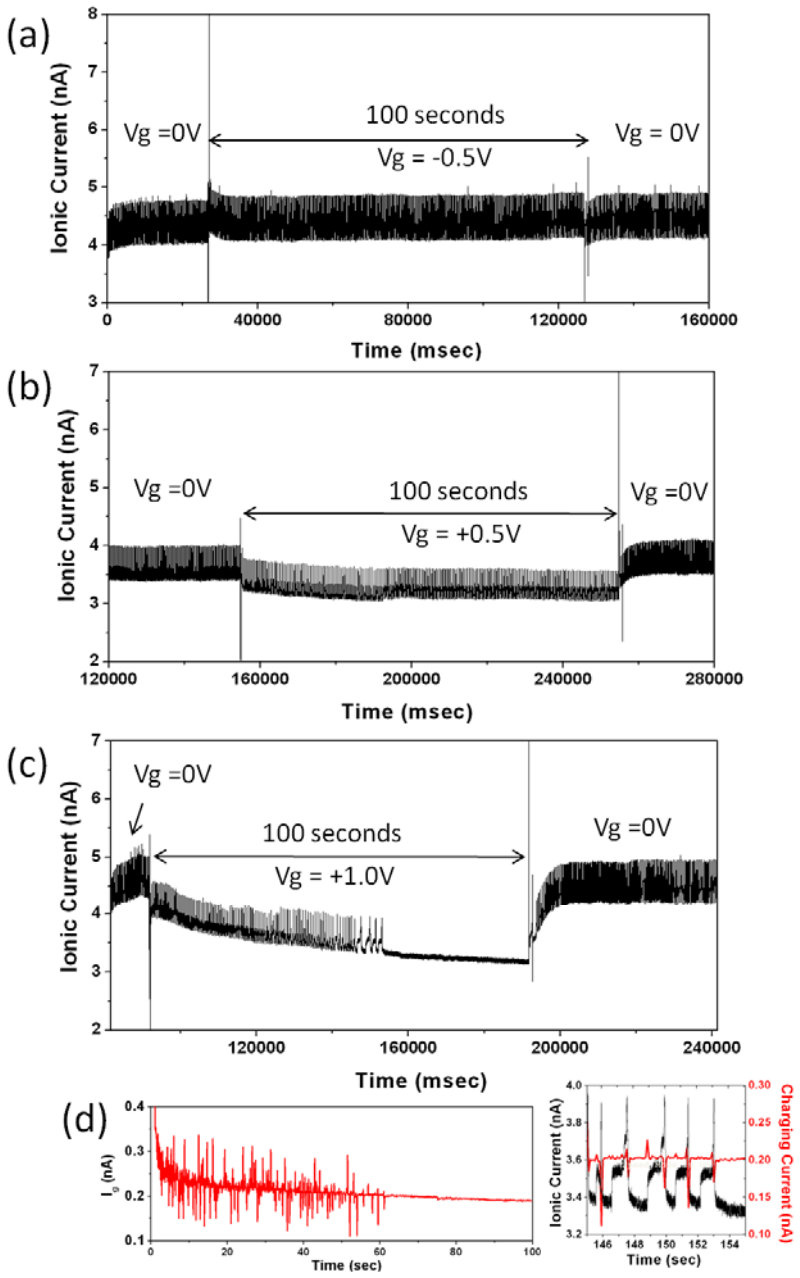

Figure 7.4 Molecular transistor action with V_{ionic} = 0.6V. A negative gate (-0.5V) bias does not affect the translocation (a) The translocation rate is reduced (b) at positive gate bias (+0.5V), finally turning off completely with Vg =1.0V (c). The operation of the device is completely reversible. (d) Left: showing the gate current over the time interval where molecular flow is turned off, showing how ionic current spikes are mirrored by spikes in the gate current; Right: good alignment of spike singals between the ionic current and gate current, that can be used to monitor the translocation process.

REFERENCES

1. Iijima, S., Helical Microtubules of Graphitic Carbon. *Nature* 1991, 354, 56-58.

2. Dresselhaus, M. S., Dresselhaus, G., Avouris, Ph. , *Carbon Nanotubes- Synthesis, Structure, Properties, and Applications; Topics in Applied Physics* Springer: 2001; Vol. 80.

3. Saito, R.; Dresselhaus, G.; Dresselhaus, M. S., *Physical properties of carbon nanotubes*. London: Imperal College Press: 1998.

4. Reich, S.; Maultzsch, J.; Thomsen, C.; Ordejón, P., Tight-binding description of graphene. *Physical Review B* 2002, 66, 035412.

5. Electronic Band Structure of a Single-Walled Carbon Nanotube by the Zone-Folding Method, Wolfram CDF Player. http://demonstrations.wolfram.com/ElectronicBandStructureOfASingleWalledCarbonNanotubeByTheZon/.

6. Bhaviripudi, S.; Reina, A.; Qi, J.; Kong, J.; Belcher, A. M., Block-copolymer assisted synthesis of arrays of metal nanoparticles and their catalytic activities for the growth of SWNTs. *Nanotechnology* 2006, 17, 5080-5086.

7. Li, Y.; Kim, W.; Zhang, Y.; Rolandi, M.; Wang, D.; Dai, H., Growth of Single-Walled Carbon Nanotubes from Discrete Catalytic Nanoparticles of Various Sizes. *The Journal of Physical Chemistry B* 2001, 105, 11424-11431.

8. Huang, L.; Cui, X.; White, B.; O'Brien, S. P., Long and Oriented Single-Walled Carbon Nanotubes Grown by Ethanol Chemical Vapor Deposition. *The Journal of Physical Chemistry B* 2004, 108, 16451-16456.

9. Javey, A.; Shim, M.; Dai, H., Electrical properties and devices of large-diameter single-walled carbon nanotubes. *Applied Physics Letters* 2002, 80, 1064-1066.

10. Bubendorfer, A.; Liu, X.; Ellis, A. V., Microfabrication of PDMS microchannels using SU-8/PMMA moldings and their sealing to polystyrene substrates. *Smart Materials and Structures* 2007, 16, 367-371.

11. Christensen, A. M.; Chang-Yen, D. A.; Gale, B. K., Characterization of interconnects used in PDMS microfluidic systems. *Journal of Micromechanics and Microengineering* 2005, 15, 928-934.

12. Kim, W.; Javey, A.; Vermesh, O.; Wang, Q.; Li, Y.; Dai, H., Hysteresis Caused by Water Molecules in Carbon Nanotube Field-Effect Transistors. *Nano Letters* 2003, 3, 193-198.

13. http://www.ims.ut.ee/~alar/microtech/Ch1_2/.

14. Schoch, R. B.; Han, J.; Renaud, P., Transport phenomena in nanofluidics. *Reviews of Modern Physics* 2008, 80, 839.

15. Daiguji, H., Ion transport in nanofluidic channels. *Chemical Society Reviews* 2010, 39, 901-911.

16. Karnik, R.; Fan, R.; Yue, M.; Li, D.; Yang, P.; Majumdar, A., Electrostatic Control of Ions and Molecules in Nanofluidic Transistors. *Nano Letters* 2005, 5, 943-948.

17. Schasfoort, R. B.; nbsp; M; Schlautmann, S.; Hendrikse, J.; van den Berg, A., Field-Effect Flow Control for Microfabricated Fluidic Networks. *Science* 1999, 286, 942-945.

18. Spencer, A. J. M., *Continuum mechanics*. Dover Publications, Inc.: 2004.

19. Wang, X.-L.; Tsuru, T.; Nakao, S.-i.; Kimura, S., Electrolyte transport through nanofiltration membranes by the space-charge model and the comparison with Teorell-Meyer-Sievers model. *Journal of Membrane Science* 1995, 103, 117-133.

20. Jin, X.; Aluru, N., Gated transport in nanofluidic devices. *Microfluidics and Nanofluidics* 2011, 11, 297-306.

21. Sparreboom, W.; van den Berg, A.; Eijkel, J. C. T., Principles and applications of nanofluidic transport. *Nat Nano* 2009, 4, 713-720.

22. Daiguji, H.; Yang, P.; Majumdar, A., Ion Transport in Nanofluidic Channels. *Nano Letters* 2003, 4, 137-142.

23. Aluru, N. R.; Li, G., Finite cloud method: a true meshless technique based on a fixed reproducing kernel approximation. *International Journal for Numerical Methods in Engineering* 2001, 50, 2373-2410.

24. Howorka, S.; Siwy, Z., Nanopore analytics: sensing of single molecules. *Chemical Society Reviews* 2009, 38, 2360-2384.

25. Branton, D.; Deamer, D. W.; Marziali, A.; Bayley, H.; Benner, S. A.; Butler, T.; Di Ventra, M.; Garaj, S.; Hibbs, A.; Huang, X. H.; Jovanovich, S. B.; Krstic, P. S.; Lindsay, S.; Ling, X. S. S.; Mastrangelo, C. H.; Meller, A.; Oliver, J. S.; Pershin, Y. V.; Ramsey, J. M.; Riehn, R.; Soni, G. V.; Tabard-Cossa, V.; Wanunu, M.; Wiggin, M.; Schloss, J. A., The potential and challenges of nanopore sequencing. *Nature Biotechnology* 2008, 26, 1146-1153.

26. Kasianowicz, J. J.; Brandin, E.; Branton, D.; Deamer, D. W., Characterization of individual polynucleotide molecules using a membrane channel. *Proceedings of the National Academy of Sciences* 1996, 93, 13770-13773.

27. Kasianowicz, J. J.; Henrickson, S. E.; Weetall, H. H.; Robertson, B., Simultaneous multianalyte detection with a nanometer-scale pore. *Analytical Chemistry* 2001, 73, 2268-2272.

28. Han, A.; Creus, M.; Schürmann, G.; Linder, V.; Ward, T. R.; de Rooij, N. F.; Staufer, U., Label-Free Detection of Single Protein Molecules and Protein−Protein Interactions Using Synthetic Nanopores. *Analytical Chemistry* 2008, 80, 4651-4658.

29. Deamer, D., Nanopore Analysis of Nucleic Acids Bound to Exonucleases and Polymerases. *Annual Review of Biophysics* 2010, 39, 79-90.

30. Venkatesan, B. M.; Bashir, R., Nanopore sensors for nucleic acid analysis. *Nat Nano* 2011, 6, 615-624.

31. Clarke, J.; Wu, H.-C.; Jayasinghe, L.; Patel, A.; Reid, S.; Bayley, H., Continuous base identification for single-molecule nanopore DNA sequencing. *Nat Nano* 2009, 4, 265-270.

32. Li, J.; Stein, D.; McCullan, D.; Branton, D.; Aziz, M. J.; Golovchenko, J. A., Ion-beam sculpting at Nanometer length scales. *Nature* 2001, 412, 166-169.

33. Storm, A.; Chen, J.; Ling, X.; Zandbergen, H.; Dekker, C., Fabrication of solid-state nanopores with single-nanometre precision. *Nature Mat., 2003* 2003, 2, 537-40.

34. Chang, H.; Iqbal, S.; Stach, E.; King, A.; Zaluzec, N.; Bashir, R., Fabrication and characterization of solid state nanopores using field emission scanning electron beam. *App. Phys. Lett.* 2006, 88, 103109.

35. Kim, M. J.; Wanunu, M.; Bell, D. C.; Meller, A., Rapid Fabrication of Uniformly Sized Nanopores and Nanopore Arrays for Parallel DNA Analysis. *Advanced Materials* 2006, 18, 3149-3153.

36. Chen, P.; Mitsui, T.; Farmer, D. B.; Golovchenko, J.; Gordon, R. G.; Branton, D., Atomic layer deposition to fine-tune the surface properties and diameters of fabricated nanopores. *Nano Lett.* 2004, 4, 1333.

37. Venkatesan, B. M.; Dorvel, B.; Yemenicioglu, S.; Watkins, N.; Petrov, I.; Bashir, R., Highly Sensitive, Mechanically Stable Nanopore Sensors for DNA Analysis. *Advanced Materials* 2009, 21, 2771-2776.

38. Garaj, S.; Hubbard, W.; Reina, A.; Kong, J.; Branton, D.; Golovchenko, J. A., Graphene as a subnanometre trans-electrode membrane. *Nature* 2010, 467, 190-193.

39. Huang, S.; He, J.; Chang, S.; Zhang, P.; Liang, F.; Li, S.; Tuchband, M.; Fuhrmann, A.; Ros, R.; Lindsay, S., Identifying single bases in a DNA oligomer with electron tunnelling. *Nat Nano* 2010, 5, 868-873.

40. Mattia, D.; Gogotsi, Y., Review: static and dynamic behavior of liquids inside carbon nanotubes. *Microfluidics and Nanofluidics* 2008, 5, 289-305.

41. Noy, A.; Park, H. G.; Fornasiero, F.; Holt, J. K.; Grigoropoulos, C. P.; Bakajin, O., Nanofluidics in carbon nanotubes. *Nano Today* 2007, 2, 22-29.

42. Whitby, M.; Quirke, N., Fluid flow in carbon nanotubes and nanopipes. *Nat Nano* 2007, 2, 87-94.

43. Hummer, G.; Rasaiah, J. C.; Noworyta, J. P., Water conduction through the hydrophobic channel of a carbon nanotube. *Nature* 2001, 414, 188-190.

44. Wei, C.; Srivastava, D., Theory of Transport of Long Polymer Molecules through Carbon Nanotube Channels. *Physical Review Letters* 2003, 91, 235901.

45. Xie, Y.; Kong, Y.; Soh, A. K.; Gao, H., Electric field-induced translocation of single-stranded DNA through a polarized carbon nanotube membrane. *The Journal of Chemical Physics* 2007, 127, 225101.

46. Yeh, I.-C.; Hummer, G., Nucleic acid transport through carbon nanotube membranes. *Proceedings of the National Academy of Sciences of the United States of America* 2004, 101, 12177-12182.

47. Gao, H.; Kong, Y.; Cui, D.; Ozkan, C. S., Spontaneous Insertion of DNA Oligonucleotides into Carbon Nanotubes. *Nano Letters* 2003, 3, 471-473.

48. Chen, M.; Khalid, S.; Sansom, M. S. P.; Bayley, H., Outer membrane protein G: Engineering a quiet pore for biosensing. *Proceedings of the National Academy of Sciences of the United States of America* 2008, 105, 6272-6277.

49. Maniwa, Y.; Matsuda, K.; Kyakuno, H.; Ogasawara, S.; Hibi, T.; Kadowaki, H.; Suzuki, S.; Achiba, Y.; Kataura, H., Water-filled single-wall carbon nanotubes as molecular nanovalves. *Nat Mater* 2007, 6, 135-141.

50. Byl, O.; Liu, J.-C.; Wang, Y.; Yim, W.-L.; Johnson, J. K.; Yates, J. T., Unusual Hydrogen Bonding in Water-Filled Carbon Nanotubes. *Journal of the American Chemical Society* 2006, 128, 12090-12097.

51. Naguib, N.; Ye, H.; Gogotsi, Y.; Yazicioglu, A. G.; Megaridis, C. M.; Yoshimura, M., Observation of Water Confined in Nanometer Channels of Closed Carbon Nanotubes. *Nano Letters* 2004, 4, 2237-2243.

52. Rossi, M. P.; Ye, H.; Gogotsi, Y.; Babu, S.; Ndungu, P.; Bradley, J.-C., Environmental Scanning Electron Microscopy Study of Water in Carbon Nanopipes. *Nano Letters* 2004, 4, 989-993.

53. Hinds, B. J.; Chopra, N.; Rantell, T.; Andrews, R.; Gavalas, V.; Bachas, L. G., Aligned Multiwalled Carbon Nanotube Membranes. *Science* 2004, 303, 62-65.

54. Holt, J. K.; Park, H. G.; Wang, Y. M.; Stadermann, M.; Artyukhin, A. B.; Grigoropoulos, C. P.; Noy, A.; Bakajin, O., Fast mass transport

through sub-2-nanometer carbon nanotubes. *Science* 2006, 312, 1034-1037.

55. Majumder, M.; Chopra, N.; Hinds, B. J., Effect of Tip Functionalization on Transport through Vertically Oriented Carbon Nanotube Membranes. *Journal of the American Chemical Society* 2005, 127, 9062-9070.

56. Fornasiero, F.; Park, H. G.; Holt, J. K.; Stadermann, M.; Grigoropoulos, C. P.; Noy, A.; Bakajin, O., Ion exclusion by sub-2-nm carbon nanotube pores. *Proceedings of the National Academy of Sciences* 2008, 105, 17250-17255.

57. Corry, B., Designing Carbon Nanotube Membranes for Efficient Water Desalination. *The Journal of Physical Chemistry B* 2007, 112, 1427-1434.

58. Sun, L.; Crooks, R. M., Single Carbon Nanotube Membranes: A Well-Defined Model for Studying Mass Transport through Nanoporous Materials. *Journal of the American Chemical Society* 2000, 122, 12340-12345.

59. Shashank, S.; Maria Pia, R.; Mattia, D.; Yury, G.; Haim, H. B., Induction and measurement of minute flow rates through nanopipes. *Physics of Fluids* 2007, 19, 013603.

60. Ito, T.; Sun, L.; Crooks, R. M., Observation of DNA transport through a single carbon nanotube channel using fluorescence microscopy. *Chemical Communications* 2003, 1482-1483.

61. Fan, R.; Karnik, R.; Yue, M.; Li, D.; Majumdar, A.; Yang, P., DNA Translocation in Inorganic Nanotubes. *Nano Lett.* 2005, 5, 1633-1637.

62. Yeh, I.-C.; Hummer, G., Nucleic acid transport through carbon nanotube membranes *Proc. Natl. Acad. Sci. (USA)* 2004, 101, 12177-12182.

63. Xie, Y.; Kong, Y.; Soh, A. K.; Gao, H., Electric field translocation of single-stranded DNA through a polarized carbon nanotube membrane. *J. Chem. Phys.* 2007, 127, 225101-7.

64. He, J.; Liu, H.; Pang, P.; Cao, D.; Lindsay, S., Translocation events in a single-walled carbon nanotube. *Journal of Physics-Condensed Matter* 2010, 22.

65. Liu, H.; He, J.; Tang, J.; Liu, H.; Pang, P.; Cao, D.; Krstic, P.; Joseph, S.; Lindsay, S.; Nuckolls, C., Translocation of Single-Stranded DNA Through Single-Walled Carbon Nanotubes. *Science* 2010, 327, 64-67.

66. Guo, X.; Small, J. P.; Klare, J. E.; Wang, Y.; Purewal, M. S.; Tam, I. W.; Hong, B. H.; Caldwell, R.; Huang, L.; O'Brien, S.; Yan, J.; Breslow, R.; Wind, S. J.; Hone, J.; Kim, P.; Nuckolls, C., Covalently bridging gaps in single-walled carbon nanotubes with conducting molecules. *Science* 2006, 311, 356-9.

67. Chow, K.-F.; Mavré, F. o.; Crooks, R. M., Wireless Electrochemical DNA Microarray Sensor. *Journal of the American Chemical Society* 2008, 130, 7544-7545.

68. Warakulwit, C.; Nguyen, T.; Majimel, J.; Delville, M.-H.; Lapeyre, V.; Garrigue, P.; Ravaine, V.; Limtrakul, J.; Kuhn, A., Dissymmetric Carbon Nanotubes by Bipolar Electrochemistry. *Nano Letters* 2008, 8, 500-504.

69. Joseph, S.; Mashl, R. J.; Jakobsson, E.; Aluru, N. R., Electrolytic Transport in Modified Carbon Nanotubes. *Nano Letters* 2003, 3, 1399-1403.

70. Smeets, R. M. M.; Keyser, U. F.; Krapf, D.; Wu, M.-Y.; Dekker, N. H.; Dekker, C., Salt Dependence of Ion Transport and DNA Translocation through Solid-State Nanopores. *Nano Letters* 2006, 6, 89-95.

71. Fan, R.; Karnik, R.; Yue, M.; Li, D.; Majumdar, A.; Yang, P., DNA Translocation in Inorganic Nanotubes. *Nano Letters* 2005, 5, 1633-1637.

72. Jin, X.; Joseph, S.; Gatimu, E. N.; Bohn, P. W.; Aluru, N. R., Induced Electrokinetic Transport in Micro-Nanofluidic Interconnect Devices. *Langmuir* 2007, 23, 13209-13222.

73. Tu, X.; Manohar, S.; Jagota, A.; Zheng, M., DNA sequence motifs for structure-specific recognition and separation of carbon nanotubes. *Nature* 2009, 460, 250-253.

74. Dekker, C., Solid-state nanopores. *Nature Nanotechnology* 2007, 2, 209-215.

75. Kim, S. J.; Wang, Y.-C.; Lee, J. H.; Jang, H.; Han, J., Concentration Polarization and Nonlinear Electrokinetic Flow near a Nanofluidic Channel. *Physical Review Letters* 2007, 99, 044501.

76. Daiguji, H., Nanofluidics: High mobility in tight spaces. *Nat Nano* 2010, 5, 831-832.

77. Liang, X.; Chou, S. Y., Nanogap Detector Inside Nanofluidic Channel for Fast Real-Time Label-Free DNA Analysis. *Nano Letters* 2008, 8, 1472-1476.

78. Duan, C.; Majumdar, A., Anomalous ion transport in 2-nm hydrophilic nanochannels. *Nat Nano* 2010, 5, 848-852.

79. Cruz-Chu, E. R.; Ritz, T.; Siwy, Z. S.; Schulten, K., Molecular control of ionic conduction in polymer nanopores. *Faraday Discussions* 2009, 143, 47-62.

80. Qiao, R.; Aluru, N. R., Atypical Dependence of Electroosmotic Transport on Surface Charge in a Single-wall Carbon Nanotube. *Nano Letters* 2003, 3, 1013-1017.

81. Chen, Y.; Ni, Z.; Wang, G.; Xu, D.; Li, Electroosmotic Flow in Nanotubes with High Surface Charge Densities. *Nano Letters* 2007, 8, 42-48.

82. Park, J. H.; Sinnott, S. B.; Aluru, N. R., Ion separation using a Y-junction carbon nanotube. *Nanotechnology* 2006, 17, 895.

83. Majumder, M.; Chopra, N.; Andrews, R.; Hinds, B. J., Nanoscale hydrodynamics: Enhanced flow in carbon nanotubes. *Nature* 2005, 438, 44-44.

84. Lee, C. Y.; Choi, W.; Han, J.-H.; Strano, M. S., Coherence Resonance in a Single-Walled Carbon Nanotube Ion Channel. *Science* 2010, 329, 1320-1324.

85. Nam, S.-W.; Rooks, M. J.; Kim, K.-B.; Rossnagel, S. M., Ionic Field Effect Transistors with Sub-10 nm Multiple Nanopores. *Nano Letters* 2009, 9, 2044-2048.

86. Jiang, Z.; Stein, D., Electrofluidic Gating of a Chemically Reactive Surface. *Langmuir* 2010, 26, 8161-8173.

87. Luan, B.; Peng, H.; Polonsky, S.; Rossnagel, S.; Stolovitzky, G.; Martyna, G., Base-By-Base Ratcheting of Single Stranded DNA through a Solid-State Nanopore. *Physical Review Letters* 2010, 104, 238103.

88. Leonard, F., *Physics of Carbon Nanotube Devices, The Micro and Nano Technologies*. Elsevier Science & Technology: 2008.

89. Pang, P.; He, J.; Park, J. H.; Krstić, P. S.; Lindsay, S., Origin of Giant Ionic Currents in Carbon Nanotube Channels. *ACS Nano* 2011, 5, 7277-7283.

90. Smeets, R. M. M.; Keyser, U. F.; Krapf, D.; Wu, M.-Y.; Dekker, N. H.; Dekker, C., Salt Dependence of Ion Transport and DNA Translocation through Solid-State Nanopores. *Nano Letters* 2005, 6, 89-95.

91. Lu, W.; Wang, D.; Chen, L., Near-Static Dielectric Polarization of Individual Carbon Nanotubes. *Nano Letters* 2007, 7, 2729-2733.

92. Majumder, M.; Chopra, N.; Hinds, B. J., Mass Transport through Carbon Nanotube Membranes in Three Different Regimes: Ionic Diffusion and Gas and Liquid Flow. *ACS Nano* 2011, 5, 3867-3877.

93. Joseph, S.; Aluru, N. R., Why Are Carbon Nanotubes Fast Transporters of Water? *Nano Letters* 2008, 8, 452-458.

94. Wu, J.; Gerstandt, K.; Majumder, M.; Zhan, X.; Hinds, B. J., Highly Efficient Electroosmotic Flow through Functionalized Carbon Nanotube Membranes. *Nanoscale* 2011, 3, 3321-3328.

95. Kong, J.; Franklin, N. R.; Zhou, C.; Chapline, M. G.; Peng, S.; Cho, K.; Dai, H., Nanotube Molecular Wires as Chemical Sensors. *Science* 2000, 287, 622-625.

96. Douglas, R. K.; Alexander, S., Carbon Nanotube Gas and Vapor Sensors. *Angew. Chem. Int. Edit.* 2008, 47, 6550-6570.

97. Wenrong, Y.; Kyle, R.; Simon, R.; Pall, T.; Justin, G.; Filip, B., Carbon Nanomaterials in Biosensors: Should You Use Nanotubes or Graphene? *Angew. Chem. Int. Edit.* 2010, 49, 2114-2138.

98. Dujardin, E.; Ebbesen, T. W.; Hiura, H.; Tanigaki, K., Capillarity and Wetting of Carbon Nanotubes. *Science* 1994, 265, 1850-1852.

99. Erik, D.; Thomas, W. E.; Ajit, K.; Michael, M. J. T., Wetting of Single Shell Carbon Nanotubes. *Adv. Mater.* 1998, 10, 1472-1475.

100. Joseph, S.; Aluru, N. R., Why Are Carbon Nanotubes Fast Transporters of Water? *Nano Lett.* 2008, 8, 452-458.

101. Naguib, N.; Ye, H.; Gogotsi, Y.; Yazicioglu, A. G.; Megaridis, C. M.; Yoshimura, M., Observation of Water Confined in Nanometer Channels of Closed Carbon Nanotubes. *Nano Lett.* 2004, 4, 2237-2243.

102. Cambr; eacute; Sofie; Schoeters, B.; Luyckx, S.; Goovaerts, E.; Wenseleers, W., Experimental Observation of Single-File Water Filling of Thin Single-Wall Carbon Nanotubes Down to Chiral Index (5,3). *Phys. Rev. Lett.* 2010, 104, 207401.

103. Chen, Q.; Herberg, J. L.; Mogilevsky, G.; Wang, H.-J.; Stadermann, M.; Holt, J. K.; Wu, Y., Identification of Endohedral Water in Single-Walled Carbon Nanotubes by 1H NMR. *Nano Lett.* 2008, 8, 1902-1905.

104. Maniwa, Y.; Matsuda, K.; Kyakuno, H.; Ogasawara, S.; Hibi, T.; Kadowaki, H.; Suzuki, S.; Achiba, Y.; Kataura, H., Water-Filled Single-Wall Carbon Nanotubes as Molecular Nanovalves. *Nat. Mater.* 2007, 6, 135-141.

105. Byl, O.; Liu, J.-C.; Wang, Y.; Yim, W.-L.; Johnson, J. K.; Yates, J. T., Unusual Hydrogen Bonding in Water-Filled Carbon Nanotubes. *J. Am. Chem. Soc.* 2006, 128, 12090-12097.

106. Kolesnikov, A. I.; Zanotti, J.-M.; Loong, C.-K.; Thiyagarajan, P.; Moravsky, A. P.; Loutfy, R. O.; Burnham, C. J., Anomalously Soft Dynamics of Water in a Nanotube: A Revelation of Nanoscale Confinement. *Phys. Rev. Lett.* 2004, 93, 035503.

107. Cambré, S.; Schoeters, B.; Luyckx, S.; Goovaerts, E.; Wenseleers, W., Experimental Observation of Single-File Water Filling of Thin Single-Wall Carbon Nanotubes Down to Chiral Index (5,3). *Physical Review Letters* 2010, 104, 207401.

108. Whitby, M.; Quirke, N., Fluid Flow in Carbon Nanotubes and Nanopipes. *Nat. Nano.* 2007, 2, 87-94.

109. Liang, X.; Chou, S. Y., Nanogap Detector Inside Nanofluidic Channel for Fast Real-Time Label-Free DNA Analysis. *Nano Lett.* 2008, 8, 1472-1476.

110. Dekker, C., Solid-State Nanopores. *Nat. Nano.* 2007, 2, 209-215.

111. Fan, R.; Karnik, R.; Yue, M.; Li, D.; Majumdar, A.; Yang, P., DNA Translocation in Inorganic Nanotubes. *Nano Lett.* 2005, 5, 1633-1637.

112. Lee, R. S.; Kim, H. J.; Fischer, J. E.; Thess, A.; Smalley, R. E., Conductivity enhancement in single-walled carbon nanotube bundles doped with K and Br. *Nature* 1997, 388, 255-257.

113. Staii, C.; Johnson, A. T.; Chen, M.; Gelperin, A., DNA-Decorated Carbon Nanotubes for Chemical Sensing. *Nano Lett.* 2005, 5, 1774-1778.

114. Star, A.; Gabriel, J.-C. P.; Bradley, K.; Gruner, G., Electronic Detection of Specific Protein Binding Using Nanotube FET Devices. *Nano Lett.* 2003, 3, 459-463.

115. Heinze, S.; Tersoff, J.; Martel, R.; Derycke, V.; Appenzeller, J.; Avouris, P., Carbon Nanotubes as Schottky Barrier Transistors. *Phys. Rev. Lett.* 2002, 89, 106801.

116. Avouris, P.; Chen, Z.; Perebeinos, V., Carbon-Based Electronics. *Nat. Nano.* 2007, 2, 605-615.

117. Pati, R.; Zhang, Y.; Nayak, S. K.; Ajayan, P. M., Effect of H_2O Adsorption on Electron Transport in a Carbon Nanotube. *Appl. Phys. Lett.* 2002, 81, 2638-2640.

118. Na, P. S.; Kim, H.; So, H.-M.; Kong, K.-J.; Chang, H.; Ryu, B. H.; Choi, Y.; Lee, J., O.; Kim, B.-K.; Kim, J.-J.; Kim, J., Investigation of the humidity effect on the electrical properties of single-walled carbon nanotube transistors. *Appl. Phys. Lett.* 2005, 87, 093101.

119. Sung, D.; Hong, S.; Kim, Y.-H.; Park, N.; Kim, S.; Maeng, S. L.; Kim, K.-C., Ab Initio Study of the Effect of Water Adsorption on the Carbon Nanotube Field-Effect Transistor. *Appl. Phys. Lett.* 2006, 89, 243110.

120. Kim, W.; Javey, A.; Vermesh, O.; Wang, Q.; Li, Y.; Dai, H., Hysteresis Caused by Water Molecules in Carbon Nanotube Field-Effect Transistors. *Nano Lett.* 2003, 3, 193-198.

121. Zahab, A.; Spina, L.; Poncharal, P.; Marliere, C., Water-Vapor Effect on the Electrical Conductivity of a Single-Walled Carbon Nanotube Mat. *Phys. Rev. B* 2000, 62, 10000.

122. Heller, I.; Mannik, J.; Lemay, S. G.; Dekker, C., Optimizing the Signal-to-Noise Ratio for Biosensing with Carbon Nanotube Transistors. *Nano Lett.* 2009, 9, 377-382.

123. Cui, X.; Freitag, M.; Martel, R.; Brus, L.; Avouris, P., Controlling Energy-Level Alignments at Carbon Nanotube/Au Contacts. *Nano Lett.* 2003, 3, 783-787.

124. Cao, D.; Pang, P.; He, J.; Luo, T.; Park, J. H.; Krstic, P.; Nuckolls, C.; Tang, J.; Lindsay, S., Electronic Sensitivity of Carbon Nanotubes to Internal Water Wetting. *ACS Nano* 2011, 5, 3113-3119.

125. Douglas, R. K.; Alexander, S., Carbon Nanotube Gas and Vapor Sensors. *Angewandte Chemie International Edition* 2008, 47, 6550-6570.

126. Zuo, G.; Shen, R.; Ma, S.; Guo, W., Transport Properties of Single-File Water Molecules inside a Carbon Nanotube Biomimicking Water Channel. *ACS Nano* 2009, 4, 205-210.

127. Joseph, S.; Aluru, N. R., Pumping of Confined Water in Carbon Nanotubes by Rotation-Translation Coupling. *Phys. Rev. Lett.* 2008, 101, 064502.

128. Chang, Y. W.; Sony, J.; Aluru, N. R., Effect of Quantum Partial Charges on the Structure and Dynamics of Water in Single-Walled Carbon Nanotubes. *J. Chem. Phys.* 2006, 125, 114701.

129. Yang, M. H.; Teo, K. B. K.; Milne, W. I.; Hasko, D. G., Carbon Nanotube Schottky Diode and Directionally Dependent Field-Effect Transistor Using Asymmetrical Contacts. *Appl. Phys. Lett.* 2005, 87, 253116.

130. Marcus, F.; Marko, R.; Yangxin, Z.; Johnson, A. T.; Walter, F. S., Controlled Creation of a Carbon Nanotube Diode by a Scanned Gate. *Appl. Phys. Lett.* 2001, 79, 3326-3328.

131. Majumder, M.; Chopra, N.; Hinds, B. J., Effect of Tip Functionalization on Transport through Vertically Oriented Carbon Nanotube Membranes. *J. Am. Chem. Soc.* 2005, 127, 9062-9070.

132. Fornasiero, F.; Park, H. G.; Holt, J. K.; Stadermann, M.; Grigoropoulos, C. P.; Noy, A.; Bakajin, O., Ion Exclusion by Sub-2-nm Carbon Nanotube Pores. *P. Natl. Acad. Sci.* 2008, 105, 17250-17255.

133. Benner, S.; Chen, R. J. A.; Wilson, N. A.; Abu-Shumays, R.; Hurt, N.; Lieberman, K. R.; Deamer, D. W.; Dunbar, W. B.; Akeson, M., Sequence-specific detection of individual DNA polymerase complexes in real time using a nanopore. *Nat Nano* 2007, 2, 718-724.

134. Rincon-Restrepo, M.; Mikhailova, E.; Bayley, H.; Maglia, G., Controlled Translocation of Individual DNA Molecules through Protein Nanopores with Engineered Molecular Brakes. *Nano Letters* 2011, 11, 746-750.

135. He, Y.; Tsutsui, M.; Fan, C.; Taniguchi, M.; Kawai, T., Gate Manipulation of DNA Capture into Nanopores. *ACS Nano* 2011.

136. He, Y.; Tsutsui, M.; Fan, C.; Taniguchi, M.; Kawai, T., Controlling DNA Translocation through Gate Modulation of Nanopore Wall Surface Charges. *ACS Nano* 2011, 5, 5509-5518.

137. Kalman, E.; Sudre, O.; Vlassiouk, I.; Siwy, Z., Control of ionic transport through gated single conical nanopores. *Analytical and Bioanalytical Chemistry* 2009, 394, 413-419.

APPENDIX

CO-AUTHOR APPROVAL

VERIFICATION OF CO-AUTHOR APPROVALS

I verify that the following co-authors have approved of my use of our publications in my dissertation.

Stuart Lindsay (Arizona State University)

Jin He (Arizona State University)

Di Cao (Arizona State University)

Hao Liu (Arizona State University)

Tao Luo (Arizona State University)

Colin Nuckolls (Columbia University)

Jinyao Tang (Columbia University)

Predrag Krstic (Oak Ridge National Laboratory)

Sony Joseph (Oak Ridge National Laboratory)

Jae Hyun Park (Oak Ridge National Laboratory)

Note: The author's address is listed as when the research was performed.